



저작자표시-비영리-변경금지 2.0 대한민국

이용자는 아래의 조건을 따르는 경우에 한하여 자유롭게

- 이 저작물을 복제, 배포, 전송, 전시, 공연 및 방송할 수 있습니다.

다음과 같은 조건을 따라야 합니다:



저작자표시. 귀하는 원저작자를 표시하여야 합니다.



비영리. 귀하는 이 저작물을 영리 목적으로 이용할 수 없습니다.



변경금지. 귀하는 이 저작물을 개작, 변형 또는 가공할 수 없습니다.

- 귀하는, 이 저작물의 재이용이나 배포의 경우, 이 저작물에 적용된 이용허락조건을 명확하게 나타내어야 합니다.
- 저작권자로부터 별도의 허가를 받으면 이러한 조건들은 적용되지 않습니다.

저작권법에 따른 이용자의 권리는 위의 내용에 의하여 영향을 받지 않습니다.

이것은 [이용허락규약\(Legal Code\)](#)을 이해하기 쉽게 요약한 것입니다.

[Disclaimer](#)

공학박사학위논문

**Dynamic Characteristics of the Turbulent Premixed
Bluff Body Flames in the Confined Combustor**

밀폐형 연소기에서 난류 예혼합 보염기 화염의 동적 특성

2017년 2월

서울대학교 대학원

기계항공공학부

정 찬 영

ABSTRACT

The dynamic characteristics and the combustion instability phenomenon of a premixed bluff body flame were investigated in a confined duct combustor. When the lean blowoff occurred due to the decrease of the equivalence ratio from the stable flame condition, the characteristics of the lean blowoff was compared and analyzed according to acoustic excitation to consider the external disturbance. Meanwhile, self-excited combustion instability that occur when the equivalence ratio increase from the stable flame condition and the flashback phenomenon coupled with self-excited combustion instability was investigated.

The blowoff equivalence ratio increases with the Reynolds number and changes depending on the extent of the recirculation zone. Using the relation between the Damköhler number and the Reynolds number, it was confirmed that the flow velocity at the downstream tip of the bluff body and the laminar flame speed are decisive blowoff factors. Although a periodic flame hole appeared far from the blowoff only with acoustic excitation, the blowoff observed by OH radical chemiluminescence occurred using a similar process regardless of the excitation. The recirculation zone collapses and the flame becomes small when it is close to the blowoff. Then, the flame is locally extinguished downstream from the bluff body and the recirculation zone completely collapses. Eventually, the unburned gas does not ignite and the flame is extinguished. The blowoff equivalence ratio rapidly increases at specific acoustic excitation frequencies. This was investigated using proper orthogonal decomposition analysis, the two-microphone method, and phase-locked particle imaging velocimetry measurement. Resonance occurs when the excitation frequency approaches the harmonic frequency of the combustor and it increases the velocity fluctuation in the combustor and the infiltration velocity of the unburned gas in the shear layer of the recirculation zone. Consequently, because the burning velocity must have a larger value corresponding to the enhanced mixture velocity for a sustained flame, the blowoff occurs at a higher equivalence ratio. In addition, the size of the recirculation zone was changed according to

the phase of the excitation frequency occurring the resonance and it was considered as the cause of attenuation for flame stability.

Previous studies investigating flashback in a bluff body have found that the flame moves back and forth around the trailing edge of the bluff body; however, the phenomenon in which the flame propagates beyond the bluff body has not been sufficiently studied. Therefore, it was necessary to understand a strong flashback, which can damage the upper section of a combustor and which is vulnerable to heat due to flame propagation over the front of the bluff body. The combustion instability frequency resulting from changes in the combustion length occurred within the range of the resonance frequency of the combustor, thereby confirming that thermal-acoustic combustion instability occurred in the combustor. In order to examine the flame structure at the moment of flashback, high-speed OH-PLIF and pressure fluctuation measurement were simultaneously conducted and the phase-locked PIV technique was applied. When the strong flashback occurs, an instantaneous adverse pressure gradient is formed within a combustion instability cycle. Consequently, the generated reverse flow pushed the flame attached at the trailing edge of the bluff body to the upstream from the bluff body. The flame propagated rapidly along the side of the bluff body by the influence of the boundary layer flow and the decreased quenching distance. This propagated flame became the ignition source at the front tip of the bluff body and generated the flame surface that propagated in all directions; thus, it was found to be the primary cause of the increase in the flashback distance. The flame flashback distance also varied depending on the combustor length and the initial flow condition. An attempt was made to concentrate the measured data of flashback distance under various conditions into a single line, and turbulence intensity and combustion instability frequency were the dominant factors that impacted the flashback distance.

Additionally, in order to confirm the applicability of the research results of flashback under more practical conditions, an experiment was conducted using the hydrogen to fuel ratio, the blockage ratio of the perforated plate, and the reactant temperature as variables. The addition of hydrogen increases the flame speed and flashback distance compared to the methane flame. However, when the proportion of

hydrogen exceeds 50%, a flashback proceeds to the fuel injector and the condition for which a flashback distance measurement is meaningless, easily occurs. The increase in the blockage ratio of the perforated plate attenuates the turbulence intensity flow in a non-reacting condition. This property decreases the pressure fluctuation, when combustion instability occurs and also the flashback distance. A rise in the reactant temperature increases the flame stability as well as the flame speed, and a flashback does not occur at a high reactant temperature. As the data gathered with the turbulence intensity and the instability frequency only is incomplete, a modification of the parameters is necessary. The pressure fluctuation data near the orifice is used to represent the pressure fluctuation characteristics of the combustion instability instead of the data at the position of the bluff body. Additionally, the turbulent flame speed is considered to represent the laminar flame speed and the turbulence intensity in each condition. Consequently, using the modified parameters, the relationship amongst the velocity fluctuation, turbulent flame speed, mean velocity, and the combustion instability frequency, and the factors affecting the flashback are confirmed by effectively collecting the experimental results obtained for various cases, including the methane flame condition.

Keywords: Premixed Flame, Turbulent Flame, Bluff Body Flame, Lean Blowoff, Acoustic Excitation, Damkhöler Number, Resonance, Thermo-acoustic Combustion Instability, Flashback, Turbulence Intensity, Combustion Instability Frequency, Flame Speed, PIV, OH PLIF

Student Number: 2010-20721

LIST

ABSTRACT	i
LIST	iv
LIST OF FIGURES.....	vi
LIST OF TABLES	x
NOMENCLATURE.....	xi
CHAPTER 1	
INTRODUCTION	1
CHAPTER 2	
EXPERIMENT AND MEASUREMENT SYSTEMS.....	9
2.1 Combustor	9
2.2 Flame Imaging.....	11
2.2.1 Chemiluminescence Spectroscopy.....	11
2.2.2 OH PLIF Measurements	13
2.2.3 PIV Measurements.....	18
CHAPTER 3	
EFFECT OF ACOUSTIC EXCITATION ON LEAN BLOWOFF IN TURBULENT PREMIXED BLUFF BODY FLAEMS	21
3.1 Background and Objectives	21
3.2 Experimental Methods.....	22
3.3 Characteristics of Lean Blowoff under Stable Flame Conditions	27
3.4 Characteristics of Lean Blowoff with Acoustic Excitation.....	34
3.5 Hypothesis of the Blowoff Mechanism	40
CHAPTER 4	

FLASHBACK CHARACTERISTICS COUPLED WITH COMBUSTION	
INSTABILITY IN TURBULENT PREMIXED BLUFF BODY FLAMES	50
4.1 Background and Objectives	50
4.2 Experimental Methods.....	51
4.3 Comparison of One Cycle of the Flashback with Different Conditions	53
4.4 Combustion Instability Characteristics with Flashback.....	55
4.5 Characteristics of the Strong Flashback Phenomenon.....	57
4.6 Factors Affecting the Flashback Distance	62
 CHAPTER 5	
EFFECT OF HYDROGEN/PERFORATED PLATE/REACTANT TEMPERATURE	
ON THE FLAHSBACK IN BLUFF BODY FLAMES	66
5.1 Background and Objectives	66
5.2 Experimental Methods.....	68
5.2.1 Experimental Apparatus	68
5.2.2 Experimental Conditions.....	69
5.3 Effect of Hydrogen/Methane Fuel on the Flashback	71
5.4 Effect of Perforated Plate on the Flashback.....	74
5.5 Effect of the Reactant Temperature on the Flashback	78
5.6 Relationship between the Experimental Conditions and Flashback Distance	80
 CHAPTER 6	
CONCLUSION	85
 APPENDIX A. VOLATGE ADJUSTMENT	89
APPENDIX B. SOUND PRESSURE LEVEL	91
 REFERENCES.....	92
 ABSTRACT IN KOREAN	102

LIST OF FIGURES

Fig. 1.1	Flow topology and the velocity field of the bluff body, adapted from Shanbhogue (1999) [2].	2
Fig. 1.2	Diagram of the interactions between the contributory factors in the combustion instability, adapted from Candel (2002) [30].	5
Fig. 1.3	Outline of the objective for this thesis.	8
Fig. 2.1	Overall schematic of the confined combustor with the bluff body.	10
Fig. 2.2	Schematic of energy transfer process. Relaxation processes emission of photons.	13
Fig. 2.3	OH excitation spectrum; in this study, $Q_1(6)$ was used for OH PLIF.	14
Fig. 2.4	OH fluorescence spectrum for $Q_1(6)$.	15
Fig. 2.5	Transmittance of UG11 (left) and WG305 (right).	16
Fig. 2.6	Principle of typical PIV system.	19
Fig. 3.1	Schematic of the combustor overall shape and the bluff body with the acoustic device.	23
Fig. 3.2	Schematic of the phase-locked PIV experimental setup.	27
Fig. 3.3	(a) Relationship between Φ_{bo} and $Re_{d, lip}$ for various geometric conditions, (b) The recirculation zone size with various geometric conditions for the bluff body without a nozzle.	29
Fig. 3.4	Images of OH radical chemiluminescence without excitation with a 14 mm v-gutter bluff body at $U_{lip} = 16.1$ m/s and $\Phi_{bo} = 0.457$; (a) near blowoff, (b) close to blowoff.	31
Fig. 3.5	Results of the relationship between $Da_{blowoff}$ and $Re_{D, lip}$ for studies based on methane fuel: two-dimensional and confined case (Δ , \blacktriangle , ∇ and \blacktriangledown), axisymmetric and confined case (\odot), axisymmetric and unconfined case (\bullet and \star).	33
Fig. 3.6	Images of OH radical chemiluminescence with a 10 mm v-gutter bluff	36

- body at $\dot{m}_a = 15$ g/s; (a) stable flame without acoustic excitation, (b) far from the blowoff ($f_{ex} = 170$ Hz) with acoustic excitation, (c) close to the blowoff ($f_{ex} = 170$ Hz, $\Phi_{bo} = 0.568$) with acoustic excitation.
- Fig. 3.7 Variations in the tendency of Φ_{bo} corresponding to the frequency and intensity of excitation in the range of (a) 150-400 Hz and (b) 150-1000 Hz ($\dot{m}_a = 15$ g/s). 37
- Fig. 3.8 POD analysis; (a) Images of the POD results (upper row) and OH radical chemiluminescence (lower row) at the first four modes of the stable flame with a 10 mm bluff body at $U_{lip} = 14.9$ m/s, (b) Comparison of the frequency trend of the POD analysis and Φ_{bo} . 39
- Fig. 3.9 Φ_{bo} trend of the excitation frequency; (a) Comparison of the trends of the blowoff equivalence ratio in two different cases, (b) The trends of blowoff equivalence ratio and harmonic frequencies along the $L_{com} = 2015$ mm combustor, (c) The trends of blowoff equivalence ratio and harmonic frequencies along the $L_{com} = 1615$ mm combustor. 42
- Fig. 3.10 Trends of the velocity fluctuation and the blowoff equivalence ratio with harmonic frequencies of the combustor using the two-microphone method. 43
- Fig. 3.11 Changes in the maximum transverse velocity; (a) One cycle of the maximum transverse velocity in $f_{ex} = 190$ Hz, (b) Phase-lock velocity field vectors subtracted from half of the center line x-axis velocity, overlapped by the contour image of average y-axis velocity. 45
- Fig. 3.12 (a) The velocity fluctuation measured by the two-microphone method ($L_{com} = 2150$ mm), (b) The distribution of the maximum transverse velocity at each phase with the excitation frequencies. 46
- Fig. 3.13 The averaged PIV images and the structural changes of the recirculation zone during one cycle of excitation frequency (30° , 120° , 210° , 300° , and average); (a) $f_{ex} = 190$ Hz (close to the f_{har}), (b) $f_{ex} = 230$ Hz (far from the f_{har}). 48

Fig. 3.14	Logic process describing the hypothesis for lean blowoff mechanism with excitation.	49
Fig. 4.1	Schematic diagram of the combustion section.	52
Fig. 4.2	Images of phase-resolved OH-PLIF in the vicinity of the bluff body during one period of (a) weak flashback ($U_{\text{mean}} = 7.8$ m/s, $\Phi = 0.55$); (b) strong flashback ($U_{\text{mean}} = 7.8$ m/s, $\Phi = 0.80$).	54
Fig. 4.3	The amplitude of the pressure fluctuation and frequency of the combustion instability for various U_{mean} and Φ ; (a) $L_{\text{coldzone}} = 1.0$ m; (b) $L_{\text{coldzone}} = 1.3$ m.	56
Fig. 4.4	Rayleigh Index of the weak flashback condition and the strong flashback condition; (a) the trend of Rayleigh Index over time; (b) the normal distribution of Rayleigh Index.	57
Fig. 4.5	(a) The dynamic pressure graph during one period of a strong flashback ($U_{\text{mean}} = 7.8$ m/s, $\Phi = 0.8$); (b) the instantaneous OH-PLIF images from 63° to 110° ; (c) the instantaneous OH-PLIF images from 130° to 240° .	59
Fig. 4.6	The PIV images (lower half) and the OH-PLIF images (upper half) of a strong flashback condition ($U_{\text{mean}} = 7.8$ m/s, $\Phi = 0.8$) at (a) the 110° phase and (b) the 160° phase.	61
Fig. 4.7	The V_f in the vicinity of the bluff body using OH-PLIF images of the flame edge ($U_{\text{mean}} = 7.8$ m/s and $\Phi = 0.8$); (a) the calculation method of the V_f ; (b) the trends of the V_f at different positions.	62
Fig. 4.8	The flashback distance for various U_{mean} and Φ ; (a) $L_{\text{coldzone}} = 1.0$ m; (b) $L_{\text{coldzone}} = 1.3$ m.	64
Fig. 4.9	Results of the relationship between D_{FB} and I/f_{CI} for various flow and geometric conditions.	65
Fig. 5.1	Schematic of the combustor with an electric air heater, hydrogen feeding device, and the perforated plate position.	69
Fig. 5.2	Design of the perforated plate with various blockage ratios.	70

Fig. 5.3	S_L of the hydrogen/methane flame with respect to the amount of hydrogen added (calculated using the GRI 3.0 mechanism).	73
Fig. 5.4	Relationship amongst the D_{FB} , the measured pressure fluctuation, and the f_{CI} under hydrogen/methane flame conditions.	73
Fig. 5.5	Turbulence intensity of the non-reacting flow with respect to the blockage ratio of the perforated plate.	74
Fig. 5.6	Relationship amongst the D_{FB} , the measured pressure fluctuation, and the f_{CI} under various blockage ratio conditions.	76
Fig. 5.7	Magnitude of the pressure perturbation with respect to the blockage ratio of the perforated plate; (a) near the uppermost region of the combustor and (b) near the bluff body.	77
Fig. 5.8	S_L as per the equivalence ratio under various reactant temperature conditions (calculated using the GRI 3.0 mechanism).	79
Fig. 5.9	Relationship amongst the D_{FB} , the measured pressure fluctuation, and the f_{CI} with respect to the reactant temperature (The filled symbol and hollow symbols indicate the constant velocity conditions and the constant flow rate conditions, respectively).	80
Fig. 5.10	Images of OH radical chemiluminescence in the vicinity of the bluff body during one period of (a) H_2/CH_4 flame case ($H_2/CH_4 = 50\%/50\%$, $U_{mean} = 10.4$ m/s, $\Phi = 0.80$); (b) perforated plate case ($BR = 0.5$, $U_{mean} = 10.4$ m/s, $\Phi = 0.85$); (c) reactant temperature case ($T = 373$ K, $U_{mean} = 10.4$ m/s, $\Phi = 0.90$).	82
Fig. 5.11	Relationship between the D_{FB} and I_{flame}/St_{flame} for various initial conditions.	84
Fig. A.1	Measured sound pressure with excitation frequency variations.	90
Fig. A.2	Adjusted voltage with excitation frequency variations.	90

LIST OF TABLES

Table 2.1	Formation and destruction of OH radical.	14
Table 2.2	High-speed PLIF application research summary.	17
Table 3.1	Experimental conditions for non-forced and forced flames.	24
Table 4.1	Location of the combustor parts and the dynamic pressure sensors.	52
Table 5.1	Experimental conditions with each case.	71
Table B.1	Sound pressure and excitation intensity.	91

NOMENCLATURE

Alphabet

BR	blockage ratio
CI	combustion instability
c	speed of sound
D	diameter
D_{FB}	flashback distance
Da	Damköhler number
Da_{blowoff}	blowoff Damköhler number
DPS	dynamic pressure sensor
FFT	fast Fourier transform
f	frequency
f	focal length
f_{sh}	frequency of the shear-generated vortex
I	intensity
I	turbulence intensity
L	length
L_{RZ}	axial length of recirculation zone
LHV	lower heating value
$Li(x,t)$	combustion instability damping source
MFC	mass flow controller
\dot{m}	mass flow rate
PID	proportional-integral-derivative
PIV	particle imaging velocimetry
PLIF	planar laser induced fluorescence
PMT	photomultiplier tube
POD	proper orthogonal decomposition
p'	pressure fluctuation

$p'(x, t)$	perturbation of dynamic pressure
q'	heat release fluctuation
$q'(x, t)$	heat release oscillation
Re	Reynolds number
RI	Rayleigh index
ROI	Region of the interest
RZ	recirculation zone
R^2	coefficient of determination
St	Strouhal number
S_L	laminar flame speed
S_T	turbulence flame speed
TMM	two-microphone method
t	time
U	flow velocity
U_b	burning velocity
U_{mix}	velocity of inflowing cold mixture behind the bluff body
U_y	transverse velocity
u'	velocity fluctuation
V_f	propagation velocity of the flame surface

Greek

α	thermal diffusivity
λ	wavelength
ρ	density
Φ	equivalence ratio

Subscript

a	air
bluff	bluff body

bo	blowoff
CI	combustion instability
cold	non-reacting condition
coldzone	region from the orifice to the bluff body
com	combustor
D	hydraulic diameter of the combustor
d	width of the bluff body
ex	excitation
flame	flame condition
FB	flashback
f	fuel
har	harmonic
lip	trailing edge of the bluff body
max	maximum value
mean	mean value
res	resonance

CHAPTER 1

INTRODUCTION

In the past, engines have used a combustor with a diffusion flame, which has a reliable performance and reasonable stability characteristics. This type of combustor has advantages in terms of engine performance, but it generates a large amount of thermal NO_x due to a high reaction temperature, which is a disadvantage [1]. Since the environmental problems caused by global warming phenomena have emerged as a serious issue, the Kyoto Protocol for reducing greenhouse gases was established and regulations on exhaust emissions have been implemented. Therefore, with the need to change the engine's operating condition, a lean premixed flame that can reduce the thermal NO_x emissions at a relatively low temperature during combustion has been widely used.

Although the amount of the emissions in the exhaust is reduced because the combustor is operated under lean premixed conditions, problems related to flame stability have also been encountered as important issues. One issue is the lean blowoff phenomenon that is generated by the reduction of the equivalence ratio in the stable flame condition and another issue is the thermo-acoustic combustion instability that occurs by varying the equivalence ratio in the stable flame condition.

Lean blowoff phenomenon is closely related to the hydrodynamic instability caused by the flow characteristics of the bluff body. Figure 1.1 shows the flow topology of the bluff body [2]. The symmetrical shear layer region is generated between the end point of the boundary layer and the start point of the recirculation zone. In this section, a convective instability, known as Kelvin-Helmholtz instability, exists. The recirculation zone exists from the bluff body trailing edge to the section where the wake flow occurs. Then, there is a section where the shear layers are merged and an asymmetrical wake flow occurs in the downstream of the bluff body. In this section, an absolute instability, known as Bernard-Von Karman instability, exists [3]. In the reacting flow, the vorticity generated by the shear layer and the vorticity generated by the flame (known as the baroclinic

vorticity) are mutually competitive. That is, the flow field near the bluff body is dominated by the vorticity of the shear layer, and the flow field far from the bluff body is dominated by the baroclinic vorticity. The wake structure is affected by the alteration of the entrainment dynamics due to the flame hole in the condition near the blowoff. In addition, the gas extension (such as the density ratio increase due to the flames) attenuates the sinuous behavior of the wake and the fluctuation of the shear layer [2]. However, the relationship between the flow field and the flame becomes important because the exothermicity gradually decreases from the stable flame in the near lean blowoff condition.

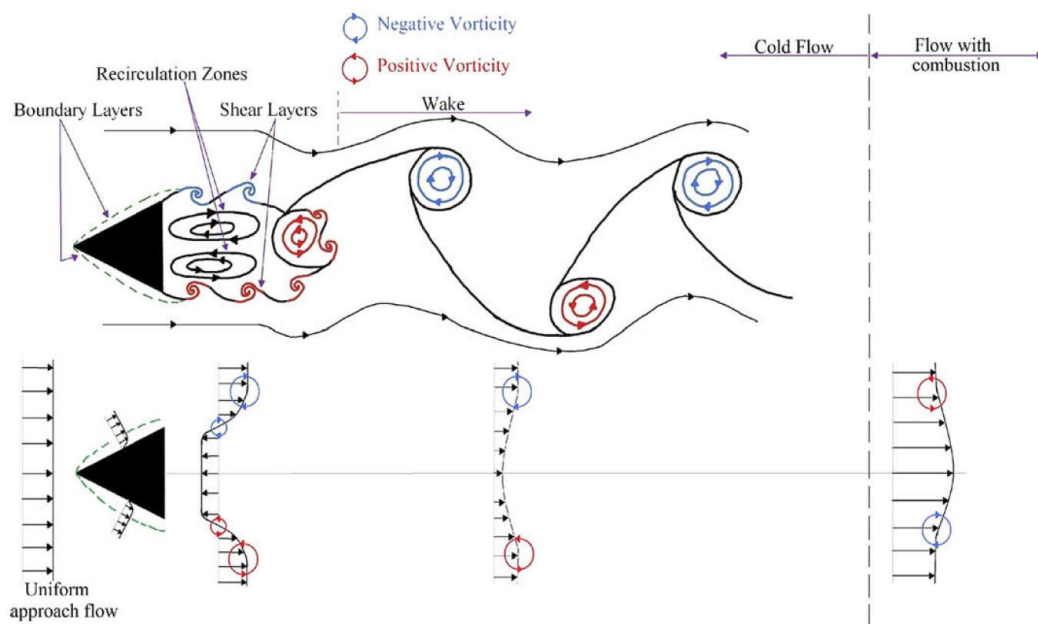


Fig. 1.1. Flow topology and the velocity field of the bluff body, adapted from Shanbhogue (1999) [2].

Because the fundamental objective of the bluff body is to anchor and stabilize the flame, many studies have focused on flame stabilization and blowoff. Several studies have explained that blowoff occurs when the rate of entrainment of the reactants in the

recirculation zone, viewed as a well-stirred reactor, is not proportional to the rate of burning [4, 5]. Another study found that blowoff occurs when the contact time between the combustible mixture and the hot products in the shear layer exceeds the chemical ignition time [6]. Other studies have attributed blowoff to local extinction as a result of excessive flame stretch near the bluff body [7-9]. Shanbhogue et al. summarized and reviewed the history of blowoff research in detail [2]. That paper suggested that blowoff occurs in two stages. The first stage is the localized extinction of the flame sheet that results when the local flame strain rate exceeds the extinction strain rate. The second stage is the large-scale disruption of the wake and the transition of the recirculation zone. However, that study mentioned that this description does not explain all aspects of the blowoff process.

Since Shanbhogue et al. conducted their research, many other have investigated the blowoff process. Chaudhuri et al. conducted a variety of imaging techniques to determine the sequence of events leading to blowoff [10]. Their results indicated that the flame was extinguished when the flow on the shear layer was not reignited by the flame kernel. Tuttle et al. observed that an increase in the distribution of flame stretch causes the extinction of the local flame in vitiated, premixed flows [11]. Other researchers have also derived similar results for the blowoff process [12, 13]. Those studies have suggested that the flame zone was fragmented by the inflow of the cold reactant into the recirculation zone. Additionally, those studies found that the characteristic timescale of the extinction is larger than the characteristic timescale of the combustor.

It is important to understand the effect of self-excited oscillation in order to improve the flame stability because the premixed flame is highly sensitive to that type of oscillation. Toward that end, several groups have conducted studies on flame behavior with acoustic excitation. Several studies have observed the behavior of acoustically forced flames and have attempted to model that behavior using a theoretical formulation [14-16]. Those studies investigated the important factor in spatio-temporal response and analyzed the ensemble-averaged characteristics of a longitudinal forced flame. Other studies have described the measured forced flame characteristics with modeling using the

Large Eddy Simulation (LES) in a swirler [17, 18] and an axisymmetric bluff body [19, 20]. Although the experimental equipment differed in those studies, they all found that the change in the vortex shedding was due to the excitation frequency, which was observed to be a dominant factor that transforms the flame and flow field. In other studies, the response characteristics of the flame were examined using the transfer function by measuring the heat release rate and velocity perturbation [21, 22]. The influences of transversely forcing the flame have also been studied using experimental and numerical analysis [23, 24].

Studies of flame blowoff with acoustic excitation have also been conducted in the same vein. Chaparro and Cetegen demonstrated that the shape of the bluff body affected the blowoff behavior by visualizing the change in the combustion flow field [25]. Chaudhuri et al. explained that the blowoff mechanism of forced flames is different from the mechanism in unforced flames [26]. Biswas et al. confirmed that the phase angle of the maximum strain rate equals the phase angle of the minimum recirculation zone length, and they explained that phenomenon occurs due to the presence of a strong vortex [27].

Thermo-acoustic combustion instability is a self-excited oscillation phenomenon, and it occurs while acoustic oscillation, flow perturbation, and heat release oscillation achieve a feedback loop with each other. Acoustic oscillation is affected by the acoustic boundary, the combustor length, the speed of sound, and the inlet and combustor geometry. Flow perturbation is affected by the fluctuation of the air flow rate and the fluctuation of the fuel flow rate. Heat release oscillation is affected by the flame shape and the flame length. Figure 1.2 shows a diagram of the interactions between the contributory factors in the combustion instability.

Lord Rayleigh determined the criterion for the occurrence of combustion instability [28], this criterion can be expressed as follows [29].

$$\int_V \int_T p'(x, t) q'(x, t) dt dV \geq \int_V \int_T \sum_i L_i(x, t) dt dV \quad (1.1)$$

The left side of the equation shows the driving process and the right shows the damping process. Therefore, there is the potential for the combustion instability to occur when the phase difference between the heat release fluctuation and the acoustic fluctuation is less than the 90° and the generated energy due to the in-phase of two fluctuations is greater than the acoustic energy loss. The combustion instability feedback loop causes a very strong pressure perturbation, which can also cause the flashback of the flame.

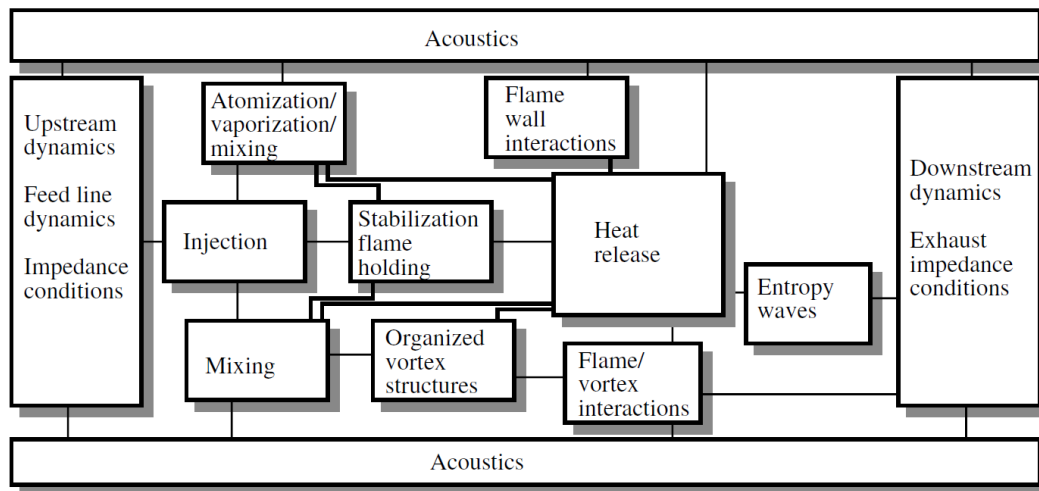


Fig. 1.2. Diagram of the interactions between the contributory factors in the combustion instability, adapted from Candel (2002) [30].

A flashback phenomenon, in which the flame is propagated upstream from the stable region, is one characteristic of the flame in a premixed gas mixture. In general, flashback occurs when the local flame speed exceeds the flow speed; this is caused by a variety of factors. Sommerer et al. [31] briefly described the reasons for flashback, and they divided it into five categories as follows: flashback by autoignition [32], flashback in the boundary layer [33], turbulent flame propagation in the core flow [34], flashback induced by vortex breakdown [35], and combustion instability leading to flashback. When

combustion instability leads to flashback, the phenomenon occurs under combustion instability conditions with a high level of velocity fluctuation and a low unstable frequency. This type of flashback can be seen in a confined premixed combustor using a flame stabilizer, such as the bluff body [36].

Since the 1980s, experimental studies have examined flashback in the bluff body and the rearward facing step. Keller et al. demonstrated that the interactions between the recirculation and the trailing vortices caused the characteristic flame structure, including a flashback [37], and their results were numerically reproduced by Thibaut and Candel [38]. Dowling predicted that the flame distortion induced nonlinear \mathbf{u}' and revealed that the describing function analysis effectively evaluates the limit-cycle characteristics because the analysis reflects the nonlinearity influence [39]. Fureby found that the multiple shear-layer interactions between the flame and the confinement in combustor increased effective reaction rate, which in turn, caused flame wrinkling or flame flapping [40].

Ghoniem et al. showed that the pressure oscillation frequency coincided with the acoustic quarter mode of the combustor tunnel, and that of the absolute mode frequency of the wake mode. Also they investigated that the pressure leads the velocity by 90° as well, that is, it is in phase with the heat release rate in quarter-wave mode [41]. Birbaud et al. investigated the influence of confinement on the dynamics of inverted flames. They changed the diameters of the duct and measured the response. It is found that interaction with the wall strongly influences the dynamics of the flame tip, the flame wrinkling geometry in the vicinity of the boundary, and to a great extent the amplitude of response [42]. Recently, Hong et al. investigated the combustion instability in the backward-facing step combustor with the various parameters (flow-flame interaction; heat transfer by material; and the relationship between heat release and pressure fluctuation). They revealed that the stretch rate, the phase difference between heat release and pressure fluctuation and low-thermal-conductivity material bluff body are the significant parameter to determine the characteristics of dynamic mode because those parameters related to the flame speed. Also, they observed that the combustion instability is suppressed by using the low-thermal-conductivity material bluff body with low heat flux

to the reactant and low flame burning speed. [43-45].

The use of a lean premixed combustor is indispensable to adhere to the increasingly stringent emissions regulations. A complete understanding of the dynamic characteristics of the bluff body flame is essential to improve the reliability of the combustor under lean premixed conditions. Thus, this study aimed to investigate the dynamic characteristics in the turbulence premixed bluff body flames, as shown Figure 1.3. For this purpose, the following studies were performed.

1. In Chapter 3, the blowoff phenomenon was experimentally investigated in the presence of external excitation. The blowoff equivalence ratio was measured using different types of combustor geometry and various flow properties. The flame structure near and close to the blowoff was examined using images of OH radical chemiluminescence. We investigated the effect that frequency variation and the intensity of the external excitation had on the blowoff, and we confirmed that the blowoff equivalence ratio increased at specific frequencies. The blowoff mechanism hypothesis was developed based on those results, and its verification was attempted using particle imaging velocimetry measurements and the two-microphone method.
2. In Chapter 4, the flashback phenomenon coupled with self-excited combustion instability was investigated. In particular, the flashback phenomenon in which the flame propagates to the upstream region of the bluff body was experimentally investigated using pressure fluctuation measurements, high-speed OH* planar laser induced fluorescence, and phase-lock particle imaging velocimetry measurements in turbulent premixed bluff body flames.
3. In Chapter 5, the flashback distance characteristics were examined in the cases of hydrogen supplementation, installation of the perforated plate, and reactant temperature variations. We identified the variables that affect the flashback distance by utilizing the data obtained through the experiment.

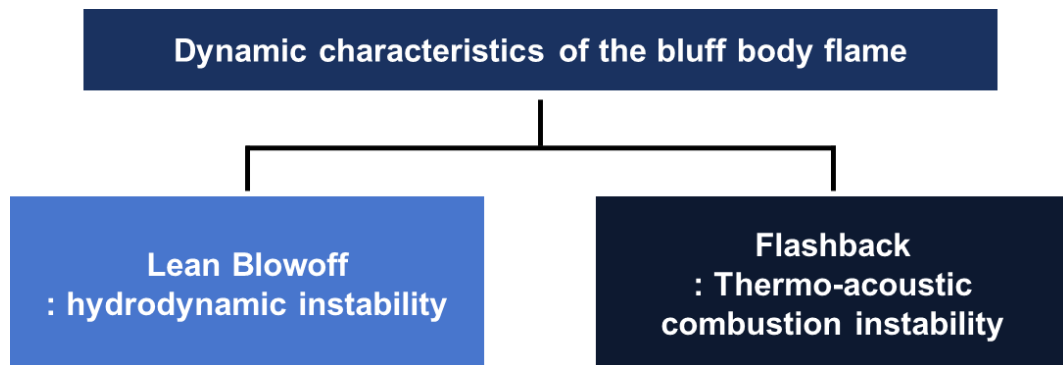


Fig. 1.3. Outline of the objective for this thesis.

CHAPTER 2

EXPERIMENT AND MEASUREMENT SYSTEMS

2.1 Combustor

The experiments were performed in a long duct-shaped combustor with a v-gutter bluff body, as shown in Figure 2.1. The experimental apparatus consisted of three sections—the air-fuel supply, the mixing-combustion section, and data acquisition. An air compressor used to supply influx air can deliver up to 7 bars of compressed air. A mass flow controller (MFC) (TSC-150) was used to control the air mass flow rate that was supplied to the combustor. An orifice with a 5 mm diameter (blockage ratio of 98.8%) was installed at the top of the combustor; this denoted the upper closed acoustic boundary of the mixing-combustion section. The fuel consisted of a natural gas mixture of 89% methane (CH_4) and 9% ethane (C_2H_6); moreover, a small amount of propane, butane, etc. was supplied through a city gas pipeline. Fuel was supplied in the compressed condition of 5 bars and regulated using a MFC (TSC-245).

The mixing-combustion section consists of four parts: the fuel injector, the mixing section, the combustion section, and the nozzle. The mixing-combustion section has a square, 40 mm \times 40 mm cross-section area and a long duct shape in the longitudinal direction. The plane orifice fuel injectors are mounted at the top and bottom of the mixing section. The fuel was injected perpendicular to the airflow direction at 830 mm ahead of the bluff body in the combustion section. Thus, air and fuel were sufficiently premixed while passing through the mixing section at 830 mm before reaching the bluff body [46]. The combustion section consists of a torch igniter, a bluff body, visualization windows, and extension ducts and it has five ports to allow for the installation of a temperature or pressure sensor. A torch igniter used for the initial ignition uses hydrogen (H_2) and air, and it was installed directly below the bluff body. The v-gutter bluff body and triangular bluff body were used. These bluff bodies are shaped like an equilateral triangle, the sides

of which are 10 mm and 14 mm in length. In order to transmit the laser and visualize the flame, quartz windows were installed at the top, bottom, and side of the combustion section. At the end of the extension duct, a nozzle was installed to ensure a fixed acoustic length. The square cross-section area of the nozzle is 40 mm × 20 mm. Normally, the distance between the upper orifice and the nozzle is fixed at about 2000 mm.

For the analysis, the PXI-1042 system (NI Instrument) was used to acquire temperature and static pressure data. A K-type thermocouple (Omega Co.) and a pressure transducer (Valcom Co.) were used to obtain the temperature and static pressure information, respectively. The temperature and static pressure sampling rate was 1 Hz. In addition, a data acquisition (DAQ) board (BNC 9000) was used to obtain the dynamic pressure. Eight dynamic pressure sensors (PCB 102A05) were mounted at the mixing-combustion section using the infinite tube method. Using these sensors, the dynamic pressure signals were measured at various locations in the mixing-combustion sections, simultaneously, and the combustion frequencies and pressure fluctuations were then obtained from the signal processing.

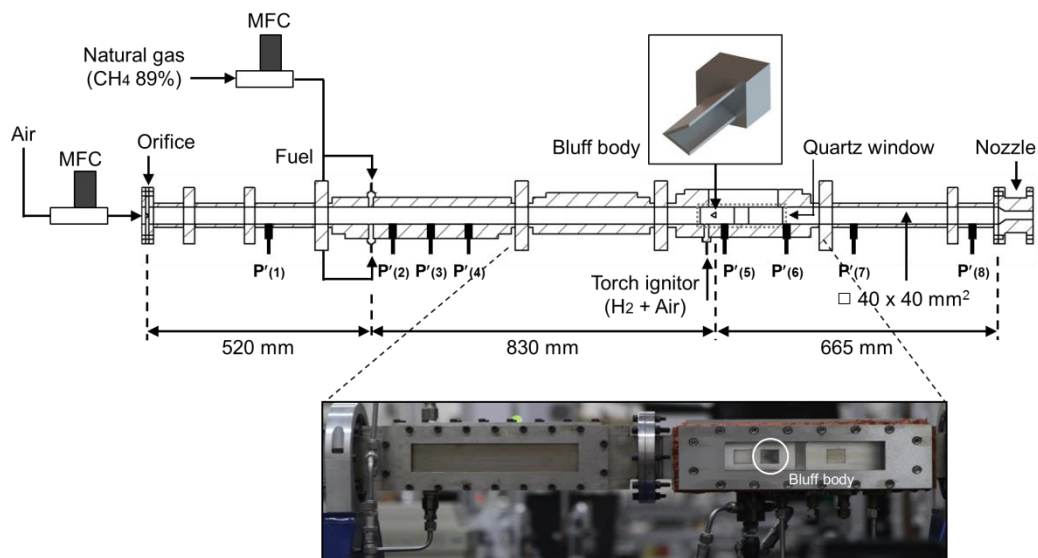


Fig. 2.1 Overall schematic of the confined combustor with the bluff body.

2.2 Flame Imaging

In this study, OH^* chemiluminescence images were recorded to measure flame structure. The OH^* chemiluminescence image should be used since OH radicals are good indicators of the reaction zone, which is a high temperature region where thermal NO_x can be produced. Thus, OH^* images were acquired using a ICCD camera (PI-MAX, Princeton Instruments, 512×512 pixel CCD) with a UV-Nikkor objective ($f = 105$ mm; $f/4.5$) and 307.1 ± 5 nm narrow bandpass filter.

2.2.1. Chemiluminescence Spectroscopy

Chemiluminescence, like atomic emission spectroscopy (AES), uses quantitative measurements of the optical emission from excited chemical species to determine analyte concentration; however, unlike AES, chemiluminescence is usually emission from energized molecules instead of simply excited atoms. The bands of light determined by this technique emanate from molecular emissions and are therefore broader and more complex than bands originating from atomic spectra. Furthermore, chemiluminescence can take place in either the solution or gas phase, whereas AES is almost strictly a gas phase phenomenon. Like fluorescence spectroscopy, chemiluminescence's strength lies in the detection of electromagnetic radiation produced in a system with very low background. And on top of this, because the energy necessary to excite the analytes to higher electronic, vibrational, and rotational states (from which they can decay by emission) does not come from an external light source like a laser or lamp, the problem of excitation source scattering is completely avoided. The major limitation to the detection limits achievable by chemiluminescence involves the dark current of the photomultiplier (PMT) necessary to detect the analyte light emissions. If the excitation energy for analytes in chemiluminescence doesn't come from a source lamp or laser, where does it come from? The energy is produced by a chemical reaction of the analyte and a reagent. An example of a reaction of this sort is shown below:



In gas phase chemiluminescence, the light emission (represented as $h\nu$) is produced by the reaction of an analyte (dimethyl sulfide in the above example) and a strongly oxidizing reagent gas such as fluorine (in the example above) or ozone, for instance. The reaction occurs on a time scale such that the production of light is essentially instantaneous; therefore, most analytical systems simply mix analytes and the reagent in a small volume chamber directly in front of a PMT. If the analytes are eluting from a gas chromatographic column then the end of the column is often fed directly into the reaction chamber itself. Since as much of the energy released by the reaction should (in the analyst's eye) be used to excite as many of the analyte molecules as possible, loss of energy via gas phase collisions is undesirable, and therefore a final consideration is that the gas pressure in the reaction chamber be maintained at a low pressure (~ 1 torr) by a vacuum pump in order to minimize the effects of collisional deactivation. It must be stated that the ambiguous specification of "products" in the above reaction is often necessary because of the nature and complexity of the reaction. In some reactions, the chemiluminescent emitters are relatively well known. In the above reaction the major emitter is electronically and vibrationally excited HF; however, in the same reaction, other emitters have been determined whose identities are not known and these also contribute to the total light detected by the PMT. To the analytical chemist the ambiguity about the actual products in the reaction is, in most cases, not important. All the analyst cares about is the sensitivity of the instrument (read detection limits for target analytes), its selectivity—that is, response for an analyte as compared to an interfering compound, and the linear range of response. In chapter 3 and 5, OH^* chemiluminescence measurements were conducted to obtain the reaction region.

2.2.2. OH PLIF Measurement

Laser induced fluorescence (LIF) is described as the absorption of a photon by a molecule or radical, followed by an emission of a photon as the molecule undergoes the transition from a higher level energy state to a lower one. Figure 2.2 shows the schematic of energy transfer process. Some of the molecules will relax to the initial state by emission of photon. Several relaxation processes are possible including (a) spontaneous emission, (b) stimulated emission by exterior stimulus, (c) quenching by collision of molecules, (d) redistribution of energy level, and (e) change of molecular component by chemical reaction. However, the rapid or spontaneous emissions of photons are termed as LIF. The frequency of LIF signal can have different value from that of inducing laser beam.

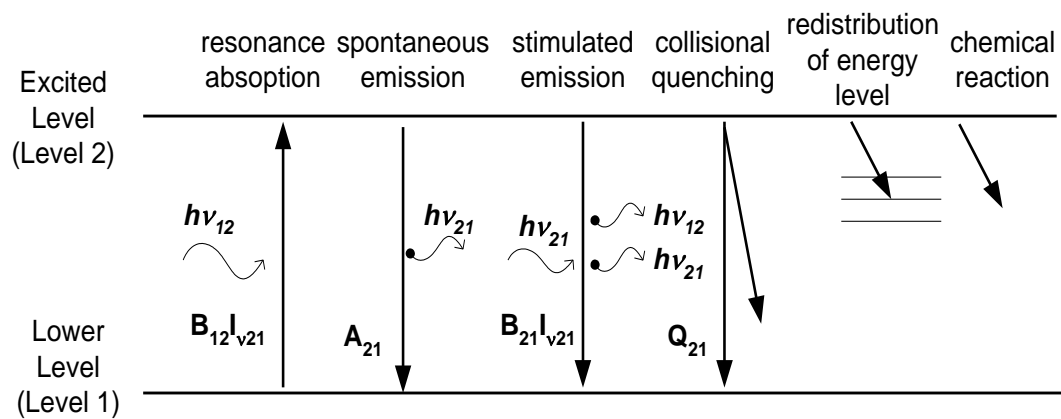


Fig. 2.2 Schematic of energy transfer process. Relaxation processes emission of photons.

OH PLIF was used to obtain spatially and temporally resolved images of the reaction zone in various combustors. As described in Table 2.1, the OH radical concentration increases rapidly around the flame in about 20 μsec and then decomposes slowly in 1 to 5 ms by a 3-body recombination reaction [47]. Thus, near the flame front exists super-equilibrium OH. The OH radical, which is intermediate product of chemical reaction, has a concentration of more ten times than that of O or H radicals [48]. Therefore, the OH

radical is found to emit more intensive fluorescence signal than other species when absorbing laser light. Hence, the fluorescence signal of OH radical is widely used as an indicator of flame front in reacting flows.

Table 2.1 Formation and destruction of OH radical.

Fast OH formation by two-body reactions (1~5nsec)
$\text{H} + \text{O}_2 \leftrightarrow \text{OH} + \text{O}$
$\text{O} + \text{H}_2 \leftrightarrow \text{OH} + \text{H}$
$\text{H} + \text{HO}_2 \leftrightarrow \text{OH} + \text{OH}$
Slow destruction by three-body recombination reactions (~20μsec)
$\text{H} + \text{OH} + \text{M} \leftrightarrow \text{H}_2\text{O} + \text{M}$

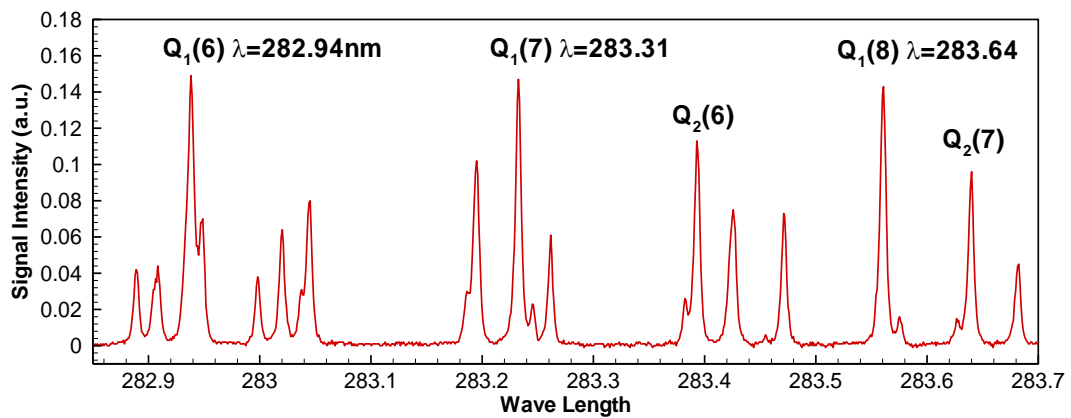


Fig. 2.3 OH excitation spectrum; in this study, Q₁(6) was used for OH PLIF.

To observe the line positions for transition, we scanned the dye laser and recorded the signal at each step. We intended to use $Q_1(6)$ transition of the $A^2\Sigma^+ \leftarrow X^2\Pi (v' = 1, v'' = 1)$ band ($\lambda = 282.94$ nm) for the excitation wavelength and to collect the fluorescence signal from the $A-X (1, 0)$ and $(0, 0)$ bands ($\lambda = 306 \sim 320$ nm). Using monochromator and PMT (photo-multiplier tube), in conjunction with a test flame in laminar premixed condition, a laser excitation scan was performed over the range of interest from $\lambda = 282.5$ nm to $\lambda = 283.5$ nm with 0.001 nm step. The monochromator was fixed at 315 nm to collect the fluorescence. The signal was multiplied by PMT and recorded through the boxcar averager. At every scanning step, 10 pulses of signal were recorded and averaged. After scanning the dye laser, the OH excitation spectrum can be obtained as shown in Figure 2.3. Among the peak values of excitation spectrum, we used $Q_1(6)$ as the excitation wavelength of OH radical.

When the location of $Q_1(6)$ line was detected, the fluorescence spectrum could be obtained by recording the LIF signal at each scanning step of the monochromator. Figure 2.4 is OH fluorescence spectrum graph for $Q_1(6)$. Peak value is found at 320nm.

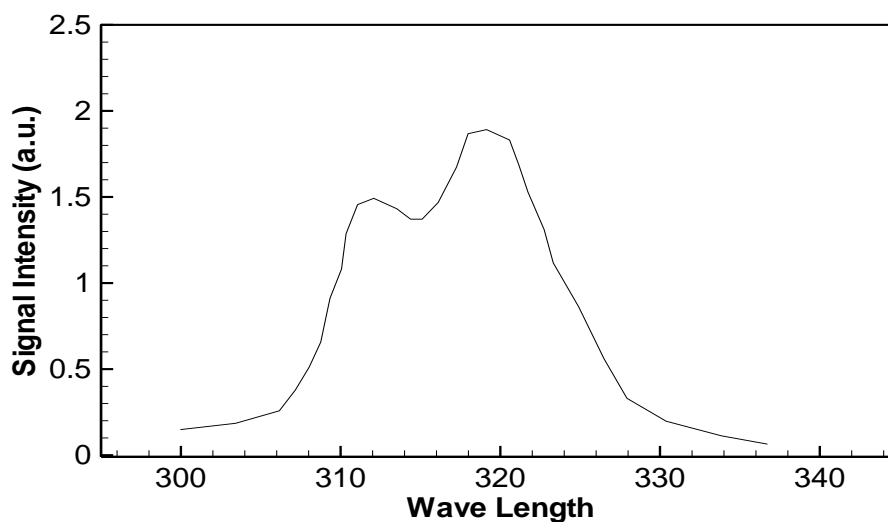


Fig. 2.4 OH fluorescence spectrum for $Q_1(6)$.

PLIF System

For OH PLIF, an Nd:YAG pumped dye laser was turned to $Q_1(6)$ transition of the $A^2\Sigma^+ \leftarrow X^2\Pi (v' = 1, v'' = 1)$ band ($\lambda = 282.94$ nm). $Q_1(6)$ transition line is generally used in the measurement of molecular concentration because it has large LIF signal and the dependency for temperature is low. Fluorescence from the $A-X (1, 0)$ and $(0, 0)$ bands ($\lambda = 306 \sim 320$ nm) were collected with a UV-Nikkor 105 mm/f 4.5 objective. Because UV light cannot penetrate the common glass, all the lenses should be made with quartz. The region of interest was focused onto the ICCD camera of Princeton Instrument (PI-MAX 1K). Two filters (WG-305 and UG-11) were used to block scattered signal lights. Transmittance of each filter is shown in Figure 2.5.

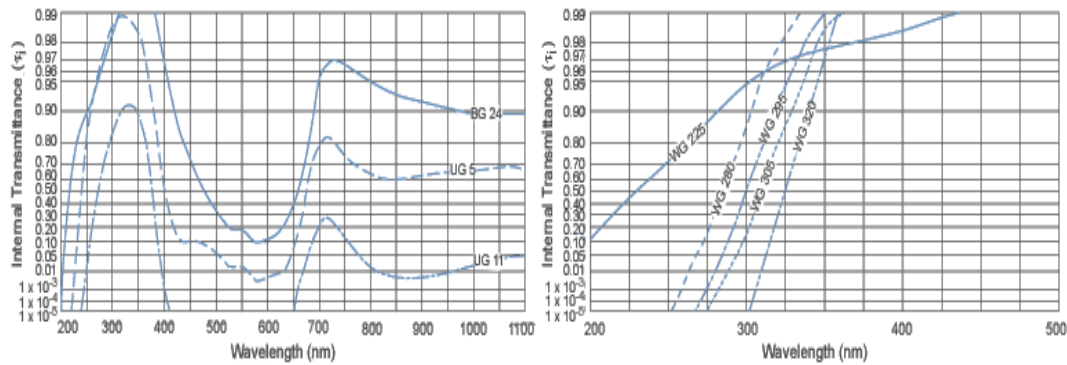


Fig. 2.5 Transmittance of UG11 (left) and WG305 (right).

High Speed PLIF System

High speed laser measurement widely applied in various research fields to find the unknown characteristics of high frequency phenomenon. Many research groups are conducting experimental approach about CH_4/Air flame, Liquid fuel flame and micro structure of the flame. The detailed information about the research is summarized in Table 2.2.

Table 2.2 High-speed PLIF application research summary

Research Group	Year	Author	Contents	Repetition Rate
DLR	2013	M. Stohr	Simultaneous measurement of PIV & OH PLIF in CH ₄ swirling flame [49]	10kHz
DLR	2011	M. Stohr	Blow off characteristics of CH ₄ swirling flame [50]	5kHz
DLR	2010	I. Boxx	Simultaneous measurement of transient phenomena in a partially premixed swirl flame [51]	5kHz
CNRS	2012	P. Petersson	Simultaneous high-speed PIV & OH-PLIF about coaxial diffusion flame burner [52]	10kHz
CNRS	2014	P. Xavier	Cavity flame anchoring characteristics based on high-speed OH-PLIF [53]	10kHz
University of Cambridge	2011	J.R. Dawson	Near blow-off characteristics of bluff body stabilized CH ₄ flame [54]	5kHz
University of Cambridge	2012	N.A. Worth	Flame interaction of CH ₄ /air conical bluff-body stabilized flame [55]	5kHz
AFRL	2013	S. Hammack	Plasma-enhanced flame characteristics of turbulent non-premixed flame [56]	10kHz
Michigan University	2015	P.M. Allison	CH ₂ O-PLIF measurements in dual-swirl burner [57]	4kHz
Sydney University	2011	S. Meares	High-speed OH-PLIF imaging of extinction and re-ignition [58]	5kHz

In this study, the high harmonic instability frequencies were measured and the application of high-speed OH-PLIF is necessary to find the high frequency structural characteristics. High-speed OH-PLIF was set up at the rate of 7 kHz. The 7 kHz OH-PLIF used the laser beam from an Nd:YAG laser (Edgewave, IS-200-L) as the pumping source for the dye laser (Sirah, Credo-Dye-LG-24) and the OH fluorescence signal was measured by an intensifier (HS-IRO), a high speed camera (HSS8), a UV lens (f/2.8), and a bandpass filter (307±10 nm).

2.2.3. PIV Measurement

A particle image velocimetry (PIV) is the measurement technique, which obtains the velocity vector fields of a flow by comparing consecutive two images. The experimental set-up of PIV system consists of several sub-systems: light source system, detecting system, and particle seeding system as shown in Figure 2.6. Small particles have to be seeded into flow to perform PIV technique because PIV measures only the velocity of particles by comparing the displacement of the particle images illuminated by the sequential light pulses, not the flow itself.

Generally, a double pulsed Nd:YAG laser is used as a light source and a high speed CCD camera is employed to obtain instantaneous particle images at a measurement plane. There are no specific rules for particle seeding system; however, the size of particle should be determined by considering whether particles can follow the flow well or not [32]. In most cases, it is necessary to add tracer particles into the flow. These particles are illuminated at the measurement plane of the flow at least twice times within a short interval. The light scattered or fluoresced by particle is recorded either on a single frame or on sequential frames. The displacement of the particle images recorded by the light pulses is calculated through evaluation of the PIV.

To calculate the displacement of the particles grabbed by a CCD camera, it is necessary to divide the image into a grid. The grid is called as an interrogation spot. After setting the interrogation spot size, one interrogation spot of the first images is picked and compared with all the interrogation spot of the second images. The displacement between the interrogation spot of the first image and the interrogation spot of the second image represents one vector of flow field. By conducting this work in all the interrogation spots, whole vectors of flow-field are obtained. This process is called as a correlation.

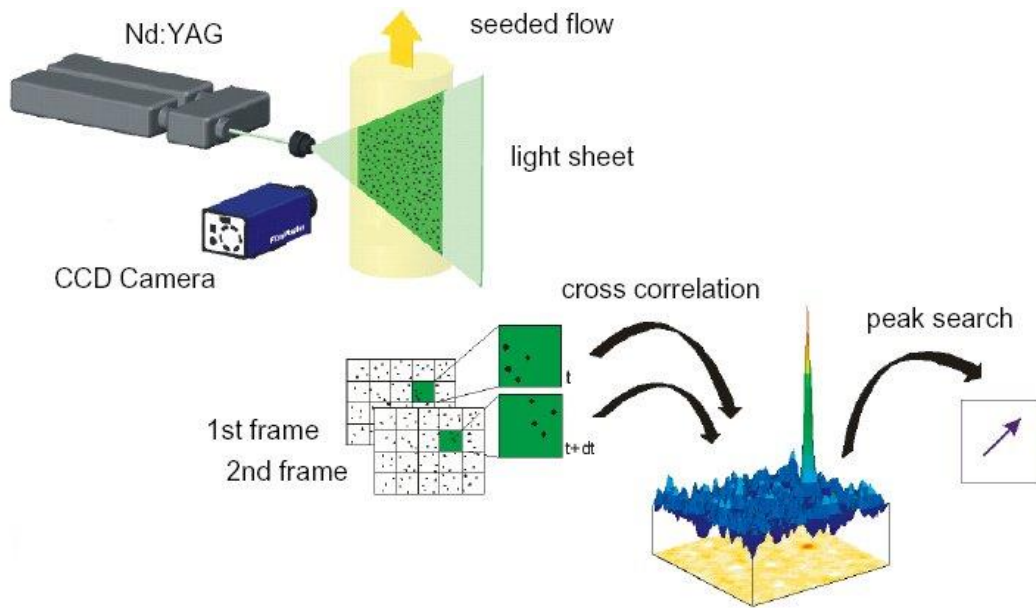


Fig. 2.6 Principle of typical PIV system.

The correlation function is expressed as follows:

$$h(s_x, s_y) = \int_0^{\infty} \int_0^{\infty} f(x, y)g(x + s_x, y + s_y)dx dy \quad (2.2)$$

The expression can become simple as conducting Fourier transformation for a convenience's sake in calculating. Here, F and G are Fourier transformed function of each f and g , and they mean Fourier transform operator.

$$F(h) = F^*(f) \times F(g) = F^* \times G \quad (2.3)$$

$$h = F^{-1}(F^* \times G) \quad (2.4)$$

Equation 2.2 is the same expression of spatial masking in an image processing technique. Thus, it means that a correlation is a kind of masking concepts. According to this concept, the correlation can be called as a process to figure out distribution of the similarity by signal distribution in an image plane. Equation 2.4 makes us use fast Fourier transform (FFT) algorithm which reduces the calculation time drastically. The interrogation spot size of $2n \times 2n$ should be chosen to use FFT algorithm because FFT algorithm is a method by dividing even and odd terms. However, the calculation time becomes short by $\log_2 N/N$ times comparing with direct Fourier transform (DFT) algorithm.

A correlation method is separated into auto-correlation and cross-correlation by the number of functions. Mathematically, auto-correlation is the case; $f(x; y) = g(x; y)$ in Eq. 2.5 and cross-correlation is the case; $f(x; y) \neq g(x; y)$. Experimentally, an auto-correlation is used for the case where the first image at $t = t_1$ and the second image at $t = t_2$ are recorded in one frame (called as a single frame/double exposure mode) and cross-correlation is used for the case where the first image at $t = t_1$ and the second image at $t = t_2$ are recorded in separated frames (called as a double frame/single exposure mode). Comparing with an auto-correlation method, a cross-correlation method has some merits as follows:

1. Directional ambiguity problem can be avoided easily.
2. The algorithm is simple because there is only one peak as a result of correlation.
3. Dynamic range is relatively large.

However, it was difficult to satisfy hardware requirements for cross-correlation. Specially, a time interval was a problem in most cases because the device, which satisfied both high resolution condition and short time interval (microsecond), was very expensive. Nowadays, it becomes relatively inexpensive and popular. Thus, most PIV systems use a cross-correlation method.

CHAPTER 3

EFFECT OF ACOUSTIC EXCITATION ON LEAN BLOWOFF IN TURBULENT PREMIXED BLUFF BODY FLAMES

3.1 Background and Objectives

Research on premixed flame stabilization in a high-speed flow has been actively conducted since mid-20th century, and various flame-holding methods have been designed for flame stabilization. The common goal of these research studies has been to provide a space inside the combustor to reduce the velocity of the flow so that the flame is anchored and maintained in that space. The bluff body is commonly targeted to stabilize the flame. The bluff body sustains the flame by means of the recirculation zone (RZ) that is generated behind it. Hot burned gases exist in the recirculation zone and act as an ignition source for the unburned mixtures to ensure continuous combustion. Since Zukoski's [59] and Roshko's [60] papers were published in the 1950s, numerous studies have been carried out to understand the flow characteristics and combustion stabilization that occur near the bluff body [9, 61, 62]. Prior research has shown that geometric properties and inflow flow characteristics have a major effect on the flow characteristics near the bluff body.

Since the 1950s, a number of studies have been conducted on lean blowoff characteristics [4-9]. Shanbhogue et al. reviewed and summarized the history of blowoff research in detail. That study suggested that blowoff occurs in two stages [2]. The first stage is the localized extinction of the flame sheet that results when the local flame strain rate exceeds the extinction strain rate. The second stage is the largescale disruption of the wake and the transition of the recirculation zone. Many other studies have investigated the blowoff process. Chaudhuri et al. conducted a study using a variety of imaging

techniques to determine the sequence of events leading to blowoff [10]. Their results indicated that the flame was extinguished when the flow on the shear layer was not reignited by the flame kernel. Tuttle et al. observed that an increase in the distribution of the flame stretch causes the extinction of the local flame in vitiated, premixed flows [11]. Other researchers have also derived similar results for the blowoff process [12, 13]. Those studies have suggested that the flame zone was fragmented by the inflow of the cold reactant into the recirculation zone. Those studies also found that the characteristic timescale of the extinction is larger than the characteristic timescale of the combustor.

It is important to understand the effect of self-excited oscillation in order to improve the flame stability because the premixed flame is highly sensitive to that type of oscillation. However, the blowoff with acoustic excitation is a phenomenon that is least understood because it has only been studied in recent years [25-27]; and the blowoff without acoustic excitation has not yet been completely identified.

Therefore, previous studies have all presented very significant results, it is still necessary to understand the blowoff phenomenon with acoustic excitation in more detail. In this current study, the blowoff phenomenon was experimentally investigated in a confined duct combustor. When local extinction of the flame occurred, we compared the conditions under which the flame recovered or proceeded to blowoff. In particular, we investigated the effect that frequency variation and the intensity of the external excitation had on the blowoff. The obtained results revealed the decisive factor that affected the blowoff.

3.2 Experimental Methods

The overall schematic of the combustor is provided in Figure 2.1. The position of an acoustic device, the x and y directions, and the detail of the combustion section are described in Figure 3.1. For external excitation, a speaker (SU-150EF) was placed 105 mm downstream from the orifice on the side of the combustor wall. In this chapter, the

bluff bodies (v-gutter type and triangle type) were in the shape of an equilateral triangle, the sides of which were either 10 mm or 14 mm. The shape of the bluff body was varied in the experiment without the excitation, while the shape of the bluff body was fixed as v-gutter with side of 10 mm in the excitation experiment.

Combustion tests were performed under various inlet air mass flow rate (\dot{m}_a) conditions, ranging from 10 g/s to 25 g/s in steps of 2.5 g/s, under ambient conditions. An air flow transducer (Kanomax 6332D) and probe (Kanomax 0964-01) were used to measure the flow velocity corresponding to the air mass flow rate. The equivalence ratio (Φ) was regulated from 0.4 to 0.7. The air mass flow rate was fixed and the fuel mass flow rate decreased for observation of the blowoff. The blowoff equivalence ratio was measured while the fuel mass flow rate was reduced by 2 slpm (about 0.02 g/s) using the MFC near the blowoff conditions.

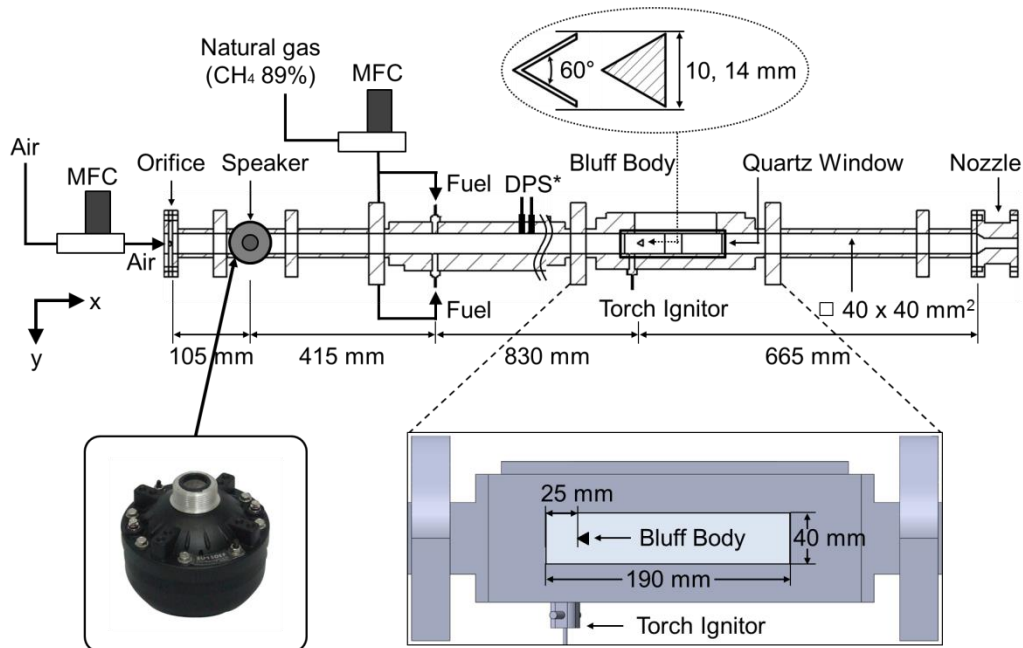


Fig. 3.1 Schematic of the combustor overall shape and the bluff body with the acoustic device.

In this experiment, the intensity and frequency of excitation were the important variables used to study the blowoff characteristics. However, excitation intensity varies depending on the frequency due to the speaker's characteristics if the input voltage to the speaker is the same. To maintain equal intensity depending on the excitation frequency, the voltage applied to the acoustic device was compensated. Accordingly, the excitation frequency (f_{ex}) ranged from 150 Hz to 1 kHz, and the excitation intensity (I_{ex}) was adjusted within 86.7–98.9 dB. The velocity fluctuation in the combustor has a tendency to change depending on the excitation frequency and the excitation intensity. For example, the velocity fluctuation was 0.15–2.7 m/s (mean velocity of 1.5–26%) in the combustion condition ($\dot{m}_a = 15$ g/s, $\Phi = 0.5$) when the excitation intensity was 96.1 dB. These experimental conditions are summarized in Table 3.1.

Table 3.1 Experimental conditions for non-forced and forced flames.

Parameter	Condition	
	w/o excitation	w/ excitation
Inlet Air Mass flow (g/s) (Bulk velocity (m/s))	10 – 25 (5.2 – 13.0)	15 (7.8)
Fuel Type	Natural Gas (CH ₄ 89%, C ₂ H ₆ 9%)	
Mixture Temperature	Room Temperature	
Equivalence Ratio	0.40 – 0.80	
Bluff Body Length (mm)	10, 14	10
Bluff Body Shape	v-gutter, triangular	v-gutter
Excitation Frequency Range (Hz)	-	150 – 1000
Excitation Intensity (dB)	-	86.7 – 98.8
Boundary Condition	closed-open (w/o, w/ nozzle)	closed-open (w/o nozzle)

To observe the structure of and changes in the flame, OH radical chemiluminescence images were obtained using an intensified charge-coupled device (ICCD) high-speed camera (Photron FASTCAM Ultima II) with a 105 mm macro lens (Canon). The camera had a resolution of 1024×512 pixels and the frame rate was set to 4000 fps. A 310 nm band-pass filter with 10 nm bandwidth was placed in front of the high-speed ICCD camera. And, the two-microphone method (TMM) is usually utilized to measure the reflection coefficient, and this can be applied to the calculation of the velocity fluctuation [63]. In Euler's equation, a relationship between the pressure and the velocity fluctuation is expressed as follows [64]:

$$\rho \frac{\partial u'}{\partial t} + \frac{\partial p'}{\partial x} = 0 \quad (3.1)$$

Rearranging the above equation, the following equation is obtained:

$$u'(t + \Delta t, x) = u'(t, x) - \frac{\Delta t}{\rho} \cdot \frac{p'(t, x_2) - p'(t, x_1)}{\Delta x} \quad (3.2)$$

where u' is the velocity fluctuation, p' is the pressure fluctuation, ρ is the density of the fluid, Δx is the distance between two points to measure the pressure fluctuation, and Δt is the sampling interval of a microphone. Therefore, the velocity fluctuation between the measuring points is calculated by Equation 3.2 with the measurement of the pressure fluctuation at two points. The test equipment was set according to ISO 10534-2:1998. Dynamic pressure sensors were used to measure the pressure fluctuation and they were installed 675 mm and 690 mm downstream from the orifice, respectively. The phase delay of the dynamic pressure sensors was adjusted equally by the preliminary experiment. In the present study, Δx and Δt were 15 mm and 40 μ s, respectively. Density was examined by measuring the temperature at the time of the experiment.

PIV was used to measure the velocity field near the bluff body. Figure 3.2 shows the schematic of the phase-locked PIV experimental setup. PIV signals were emitted by the

sheet beam produced by the double pulse PIV laser (Nd:YAG laser, 532 nm) and the cylindrical lenses. The time between the two laser sheet beams was set to 10 μ s. Zirconium oxide with a mean diameter of about 1 μ m was used as a seeding particle and it was introduced 845 mm ahead of the bluff body. To fix the total air flow rate, the carrier flow rate for the particle transport and the air flow rate through the orifice were controlled using the MFC. The scattering signals were captured by a CCD camera (ES2020, Princeton Instruments). The laser and camera were both operated at 10 Hz.

Two signals for the operation of the laser and the speaker were generated simultaneously in LabVIEW. Using the oscilloscope, it was confirmed that the phases of the two output signals were almost identical. Each excitation frequency was divided into 12 phases and the average field of each phase was obtained. Thus, two DG 535 delay generators were used for phase-locking. A signal of 10 Hz generated by LabVIEW was transmitted to the first DG 535 delay generator; then, the signal with a delay time, which was considered in order to match the phase of each frequency, was transferred to the second DG 535 delay generator for that signal. The second delay generator adjusted the laser pulse timing and the gate time of the camera. The resolution of the captured image was 2.166×10^{-5} m per pixel and the interrogation spot size was 48×48 pixels.

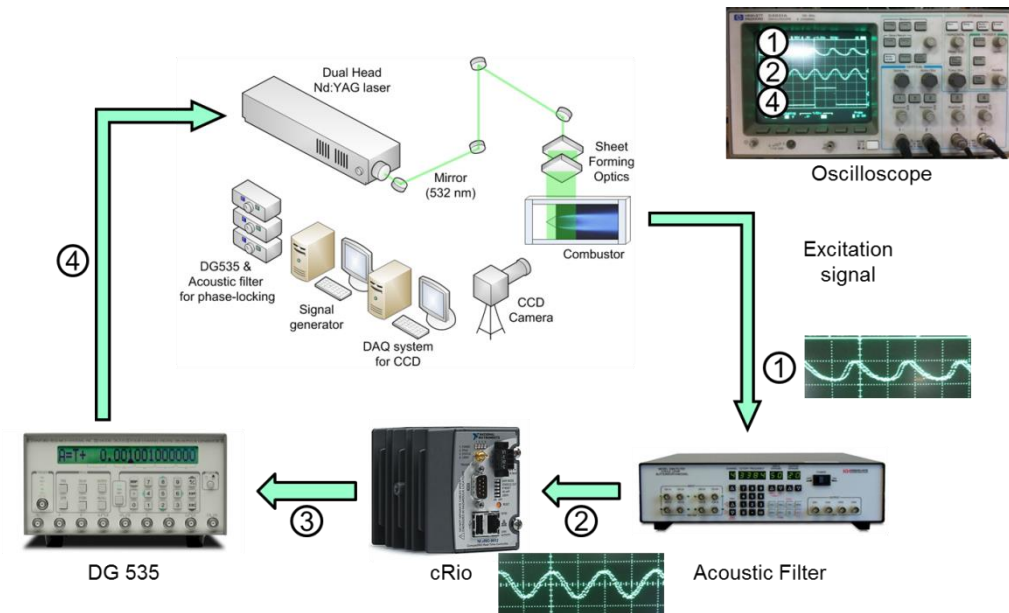


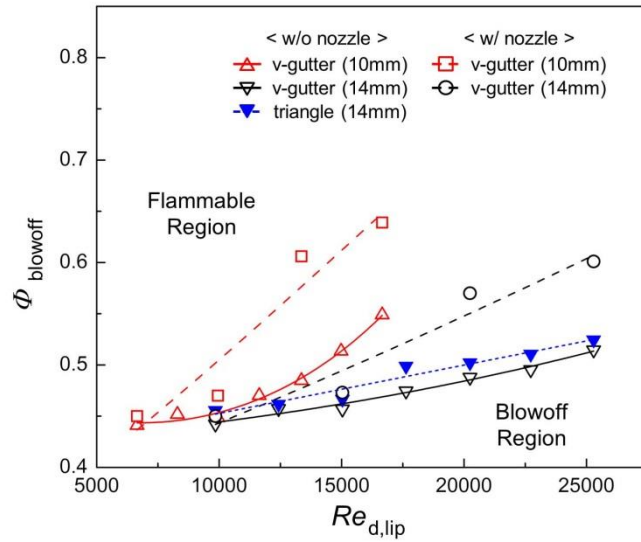
Fig. 3.2 Schematic of the phase-locked PIV experimental setup.

3.3 Characteristics of Lean Blowoff under Stable Flame Conditions

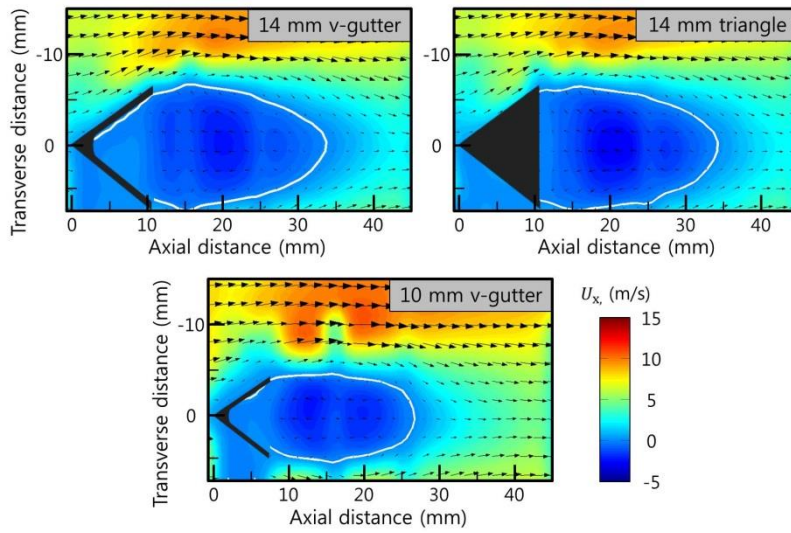
In order to compare the characteristics of the blowoff associated with acoustic excitation, it is important to examine the findings from research on non-forced blowoff. This section discusses the main cause of flame blowoff without acoustic excitation that was investigated in this current study by comparing it with the results from previous studies.

Figure 3.3(a) shows a graph of the blowoff equivalence ratio (Φ_{bo}) for various Reynolds numbers (Re). $Re_{d,tip}$ denoted that the Re was calculated using the flow velocity at the downstream tip of the bluff body (U_{tip}) and the width of the bluff body (L_{bluff}). As reported in other papers [11, 12], the Φ_{bo} increased monotonically to the Re , regardless of the geometric conditions. The value of Φ_{bo} was analogous regardless of the conditions when the Re was small, but the value changed as the Reynolds numbers increased. First,

the blowoff equivalence ratio was greater when the nozzle was placed at the end of the combustor. It is assumed that a change in either the pressure field or the acoustic field induced by the nozzle would result in a dramatic increase in Φ_{bo} . In addition, the blowoff equivalence ratio was reduced in inverse proportion to the size of the bluff body. Furthermore, the Φ_{bo} value of the 14 mm bluff body with a nozzle was smaller than the value of the 10 mm bluff body without a nozzle. The Φ_{bo} value of the v-gutter bluff body was smaller than the value of the triangular bluff body when the bluff bodies were the same size. These results were considered to be due to differences in the size of the recirculation zone, which increased when the size of the bluff body was larger or when it had more internal space. The white solid line in Figure 3.3(b) shows the extent of the recirculation zone of the non-reacting flow and $Re_{d, lip} \sim 15000$ without a nozzle case, shown in Figure 3.3(a). In this paper, the positive direction of the y-axis is defined as the direction toward the bottom of the combustor (see the coordinate system in Figure 3.1). The recirculation zone is defined using line connecting points when the axial velocity is 0 [65]. The 10 mm bluff body has a smaller recirculation zone than the other two cases. The 14 mm bluff bodies are similar in size to the recirculation zone, but the flame stability of the v-gutter bluff body is better than that of the triangular bluff body. Therefore, it was demonstrated that the recirculation zone that develops in the inner space of the bluff body has a significant effect on flame stabilization. Consequentially, the blowoff equivalence ratio is proportional to the flow velocity and the nozzle blockage ratio and inversely proportional to the extent of the recirculation zone.



(a)



(b)

Fig. 3.3. (a) Relationship between Φ_{bo} and $Re_{d,lip}$ for various geometric conditions, (b) The recirculation zone size with various geometric conditions for the bluff body without a nozzle.

Figure 3.4 shows the OH radical chemiluminescence images near the Φ_{bo} with the 10mm v-gutter bluff body and $\dot{m}_a = 15$ g/s. The value (ms) on the left side of each image (t_{bo}) denotes the time to blowoff. As shown in Figure 3.4(a), the flame suffered structural changes near the blowoff. At $t_{bo} = -173$ ms, the strength of the flame was significantly weakened, and this phenomenon was increasingly noticeable over time. Because the unburned gas that was introduced downstream from the bluff body due to the vortex did not burn, the strength of the flame decreased. At $t_{bo} = -167$ ms, a flame hole subsequently occurred when the flame was locally extinguished. A flame hole is a well-known phenomenon that occurs near the blowoff [2]. Until $t_{bo} = -161$ ms, the recirculation zone collapsed, and the flame remained very small. Moreover, OH radical chemiluminescence existed inside the bluff body, thereby demonstrating that the hot products that sustained the combustion phenomenon had disappeared. However, the flame was not completely extinguished and it became stable again afterwards. This phenomenon occurred repeatedly close to the blowoff. Figure 3.4(b) shows the OH radical chemiluminescence images close to the blowoff. Just before the blowoff, the size of the recirculation zone decreased considerably. The unburned mixture was entrained downstream from the bluff body due to the vortex that was generated from the shear layer. This entrainment resulted in the production of a flame hole. Thus, the OH radical only appeared in the vicinity of the bluff body. The smaller flame did not recover and it was affected by the subsequent vortex. At $t_{bo} = -6$ ms, it seemed that the OH radical took on a ‘C’ shape as a result of the subsequent vortex. The flame gradually moved in the bluff body and, eventually, blowoff occurred. This set of processes was first labeled by Zukoski [59] as a residual flame, and it was reported in other literature as previously mentioned in the Introduction section of this current paper. As found in other studies [10, 12], the ignition of the inflowing unburned mixture and the collapse of the recirculation zone play an important role in the structural change of the flame before blowoff.

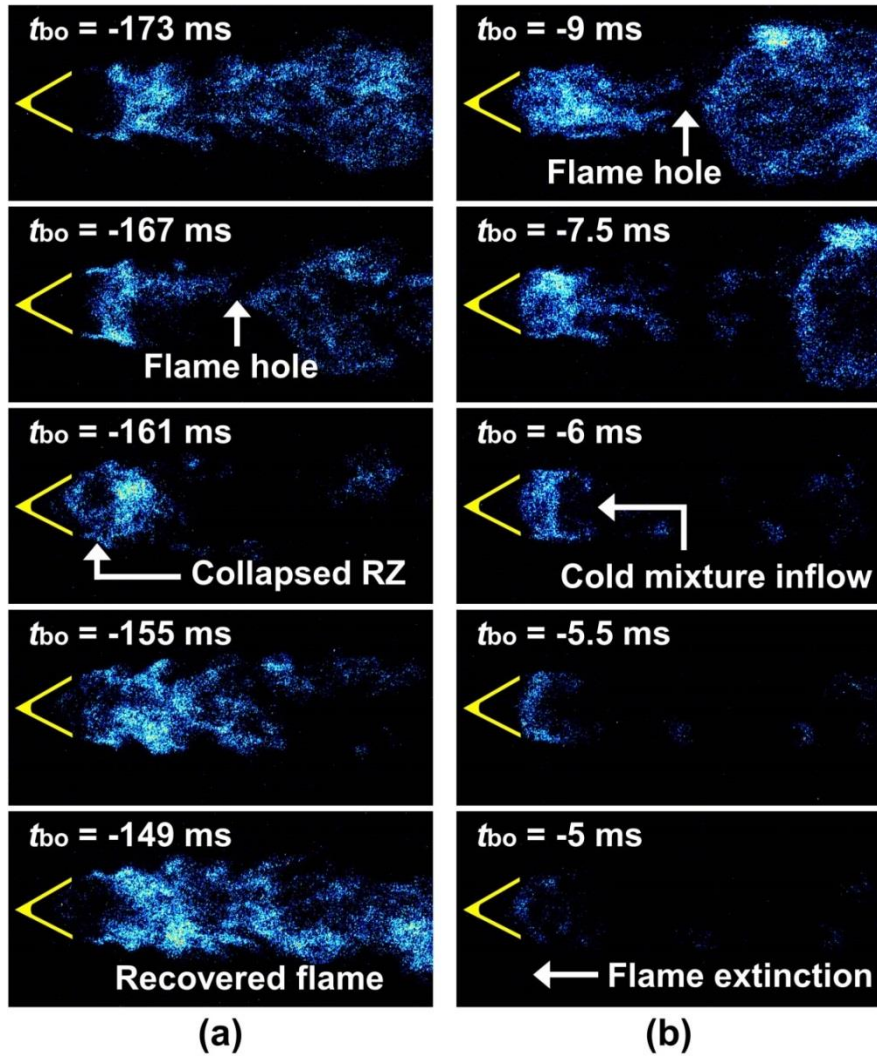


Fig. 3.4. Images of OH radical chemiluminescence without excitation with a 14 mm v-gutter bluff body at $U_{ip} = 16.1$ m/s and $\Phi_{bo} = 0.457$; (a) near blowoff, (b) close to blowoff.

The application of a dimensionless number enables one to analyze the main cause of a phenomenon. Many researchers have used a variety of parameters for scaling the blowoff phenomenon. The common conclusion obtained from their studies is that the

Damköhler number (Da) is a dimensionless number that is useful to represent the blowoff characteristics [66]. Therefore, in this present study the main parameter affecting the blowoff was investigated using Damköhler number. To express the effect that the geometry of the bluff body has on the blowoff phenomena in greater detail, Da_{blowoff} was defined as $Da_{\text{blowoff}} = (L_{\text{RZ,cold}}/U_{\text{lip}})/(\alpha_f/S_{\text{L,bo}}^2)$ because U_{lip} and $S_{\text{L,bo}}$ are affected by the blockage ratio and Φ_{bo} , respectively. Here, $L_{\text{RZ,cold}}$ is the axial length of the recirculation zone in the non-reacting flow and it is a suitable parameter to represent the flow length scale [67]. In addition, α_f is the thermal diffusivity of the fuel and $S_{\text{L,bo}}$ is the laminar flame velocity at the blowoff equivalence ratio. $Re_{\text{D,tip}}$ was calculated using the flow velocity at the downstream tip of the bluff body and the hydraulic diameter of the combustor (D) in order to consider the effect of turbulent. The results of the present study (two-dimensional case) and other studies (axisymmetric case) that used CH_4 as fuel are presented in Figure 3.5. Information on $L_{\text{RZ,cold}}$ of other studies was obtained from another paper describing an experiment conducted with an identical apparatus [68]. As shown in the graph, Da_{blowoff} increased along with $Re_{\text{D,tip}}$ because the blowoff could easily occur at a higher flow velocity. The calculated value of Da_{blowoff} in confined axisymmetric (red ring in Figure 3.5) and unconfined axisymmetric cases (red filled circle and green star in Figure 3.5) is distributed in the graphs when only the recirculation zone behind the bluff body is considered as the characteristic length. It was necessary to introduce new conditions in order to complement the differences due to the geometric features of the combustor. The confined axisymmetric case has the advantage of flame stability under the same conditions; this is because the outer recirculation zone that exists between the flame and the wall in the dump combustor exerts an influence. Therefore, the Da_{blowoff} in the confined axisymmetric case was calculated using the recirculation zone length that contains the length of the outer recirculation zone. Consequently, this approach effectively works to collect data regardless of the confined geometry, as shown in Figure 3.5. Moreover, the results of the present study and the other cases overlapped, although the combustor types were different. Based on the definition of Da_{blowoff} and $Re_{\text{D,tip}}$, the

relationship between U_{lip} and $S_{L,bo}$ is the most influential parameter for determining these slopes. Meanwhile, $Da_{blowoff}$ becomes independent of $Re_{D,lip}$ when the latter is increased above $Re_{D,lip} \sim 10^5$. The relationship of ' $S_{L,bo}^2/U_{lip} \sim \text{constant}$ ' is satisfied by the definition of $Da_{blowoff}$ when the value of $Da_{blowoff}$ is constant. Therefore, it was found that there is a linear proportional relationship between U_{lip} and $S_{L,bo}^2$ under relatively strong turbulent conditions. The results of the preceding analysis suggest that U_{lip} and $S_{L,bo}$ exert a decisive influence on blowoff.

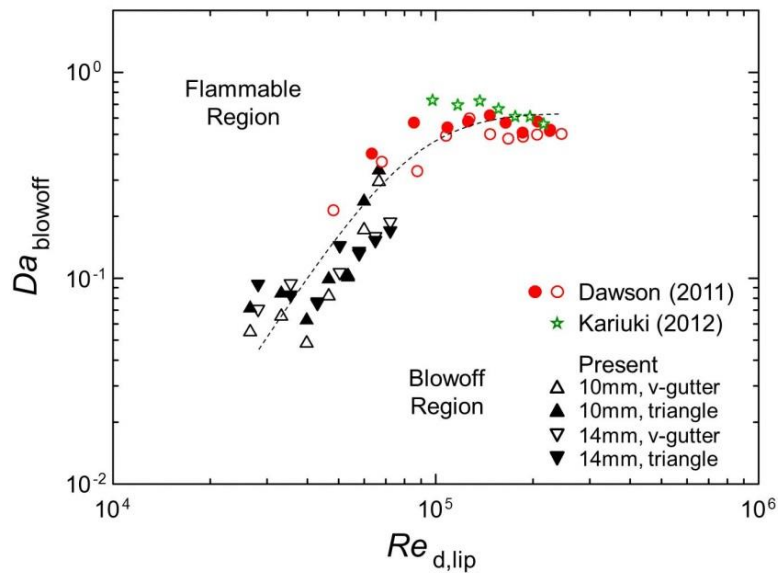


Fig. 3.5 Results of the relationship between $Da_{blowoff}$ and $Re_{D,lip}$ for studies based on methane fuel: two-dimensional and confined case (Δ , \blacktriangle , ∇ and \blacktriangledown), axisymmetric and confined case (\circ), axisymmetric and unconfined case (\bullet and \star).

3.4 Characteristics of Lean Blowoff with Acoustic Excitation

External excitation has a significant impact on the extinction and structural features of the flame. In particular, the acoustic field is one of the dominant factors that influence the characteristics of combustion dynamics. Therefore, this study investigated how external excitation through the speaker impacted the flame blowoff. For simplicity with regards to the acoustic boundary, the experiments were performed with the nozzle removed.

Figure 3.6 compares the stable flame and the acoustically-forced flame of 170 Hz near the Φ_{bo} using OH radical chemiluminescence images. Figure 3.6(a) shows the stable flame structure without acoustic excitation. The stable flame without excitation has a continuous shape and a constant width regardless of the time. However, with excitation (Figure 3.6(b)), the structural changes of the flame appeared to be tuned to the frequency of the excitation. A strong vortex was generated behind the bluff body so that the width of the flame was changed and the flame was locally extinguished. The flame hole found in the blowoff condition of the non-forced flame periodically appeared with a frequency of f_{ex} . The time interval between the two images ($t_{bo} = -2333.5$ ms and $t_{bo} = -2327.5$ ms) showed that the generation cycle of the flame hole was about 170 Hz. The observed changes were also seen for the flame far from the blowoff, and they lasted until the moment just before the blowoff. Figure 3.6(c) shows the sequence of the blowoff in the forced flame. Although the chemiluminescence intensity was relatively weak due to the decrease in the equivalence ratio, the change of the flame structure described above continued to occur immediately before the blowoff. The occurrence of blowoff depended on the recovery of the recirculation zone, which had been collapsed due to the strong vortex downstream from the bluff body. The recirculation zone was immediately restored after its disruption and it was maintained inside the bluff body, as shown in Figure 3.6(b). However, the next vortex disrupted the recirculation zone inside the bluff body and interfered with the recovery of the recirculation zone. Finally, the flame completely disappeared following the complete collapse of the recirculation zone and the continuous

penetration of the cold mixture. The analysis of blowoff with excitation also showed that the most important element in this phenomenon was the presence or absence of the collapse of the recirculation zone and the strength of the vortex downstream from the bluff body. The recovery of the recirculation zone can be achieved when the value of the burning velocity (U_b) is greater than the value of the velocity of the inflowing cold mixture behind the bluff body (U_{mix}). However, the probability of this failing is high because U_b decreases with a low equivalence ratio and U_{mix} increases with a strong vortex. Eventually, the principal elements involved in the stabilization of the flame disappear, and blowoff occurs.

The blowoff process associated with the acoustic excitation was examined and the findings are presented in Figure 3.4 and Figure 3.6. Comparing the two figures, it can be seen that the situations immediately before the flame extinction (recirculation zone collapse, downsizing flames, ignition failure of unburned mixture, and blowoff) are analogous regardless of whether or not excitation occurs. This is because the ultimate reason for blowoff is the imbalance between the mixture flow velocity and the burning rate. The results presented in this current paper correspond with the blowoff concept of a well-stirred reactor [4, 12].

The changes in the frequency and in the intensity of the applied excitation to the combustor affect the blowoff behavior. Figure 3.7(a) shows the variation of Φ_{bo} when the intensity of the external excitation increased. At the time shown in this figure, \dot{m}_a was 15 g/s and f_{ex} was changed from 150 Hz to 400 Hz in increments of 10 Hz. The excitation intensity indicates the value of the sound pressure level obtained at a standard distance of 1 m. In the case of 86.7 dB, it can be seen that Φ_{bo} substantially coincided with Φ_{bo} in a non-forced flame, irrespective of the change in frequency. However, Φ_{bo} monotonically increased with the intensity of the excitation. This tendency was constant, regardless of the excitation frequency. When the excitation became stronger, the strength of the vortex behind the bluff body also increased. As shown in Figure 3.7, Φ_{bo} and I_{ex} have a proportional relationship because the strength of the vortex downstream from the bluff body is one of the main factors that affect blowoff. However, the impact of the excitation

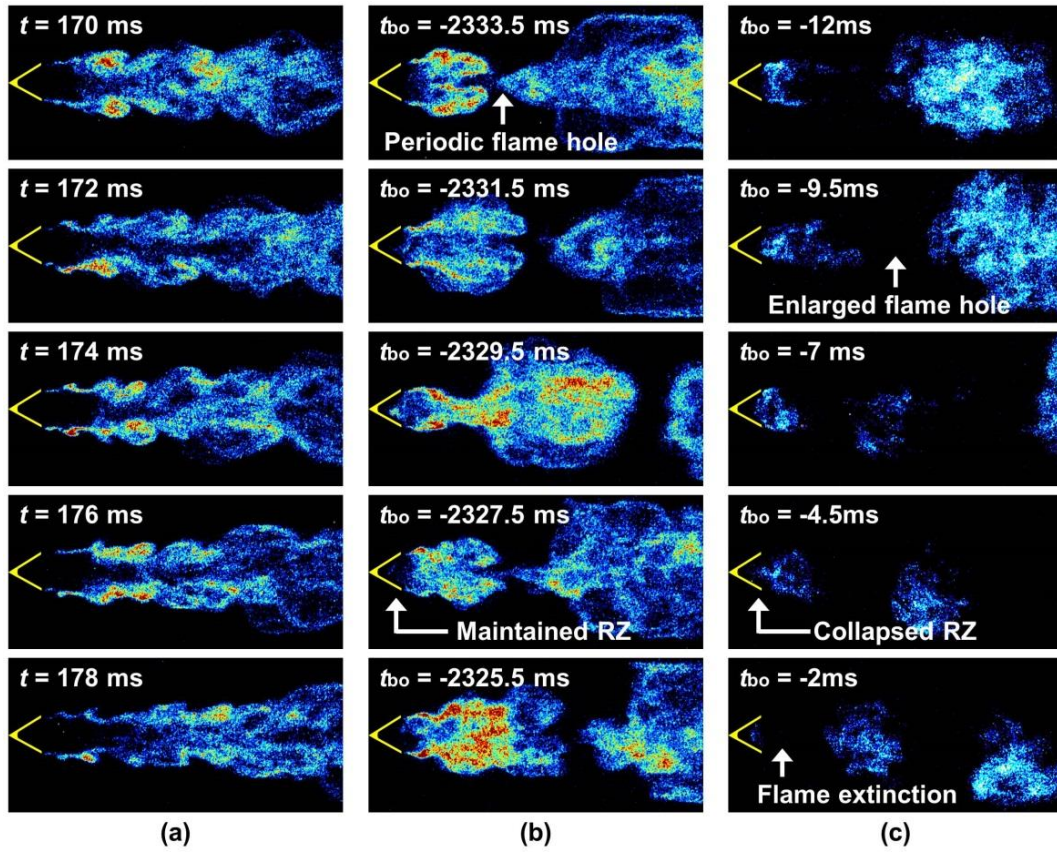
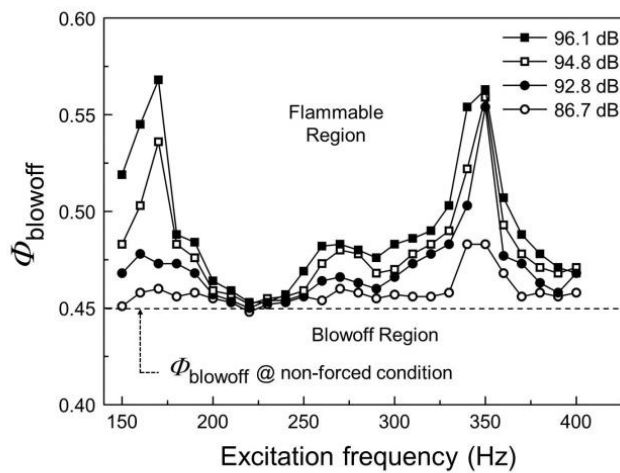


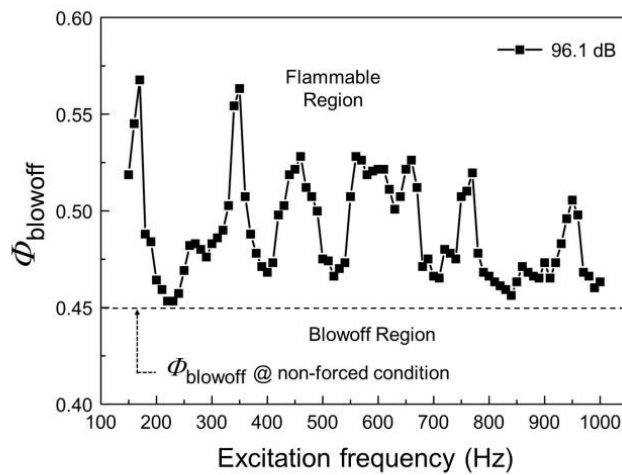
Fig. 3.6 Images of OH radical chemiluminescence with a 10 mm v-gutter bluff body at $\dot{m}_a = 15$ g/s; (a) stable flame without acoustic excitation, (b) far from the blowoff ($f_{ex} = 170$ Hz) with acoustic excitation, (c) close to the blowoff ($f_{ex} = 170$ Hz, $\Phi_{bo} = 0.568$) with acoustic excitation.

intensity on Φ_{bo} was different with respect to the frequency. As shown in Figure 3.7, Φ_{bo} rapidly increased in response to the excitation intensity near 170 Hz and 350 Hz. Moreover, in the case of 97.1 dB or 98.9 dB, it was difficult to maintain the flame; thus, Φ_{bo} could not be measured. On the other hand, the value of Φ_{bo} was similar regardless of the excitation intensity near 225 Hz. To examine the relationship between f_{ex} and Φ_{bo} in more detail, the frequency range was increased to 1000 Hz with a fixed I_{ex} of 96.1 dB.

The results illustrate that several specific frequencies with a high Φ_{bo} exist in the range of 150–1000 Hz, as shown in Figure 3.7(b). This phenomenon is attributed to the strength of the external excitation of a specific frequency being amplified by internal factors, and it is explained in detail in the following paragraph.



(a)



(b)

Fig. 3.7 Variations in the tendency of Φ_{bo} corresponding to the frequency and intensity of excitation in the range of (a) 150-400 Hz and (b) 150-1000 Hz ($\dot{m}_a = 15$ g/s).

As described above, blowoff occurs when the inflow velocity of unburned gas is greater than the burning velocity. This inflow velocity is associated with the vortex generated downstream from the bluff body. Thus, it was hypothesized that the blowoff phenomenon was linked to the vortex downstream from the bluff body. A free shear layer necessarily exists if there is a bluff body in the turbulent flow. This shear layer has a convectively unstable characteristic because it is basically generated by a Kelvin–Helmholtz mechanism and it is readily amplified [2, 69]. When combustion occurs, the strong vortex generated from the shear causes a flow field to wrap up the flame [2]. Although a baroclinic vortex generated by the flame (or density gradient) also exists, the shear-generated vortex plays a dominant role in the near field of the bluff body [70]. Therefore, a proper orthogonal decomposition (POD) algorithm was used to measure the period of the shear-generated vortex of the downstream bluff body. POD analyzes the images to determine the most dominant mode. It can also be employed to obtain the vortex shedding frequency [71]. POD analysis was performed using the 4000 OH* chemiluminescence images, taken at 4000 fps, of the stable flame in $\dot{m}_a = 15$ g/s without excitation. The details of POD analysis are referred to in the literature [72, 73]. Figure 3.8(a) shows the first four modes that were obtained from the POD analysis. The color portions at the top of each image show the results of the POD. The arbitrarily selected chemiluminescence images, right below the POD result, visually represent the flame structure that is described in each POD mode. POD mode (POM) 0 represents the time average image of the bluff body flame. The subsequent modes represent the next dominant form of the bluff body flame. The vortex frequency of each mode is calculated by Fast Fourier Transform (FFT) using the time interval between the image sources and the data obtained in each mode. The vortex frequency of the bluff body was obtained by summing the FFT results of all the modes. The black solid line in Figure 3.8(b) shows the added frequency data from POM 0 to POM 999. In other words, it shows the tendency of the frequency of the shear-generated vortex (f_{sh}) of the stable flame, whereas the black dotted line shows the trend of the Φ_{bo} changes associated with f_{ex} . As shown in that figure, the peak frequencies of the two trends are in very good agreement ($R^2 = 0.88$); thus, there

is a clear correlation between them. It is predicted that the strength of the vortex downstream from the bluff body is increased by the resonance phenomenon when f_{ex} matches f_{sh} . Thus, flame extinction occurred at a greater equivalence ratio at matching point f_{ex} and f_{sh} because the blowoff condition described above was easily created.

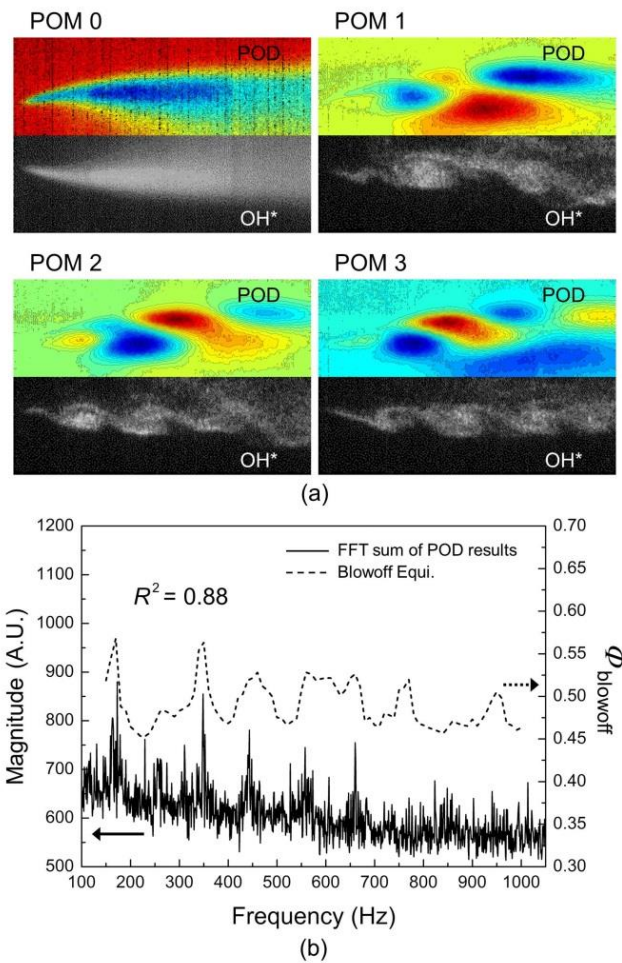


Fig. 3.8 POD analysis; (a) Images of the POD results (upper row) and OH radical chemiluminescence (lower row) at the first four modes of the stable flame with a 10 mm bluff body at $U_{lip} = 14.9$ m/s, (b) Comparison of the frequency trend of the POD analysis and Φ_{bo} .

3.5 Hypothesis of the Blowoff Mechanism

Through the results presented in the previous section, it can be predicted that the resonance phenomenon is an important factor when acoustic excitation affects the flame blowoff. The acoustic resonance is closely connected with the geometry of the combustor. Therefore, to investigate the reason why blowoff occurs at a higher equivalence ratio at a specific frequency the blowoff mechanism hypothesis presented below was suggested:

If the excitation frequency is similar to the harmonic frequency of the combustor, acoustic resonance occurs inside the combustor and increases the amplitude of the inlet flow velocity fluctuation, thereby increasing the flow velocity perpendicular to the convective direction behind the bluff body (or transverse velocity). Accordingly, the maximum value of the transverse velocity ($U_{y,max}$) represents U_{mix} downstream from the bluff body by the vortex. The increased tangential velocity requires a faster burning velocity in order to maintain a stable flame. Eventually, the blowoff occurs at a higher equivalence ratio.

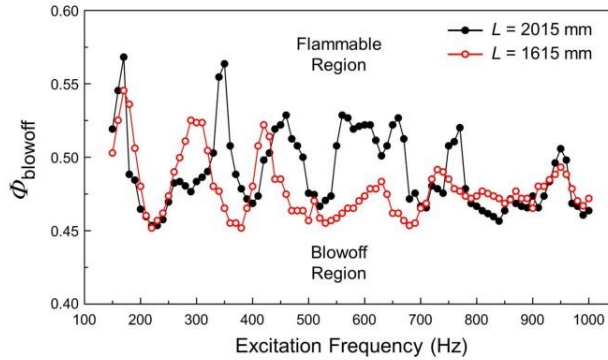
This section discusses the experimental verification that was attempted in an effort to confirm the hypothesis presented above. The observation of the blowoff equivalence ratio along the combustor length, the two-microphone method, and the PIV technique were used as verification methods. The experiments were all conducted in $\dot{m}_a = 15$ g/s and $I_{ex} = 96.1$ dB.

First, the total length of the combustor was changed to confirm the relationship between the acoustic resonance and the trends of the blowoff equivalence ratio depending on the excitation frequency. The change in the length of the combustor alters the fundamental frequencies and the harmonic frequencies. It was expected that the changed fundamental frequency would shift the excitation frequency, resulting in a higher blowoff equivalence ratio. Because the combustor has an open-closed type of acoustic boundary, the fundamental and harmonic frequencies (f_{har}) are calculated using the following equation:

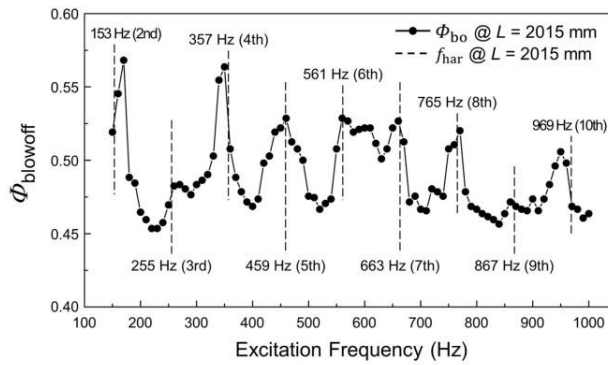
$$f_{\text{har}} = \frac{c(2n - 1)}{4L_{\text{com}}}, \quad n = 1, 2, 3 \dots \quad (3.3)$$

where c is the speed of sound and L_{com} is the total length of the combustor. The fundamental frequency in the reacting flow was about 51 Hz and 58 Hz in the $L_{\text{com}} = 2015$ mm combustor and $L_{\text{com}} = 1615$ mm combustor, respectively. Figure 3.9(a) shows the Φ_{bo} trend of the excitation frequency when the length of the combustor was different. The black and red lines represent the case of $L_{\text{com}} = 2015$ mm and $L_{\text{com}} = 1615$ mm, respectively. The peak frequencies of both cases are slightly different. As previously mentioned, the frequency with the higher blowoff equivalence ratio changed due to the change in the combustor length. Figure 3.9(b) and 3.9(c) shows the trends of the blowoff equivalence ratio and the harmonic frequencies along the combustor length. The blowoff equivalence ratio has peak points at harmonic frequencies, and it decreases as the distance from the harmonic frequencies increases. Therefore, it was verified that the Φ_{bo} varies due to the resonance phenomenon caused by the excitation frequency.

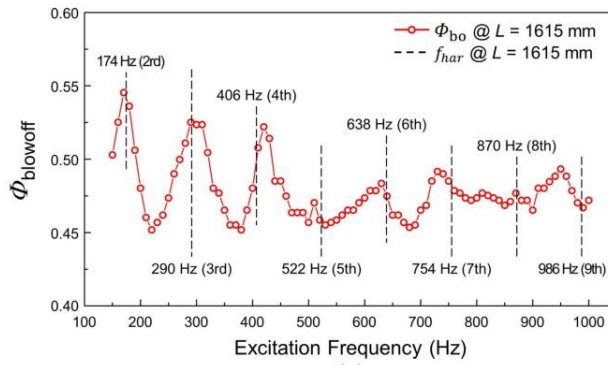
Second, the two-microphone method was applied to demonstrate the relationship between acoustic resonance and velocity fluctuation. Experiments were conducted in a combustor with a length of 1615 mm and an equivalence ratio of 0.6. The reason the equivalence ratio was fixed at 0.6 is because it is possible to maintain a stable flame and obtain the same resonance frequency at that ratio, even in excitation conditions. In Figure 3.10, the black solid line indicates the average value of the velocity fluctuation that was obtained using the TMM. The harmonic frequencies of the combustor are also displayed in Figure 3.10. The velocity fluctuation is greater than zero at all frequencies due to the influence of acoustic excitation. The peak points of the velocity fluctuation appear in the harmonic frequencies. Accordingly, it is confirmed that velocity fluctuation further increased when acoustic resonance occurred in the combustor. In this figure, the trend of the Φ_{bo} is expressed as a black dotted line. The peak points of the velocity fluctuation and the Φ_{bo} are generated at identical excitation frequencies, and the correlation coefficient was calculated as 0.80. Thus, there is a clear correlation between the two trends.



(a)



(b)



(c)

Fig. 3.9 Φ_{bo} trend of the excitation frequency; (a) Comparison of the trends of the blowoff equivalence ratio in two different cases, (b) The trends of blowoff equivalence ratio and harmonic frequencies along the $L_{com} = 2015$ mm combustor, (c) The trends of blowoff equivalence ratio and harmonic frequencies along the $L_{com} = 1615$ mm combustor.

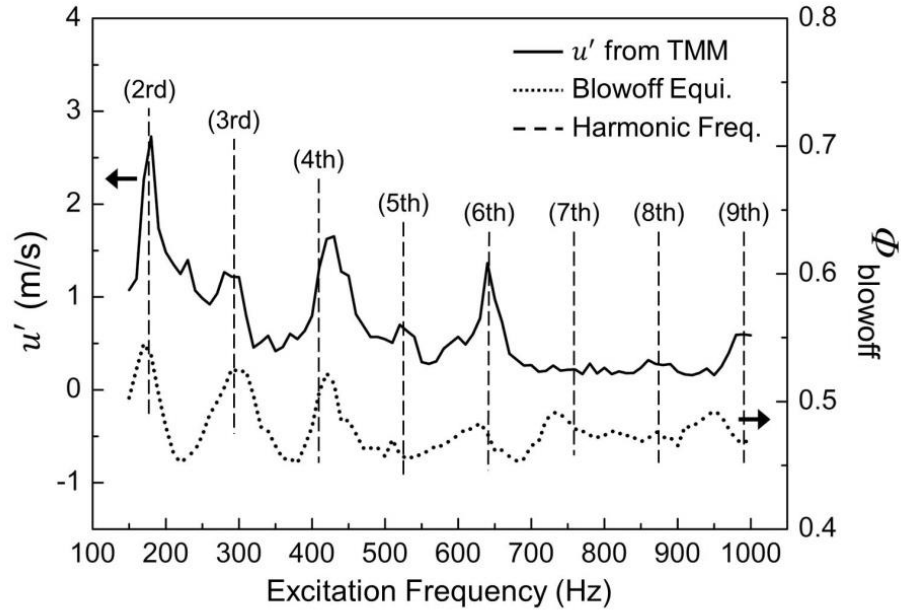


Fig. 3.10 Trends of the velocity fluctuation and the blowoff equivalence ratio with harmonic frequencies of the combustor using the two-microphone method.

Third, the PIV technique was used to examine the change in $U_{y,max}$ due to the excitation frequencies. Because of the limitations of the experimental apparatus, PIV was performed on a combustor with a length of 2150 mm in non-reacting flow. As mentioned above, the sine wave signals that were needed to actuate the acoustic device were divided into 12 phases at intervals of 30° for phase locking. The maximum value of the transverse velocity was acquired through the average field of a total of 110 pairs of images for each phase. Figure 3.11(a) shows the changes in the maximum transverse velocity when $f_{ex} = 190$ Hz. The maximum value of the transverse velocity made one 360° cycle. Figure 3.11(b) shows the images of the average velocity in the y-axis direction at each phase and the overlap with the vectors that were subtracted from half of the center line velocity of the x-axis direction. Because the location of the vortex overlapped with that of $U_{y,max}$ at

each phase, it is possible that the position of $U_{y,max}$ represents the vortex region. The vortex generated at the downstream tip of the bluff body moved downstream in accordance with the phase. In the 150° image, in which $U_{y,max}$ reached close to a maximum value, the position of $U_{y,max}$ is similar to the generation position of the flame hole at the bluff body downstream shown in Figure 3.6(a). Thus, it is considered that the flame hole would be created by a fast transverse velocity.

Figure 3.12(a) shows the velocity fluctuation measured by the two-microphone method in the combustor in which $L_{com} = 2150$ mm. The peak points of the velocity fluctuation appear in the excitation frequencies of 190 Hz and 270 Hz. These points corresponded with the harmonic frequencies of the combustor; thus, the described relationship between velocity fluctuation and acoustic resonance was documented again. Figure 3.12(b) shows the trends of $U_{y,max}$ with the excitation frequencies obtained from the PIV results. Eight cases of frequencies were selected based on the results of the two-microphone method, including two peak and valley conditions of the velocity fluctuation. The average and deviation of $U_{y,max}$ varied with the excitation frequency. The deviation of the period was larger as the average value became higher. This tendency was well aligned in comparison with the tendency shown in Figure 3.12(a) and 3.12(b). This suggests that the stronger velocity fluctuation increases $U_{y,max}$. The flame can sustain a higher burning velocity when $U_{y,max}$ increases, and the burning velocity is proportionate to the equivalence ratio. In the end, the blowoff occurs at a higher equivalence ratio.

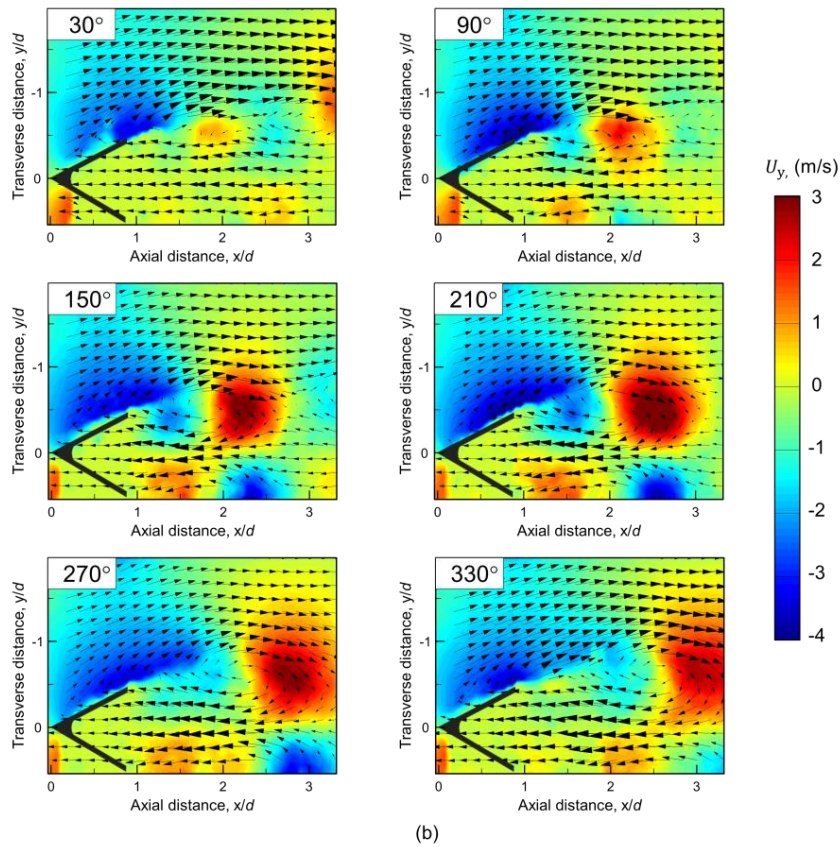
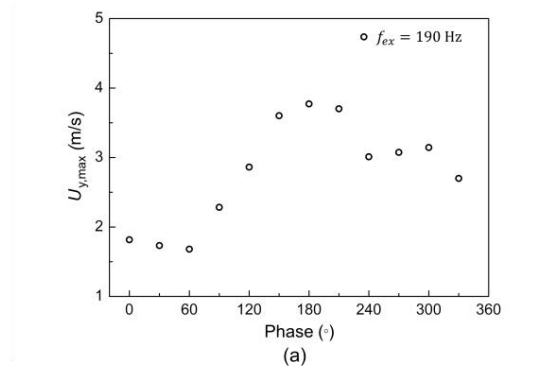
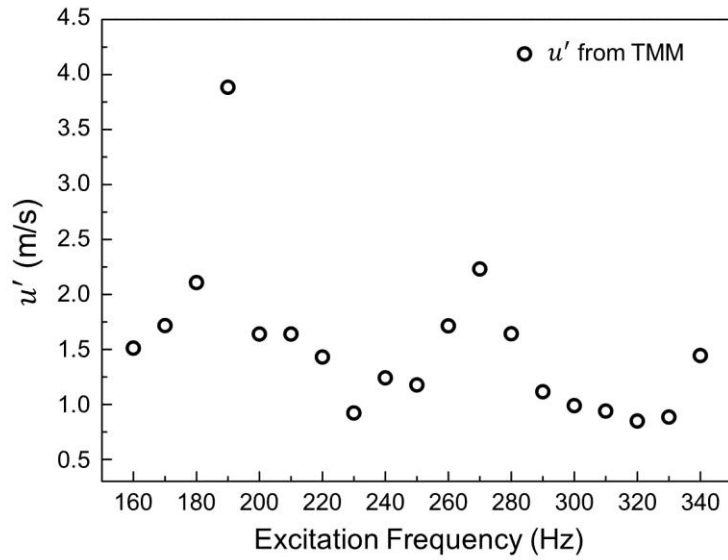
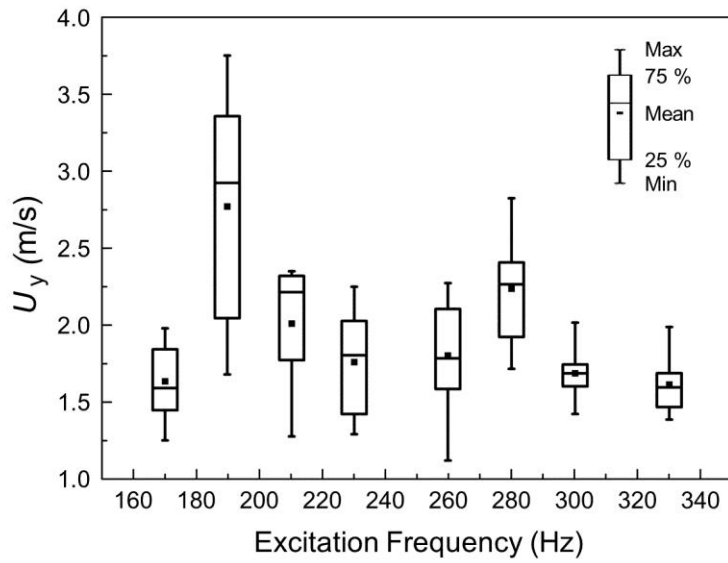


Fig. 3.11 Changes in the maximum transverse velocity; (a) One cycle of the maximum transverse velocity in $f_{ex} = 190$ Hz, (b) Phase-lock velocity field vectors subtracted from half of the center line x-axis velocity, overlapped by the contour image of average y-axis velocity.



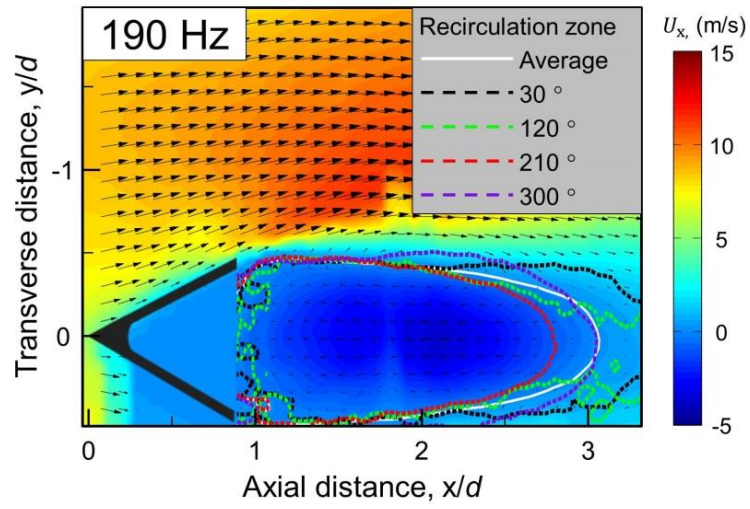
(a)



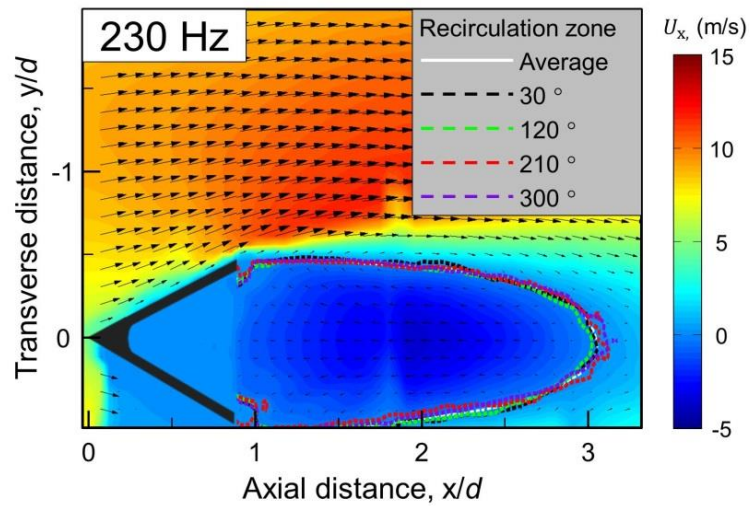
(b)

Fig. 3.12 (a) The velocity fluctuation measured by the two-microphone method ($L_{com} = 2150$ mm), (b) The distribution of the maximum transverse velocity at each phase with the excitation frequencies.

Additionally, the characteristics of the RZ could be used to grasp the formation of the conditions in which blowoff easily occurs with acoustic excitation. It is well-known that the extent and structure of the recirculation zone is closely related to flame stability; this was demonstrated again in recent research [67]. In the stable flame, the structure of the RZ and the flame were both maintained and remained steady. However, in the unstable flame, the extent of the RZ continuously changed with the passage of time. Therefore, the variations in the structure of the RZ mean that the blowoff easily occurred. Figure 3.13 shows the averaged PIV images and the structural changes in the RZ during one cycle of acoustic excitation. The solid line and the dashed line represent the average size and each of the 30°, 120°, 210°, and 300° phases, respectively, in the recirculation zone in the velocity field. The averaged images of PIV in Figure 3.13(a) and 3.13(b) are almost identical regardless of the excitation frequency, and the average size of the RZ is also equal in two of the frequency cases (white line in the figure). However, the change in the size of the RZ in one cycle is significantly different depending on the excitation frequency. In Figure 3.13(a), the size of the RZ was significantly changed because the f_{ex} matched the f_{har} . In contrast, the size of the RZ remained constant irrespective of the phase when f_{ex} was far from the f_{har} . In addition, relatively drastic changes in the size of the RZ near the downstream tip of the bluff body were observed in the case of $f_{ex} \approx f_{har}$. It was difficult for the flame to sustain a consistent shape when the flow fluctuated downstream from the bluff body. In summary, the stability of the flame deteriorated due to the changes in the overall size and shape of the RZ as the excitation frequency approximated the harmonic frequency of the combustor; consequently, this situation will lead to better flame blowoff.



(a)



(b)

Fig. 3.13 The averaged PIV images and the structural changes of the recirculation zone during one cycle of excitation frequency (30° , 120° , 210° , 300° , and average); (a) $f_{\text{ex}} = 190$ Hz (close to the f_{har}), (b) $f_{\text{ex}} = 230$ Hz (far from the f_{har}).

Figure 3.14 shows a simple logic process of the results in this paper. The part acting in common regardless of the excitation was displayed in black, and the part affected by the excitation was displayed in blue. The disruption of the recirculation zone by the decrease of equivalence ratio near the blowoff is a general phenomenon. Thereafter, the factor that decides the recovery and extinction of the flame is the relationship of U_b and U_{mix} as shown Figure 3.14. Also, the flame is extinguished more quickly with excitation. If f_{ex} and f_{sh} have an analogous value, U_{mix} increase due to the enhanced vortex in a shear layer so that blowoff easily occurs.

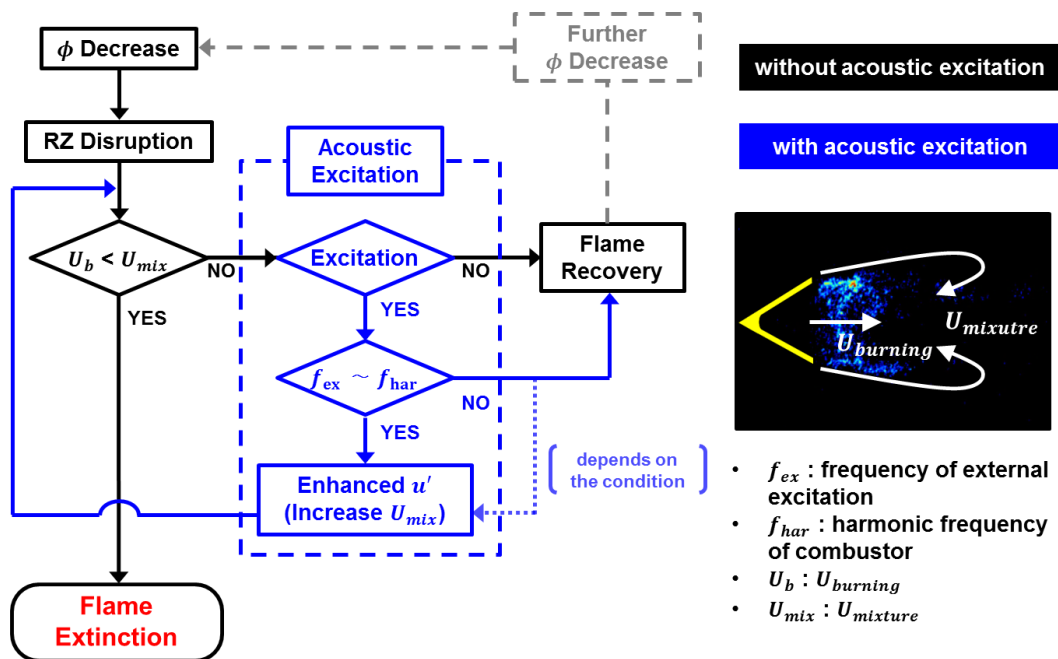


Fig. 3.14 Logic process describing the hypothesis for lean blowoff mechanism with excitation.

CHAPTER 4

FLASHBACK CHARACTERISTICS COUPLED WITH COMBUSTION INSTABILITY IN TURBULENT PREMIXED BLUFF BODY FLAMES

4.1 Background and Objectives

Due to stricter exhaust emission regulations, a lean premixed gas mixture is widely used to reduce exhaust emissions. However, the lean premixed combustor is sensitive to self-excited combustion instability (CI), which can directly degrade its performance and reduce its life cycle. Therefore, numerous studies have been conducted to examine the flame stability and CI of a lean premixed gas mixture [1, 29, 73].

Combustion instability is considered to be one of the causes of flashback [31]. A flashback phenomenon, in which the flame is propagated upstream from the stable region, is one characteristic of the flame in a premixed gas mixture. In general, flashback is the phenomenon that occurs when the local flame speed exceeds the flow speed; this is caused by a variety of factors.

Since the 1980s, experimental studies have examined flashback in the bluff body and the rearward facing step [37, 74, 75]. Keller et al. investigated the mechanism of combustion instabilities leading to flashback with a rearward-facing step, and they used the following terms to describe it: humming, buzzing, and chucking [37]. Subsequently, Thibaut and Candel reproduced the same results as Keller using a numerical method [38]. Dowling reported that the flashback phenomenon induced unsteady inlet flow in the flame-holder using a formula and confirmed that it is similar to the visualization results reported in other papers [39]. Additionally, Fureby [40], Ghoniem et al. [41], Birbaud et al. [42], and Hong et al. [43-45] studied the flashback phenomenon in a backward-facing step and an axisymmetric burner using experimental and numerical analysis.

These studies focused on the flashback phenomenon in which the flame moves back and forth around the trailing edge of the bluff body. However, as the magnitude of CI increases, it is possible for the flame front to propagate to the upstream region of the bluff body; when this happens, the upstream region of the combustor, which is vulnerable to heat, is exposed to the flame. Therefore, the present work examines the characteristics of flashback in relation to CI. In particular, the flashback phenomenon in which the flame propagates to the upstream region of the bluff body was experimentally investigated using the high-speed OH* planar laser induced fluorescence (OH-PLIF) visualization technique and the phase-locked particle imaging velocimetry (PIV) measurement system.

4.2 Experimental Methods

The overall schematic of the combustor is provided in Figure 2.1. The detail of the combustion section and ROI for the visualization techniques are described in Figure 4.1. The mass flow rate of air and fuel at 290 ± 5 K was regulated using a mass flow controller with an overall equivalence ratio (Φ) range of 0.45-1.1. The inlet air velocity (U_{mean}) condition varied from 5.2 m/s to 13.0 m/s by steps of 1.3 m/s. During the experiment, the overall length (from the orifice to the nozzle) of the combustor is approximately 2 m, unless otherwise stated. The v-gutter bluff body is in the shape of an equilateral triangle, the sides of which are 14 mm.

To obtain the combustion frequencies and p' , two static pressure sensors and eight dynamic pressure sensors (PCB-102A05, $P'_{(1)} \sim P'_{(8)}$) were installed in the combustor and were sampled at a rate of 1 Hz and 7 kHz, respectively. The location of the dynamic pressure sensors is listed in Table 4.1. The global heat release rate was acquired using the photomultiplier-tube (PMT) system with WG-305 and UG-11 filters at the rate of 7 kHz.

To excite the OH*, a laser beam at 532 nm was transited to 283 nm using the high-speed OH-PLIF system (IS-200-2-L and Credo-Dye-LG-24). The fluorescence signal was captured using a high-speed camera (High Speed Star 8) with a UV lens ($f = 105$ mm, $f/2.8$) and an OH LIF filter. The laser and camera were both operated at 7 kHz. The

camera trigger signal and the pressure signal were simultaneously recorded to identify the phase of the images.

PIV signals were emitted by the sheet beam produced by a double pulse Nd:YAG laser (Surelite-II, 532 nm) and cylindrical lenses. Zirconium oxide, with a mean diameter of approximately 1 μm , was used as the seeding particle. The scattering signals were captured using a CCD camera (VH-2MC-M42) with a Micro Nikkor lens ($f = 105 \text{ mm}$, $f/2.8$). For phase-locking, the $P'_{(1)}$ signals were filtered using an acoustic filter (Krohn-Hite 3362); they were then used as the trigger signals with two DG-535 digital delay generators.

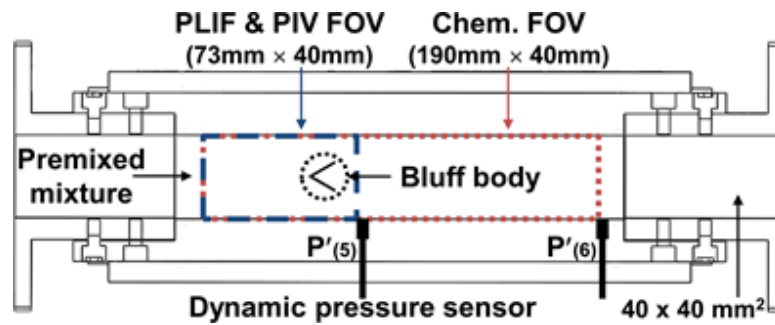


Fig. 4.1 Schematic diagram of the combustor section.

Table 4.1 Location of the combustor parts and the dynamic pressure sensors.

	Location (mm) (downstream from the orifice)
Fuel injector	520
Bluff body	1350
Dynamic pressure sensor ($P'_{(1)} \sim P'_{(8)}$)	300, 560, 640, 720, 1395, 1515, 1655, 1955

4.3 Comparison of One Cycle of the Flashback with Different Conditions

In general, a stabilized bluff body flame is anchored at the trailing edge of the bluff body, and the flame is sustained without a major structural change. Combustion instability leads to structural changes in a flame, and the flashback phenomenon occurs as part of those changes.

Using OH-PLIF images observed from the apparatus used in the present work, Figure 4.2 shows the change in flame structure under different equivalence ratio conditions. The flashback phenomenon shown in Figure 4.2(a) is similar to what has been reported in other papers [37-45]. The flame structures of the 0-180° phases in Figure 4.2(a) are analogous to the 0-90° phases in Figure 4.2(b). In Figure 4.2(a), the flame moves downstream and changes, becoming a stable flame again. In Figure 4.2(b), the flame is propagated continuously upstream from the bluff body, and an interesting flame structure appears at the front of the bluff body. Therefore, in order to distinguish between the two phenomena, a flashback flame that does not arrive at the front of the bluff body is designated as a “weak flashback,” while a flashback flame that is propagated beyond the front of the bluff body is designated as a “strong flashback” in the present work. The combustion instability characteristics that occur during the flashback phenomenon, and the cause of the flame structure change shown in Figure 4.2(b), are explained in detail in the following sections.

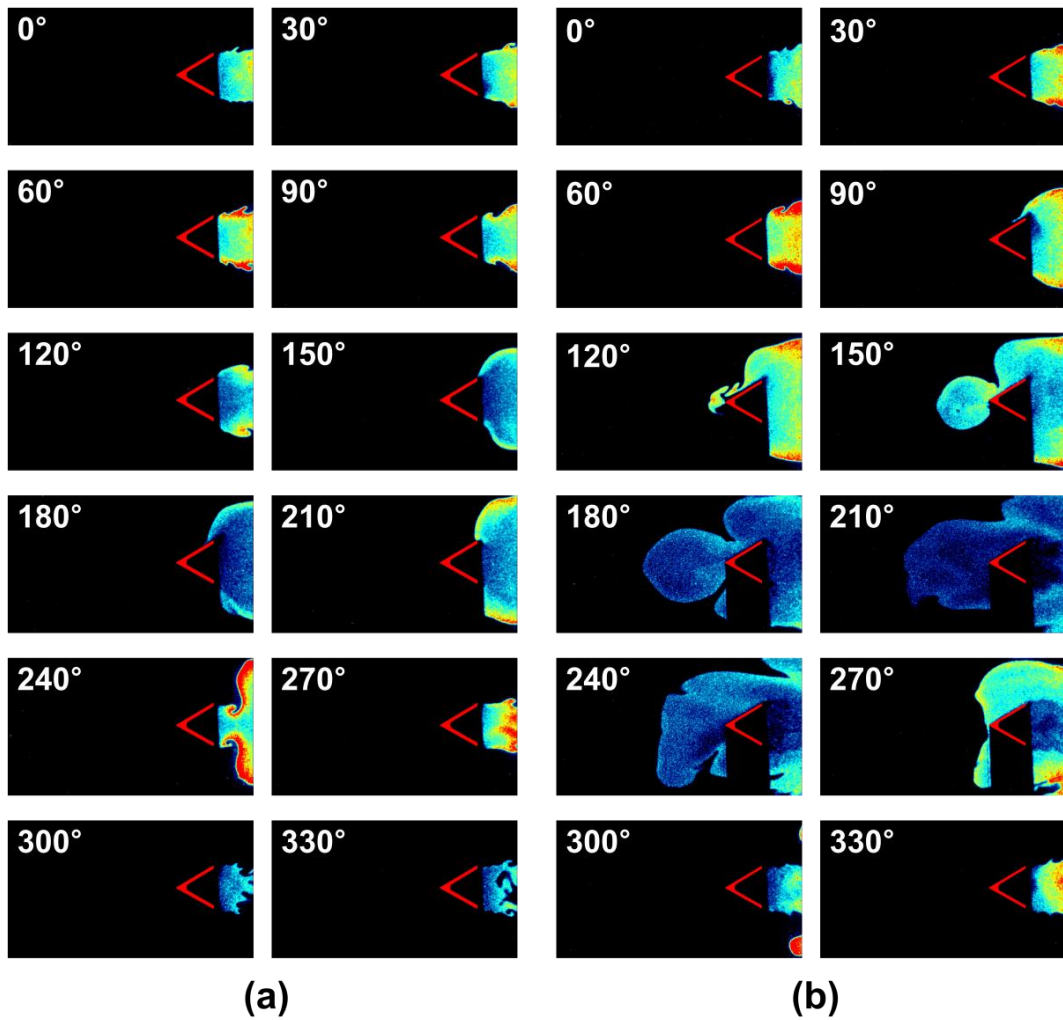


Fig. 4.2 Images of phase-resolved OH-PLIF in the vicinity of the bluff body during one period of (a) weak flashback ($U_{\text{mean}} = 7.8$ m/s, $\Phi = 0.55$); (b) strong flashback ($U_{\text{mean}} = 7.8$ m/s, $\Phi = 0.80$).

4.4 Combustion Instability Characteristics with Flashback

Figure 4.3 shows a graph of the p' amplitude and frequency for various inlet conditions. The circle diameters represent the RMS value of the p' . The symbol in the left upper section of Figure 4.3 is the reference diameter size, indicating the occurrence criterion of the CI [73]. The p' data were measured at $P'_{(1)}$. The frequency of the thermo-acoustic CI is related to the resonance frequency (f_{res}) of the combustor, and the f_{res} varies depending on the temperature distribution and the combustor length. In order to shift the CI frequency (f_{CI}), the length of the cold zone (from the orifice to the bluff body, $L_{coldzone}$) with unburned mixture was changed by moving the position of the orifice and fixing the distance between the fuel injector and the bluff body. Thus, the overall length of the combustor was shortened to 1.7 m, as seen in the condition presented in Figure 4.3(a). The f_{res} of the combustor were calculated using COMSOL Multiphysics software. The cold zone temperature was 290 K and the hot zone temperature (from the bluff body to the nozzle) was the adiabatic temperature of each Φ . The f_{CI} slightly increases with the Φ because of the increase in the hot zone temperature according to the high Φ . Likewise, the magnitude of p' increases with the Φ because a higher Φ causes a larger heat release rate and q' that lead to an increase in p' . As expected, the range of f_{CI} increased when the cold zone was shortened. As shown in Figure 4.3(a) and Figure 4.3(b), the f_{CI} was near 80 Hz and 65 Hz, respectively. The calculated f_{res} exists within the range of the f_{CI} , which means that thermo-acoustic CI occurs in each geometry condition.

The Rayleigh index (RI) is the most common way to determine CI [73]. The q' is obtained using the intensity of the OH radical chemiluminescence, as measured by PMT, near the bluff body, and the p' is measured at $P'_{(5)}$. RI was calculated using a normalized p' and q' . Figure 4.4(a) shows the RI trend over time at $L_{coldzone} = 1.3$ m. The normal distribution of RI that was obtained using the measured data for 5 seconds (about 300 cycles of CI) is presented in Figure 4.4(b). In the weak flashback condition, the RI has relatively low amplitude, and it is evenly distributed in the positive and negative region;

this means that the CI driving and damping are similar. Meanwhile, the RI in the strong flashback condition primarily exists in the positive region, which indicates that CI driving occurs more strongly. When the distribution map is analyzed with the assumption that p' and q' are in the complete sine-wave form, the phase difference of p' and q' is about 90° in the weak flashback condition and 60° in the strong flashback condition. The reduction in the phase difference of p' and q' during strong flashback is consistent with the RI distribution in Figure 4.4(b); this demonstrates that the CI magnitude of the strong flashback case is larger than that of the weak flashback case.

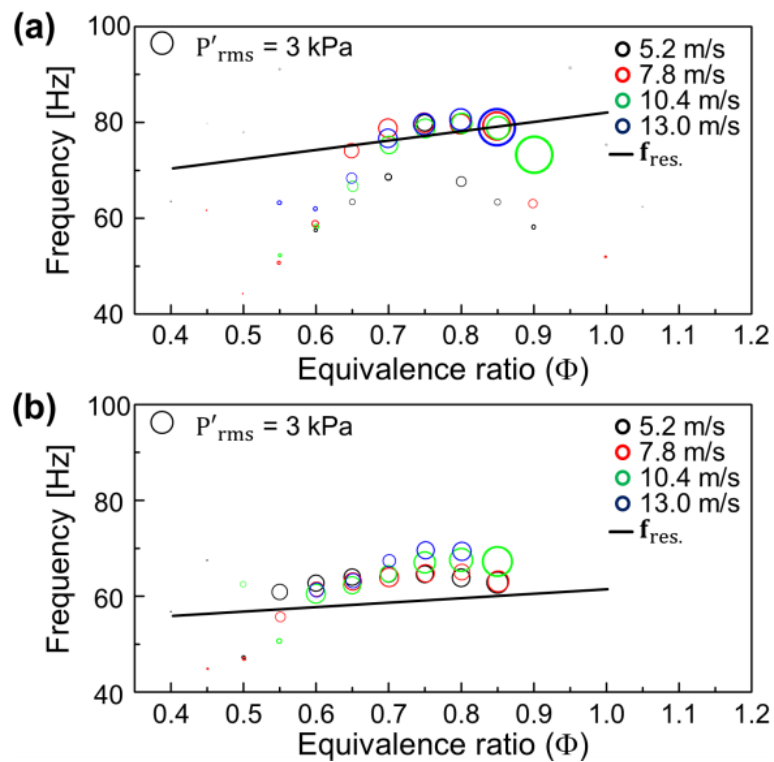


Fig. 4.3. The amplitude of the pressure fluctuation and frequency of the combustion instability for various U_{mean} and Φ ; (a) $L_{coldzone} = 1.0$ m; (b) $L_{coldzone} = 1.3$ m.

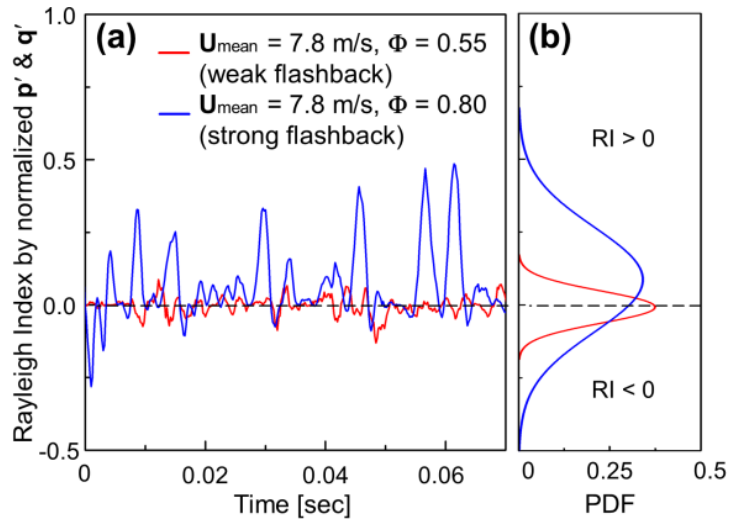


Fig. 4.4. Rayleigh Index of the weak flashback condition and the strong flashback condition; (a) the trend of Rayleigh Index over time; (b) the normal distribution of Rayleigh Index.

4.5 Characteristics of the Strong Flashback Phenomenon

A strong flashback is characterized by the change in the flame structure propagating in front of the bluff body upstream. This section addresses the features and causes of a strong flashback that were investigated using high speed OH-PLIF and phase-locked PIV. The one experimental condition ($U_{\text{mean}} = 7.8 \text{ m/s}$, $\Phi = 0.8$, and $L_{\text{coldzone}} = 1.3 \text{ m}$) was selected because it represents the characteristic of a strong flashback, and it is suitable for visualization.

Figure 4.5 presents a combustor pressure graph for one cycle and its instantaneous OH-PLIF images. To depict the characteristic flame structure of a strong flashback, Figure 4.5(b) shows the phases that occur between the time the flame propagation begins from the trailing edge of the bluff body and the time the flame arrives at the front tip of the bluff body. Figure 4.5(c) shows the phase between the flame propagation, which has an interesting structure at the front of the combustor, and the subsequent downstream

motion of the flame.

In Figure 4.5(a), ‘Front P’ and ‘Back P’ indicate that the combustion pressure was obtained from the summation of the static pressure and dynamic pressure measured at the $P'_{(1)}$ and $P'_{(8)}$ positions. The phases corresponding to the conditions shown in Figure 4.5(b) and Figure 4.5(c) are represented in Figure 4.5(a). The large amplitude p' of the CI causes the phenomenon of a momentary inverse pressure gradient. Consequently, the flame propagates to the upstream region of the bluff body at the 83° phase, as shown in Figure 4.5(b). Notably, the “flame bulge” appears and moves quickly along the side of the bluff body, demonstrating features similar to boundary layer flashback described in the previous studies [76, 77]. This work assumes that the boundary layer flashback occurs due to the slow flow of the bluff body boundary layer in addition to the decrease of quenching distance caused by a heated bluff body. The image of the 110° phase shows how the flame arrives at the front tip of the bluff body, resulting in a relatively strong OH^* signal.

The flame then propagates in all directions like as freely propagating flame, forming a circular flame surface at the front of the bluff body during about the 90° phase, as shown in Figure 4.5(c). This flame structure becomes possible because the pressure in all regions of the combustor is nearly identical, and the pressure gradient based on the position inside the combustor disappears because the pressure in the upper portion of the combustor increased again. This circular flame structure causes an increase in the flashback distance. The flame surface that arrives at the maximum position stagnates during the $10\text{-}20^\circ$ phases. As the pressure gradient inside the combustor is recovered successfully, the flame then moves back again.

Meanwhile, the boundary layer flashback shown in Figure 4.5(b) also appeared in the case of the weak flashback, depending on the conditions (not shown). However, the flame at the front tip of the bluff body did not gain a circular flame shape, as shown in Figure 4.5(c), and the flame moved downstream. As a result, the criterion to distinguish weak and strong flashbacks mentioned in Section 4.3 is the existence of a flame that

propagates freely in the upstream area of the bluff body; the flame structure was determined by the variations of the pressure gradient trends within the combustor.

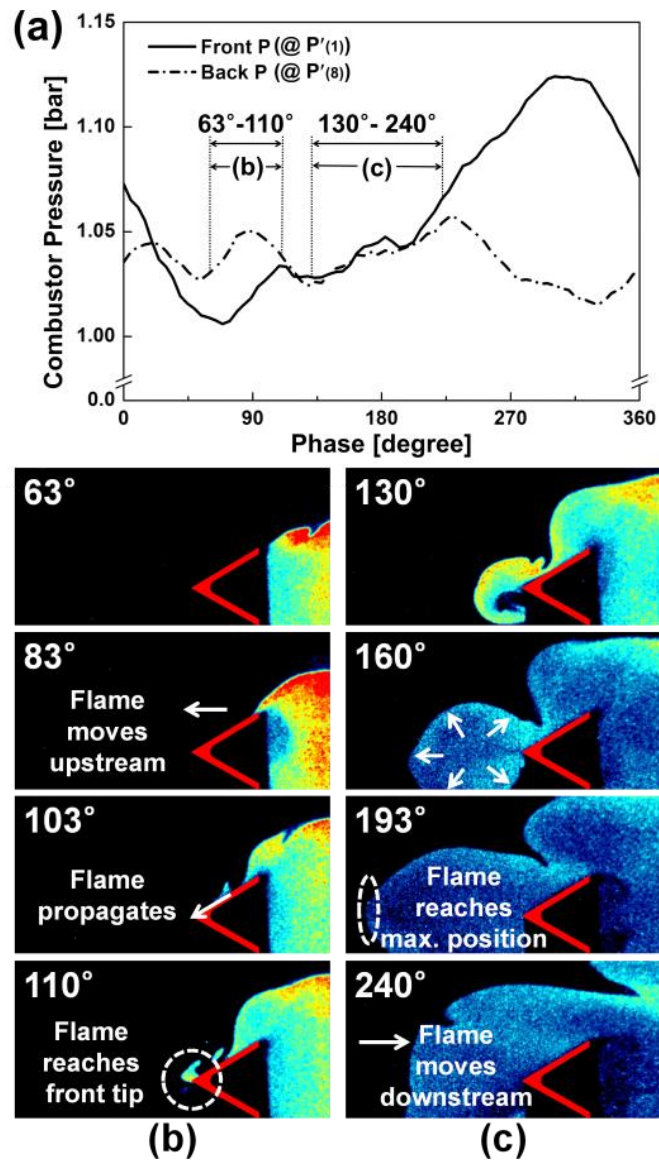


Fig. 4.5. (a) The dynamic pressure graph during one period of a strong flashback ($U_{\text{mean}} = 7.8$ m/s, $\Phi = 0.8$); (b) the instantaneous OH-PLIF images from 63° to 110°; (c) the instantaneous OH-PLIF images from 130° to 240°.

The phase-locked PIV method was conducted at the 110° and 160° phases of CI, which were selected as the moments that represent the signature flame structure of a strong flashback. Figure 4.6 shows a combination of PIV and OH-PLIF images. Figure 4.6(a) shows the PIV image of the 110° phase that is shown in Figure 4.5(b). Based on the flame at the side of the bluff body, the normal direction flow is in front of the flame, and a reverse flow occurs behind the flame. The adverse pressure gradient shown in Figure 4.5(a) generates the reverse flow, and the flashback occurs when the reverse flow pushes the flame behind the bluff body. Moreover, the vortex is generated perpendicular to the flow at the flame front when the flow from upstream collides with the reverse flow. In addition, a reverse flow was also observed in the front side of the bluff body. When a boundary layer flashback occurs, it has been reported that a reverse flow region exists in the upstream of the flame because of the flame-flow and flame-wall interaction [33, 76, 77]. Therefore, a reverse flow on the side of the bluff body can be considered as the result in a boundary layer flashback, not the adverse pressure gradient.

Figure 4.6(b) shows the PIV image of the 160° phase that is shown in Figure 4.5(c). As seen in 4.6(a), a strong reverse flow occurs when the flame front is on the side the bluff body. There is also a strong reverse flow in the upstream area of the bluff body, which is caused by pressure created by the expansion flame near the bluff body front tip. The flow becomes almost stationary at the position where the expanding flame collides with the flame on the side of the bluff body because the pressure created by the expanding flame and the pressure coming from downstream cancel each other out. The flame moving along the side of the bluff body no longer moves forward, as shown in the 160 - 190° phase images presented in Figure 4.5(c).

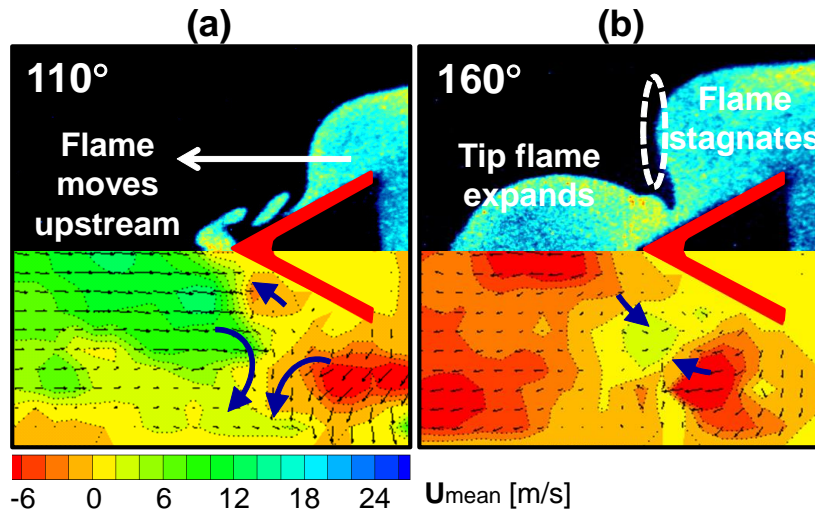


Fig. 4.6. The PIV images (lower half) and the OH-PLIF images (upper half) of a strong flashback condition ($U_{\text{mean}} = 7.8$ m/s, $\Phi = 0.8$) at (a) the 110° phase and (b) the 160° phase.

During the process shown in Figure 4.5(b), the propagation velocity of the flame surfaces (V_f) in the vicinity of the bluff body was measured and compared using OH-PLIF images, which were post-processed to acquire the flame edge [78]. The V_f was calculated using the time interval for each of the images (1/7000 sec) and the moving distance in the normal direction of the flame front, which is similar to the method used to determine laminar flame speed.

As shown in Figure 4.7(a), the $1' \rightarrow 2'$ case represents the condition of the flame that propagates along the side of the bluff body, and the $1 \rightarrow 2$ case represents the condition of the flame that propagates between the bluff body and the combustor upper wall. Figure 4.7(b) shows the V_f trends in the data obtained from a total of 31 cycles. Although the deviation was large, the $1' \rightarrow 2'$ case has a mean velocity of 9.4 m/s while the $1 \rightarrow 2$ case has a mean velocity of 2.9 m/s. Thus, at the same time, it can be observed that the side flame moves about three times faster than the other parts of flames. The velocity of flow behind the flame, as shown in Figure 4.6(a), and the velocity of the $1 \rightarrow 2$ case are of a

similar order of magnitude. However, the velocity of the $1' \rightarrow 2'$ case is faster than the reverse flow velocity on the side of the bluff body, which makes that the interpretation of the cause of the reverse flow, mentioned in Figure 4.6(a), is realistic.

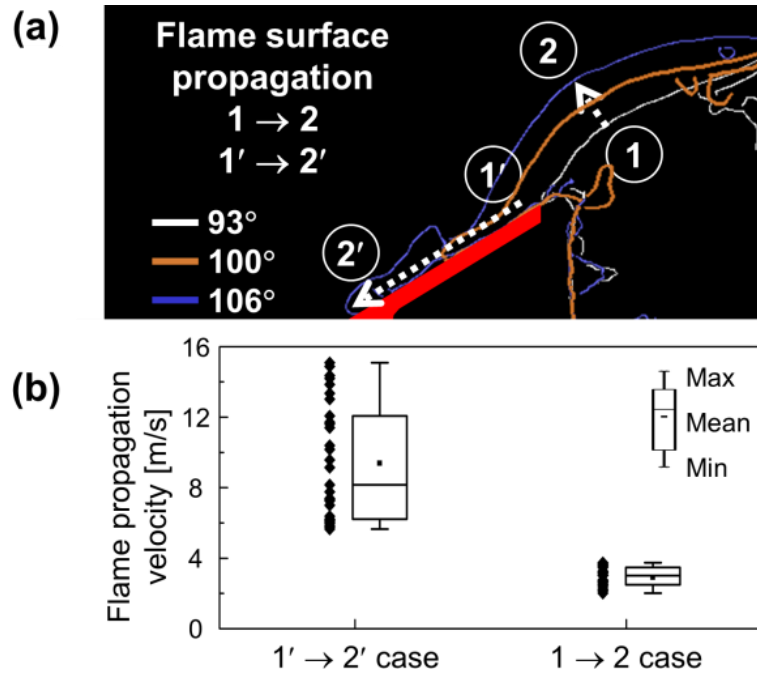


Fig. 4.7 The V_f in the vicinity of the bluff body using OH-PLIF images of the flame edge ($U_{\text{mean}} = 7.8$ m/s and $\Phi = 0.8$); (a) the calculation method of the V_f ; (b) the trends of the V_f at different positions.

4.6 Factors Affecting the Flashback Distance

Flashback is dangerous because the upstream region in the combustor is not strong enough to withstand high temperatures. Since the issue of how far the flame propagates from the anchoring point of the stable flame is important, flashback distance (D_{FB}) was measured in different combustor length (Figure 4.8). The geometry condition of the combustor, shown in Figure 4.8(a) and 4.8(b), is identical to the condition shown in

Figure 4.3(a) and 4.3(b). D_{FB} was defined as the distance between the trailing edge of the bluff body and the farthest position of flame propagation upstream from the bluff body during one cycle of CI. A weak flashback occurs when the D_{FB} is less than the distance between the leading edge and trailing edge of the bluff body. Conversely, a strong flashback occurs when the D_{FB} is larger than the distance between the leading edge and trailing edge of the bluff body.

D_{FB} increased monotonically to the Φ in lean conditions, regardless of the length of the combustor, because the magnitude of the CI is closely related to Φ (Figure 4.3). In addition, the D_{FB} decreased in the same Φ when the U_{mean} increased. As comparison of Figure 4.8(a) and 4.8(b) reveals that the shorten combustor length decreased the D_{FB} . As shown in Figure 4.3, there is no significant difference in the magnitude of the p' when CI occurs despite the change in the combustor length. However, the f_{CI} is one noticeable difference in both cases. The D_{FB} was reduced when the f_{CI} was high. The p' caused by CI changes the velocity field near the bluff body and generates u' . The magnitude of u' corresponds to the magnitude of p' , and it is almost similarly repeated in the limit-cycle. When the phenomena with periodicity moves at the same velocity condition, the distance that can be moved during one period is shortened as the cycles are shortened. The flame propagation distance is only limited to a shorter distance if the period of structural change in the flame is short under an identical u' condition. Therefore, as seen in Figure 4.8(a), the D_{FB} is short in the case of a higher f_{CI} . The results suggest that f_{CI} is one of the decisive factors that have an impact on D_{FB} .

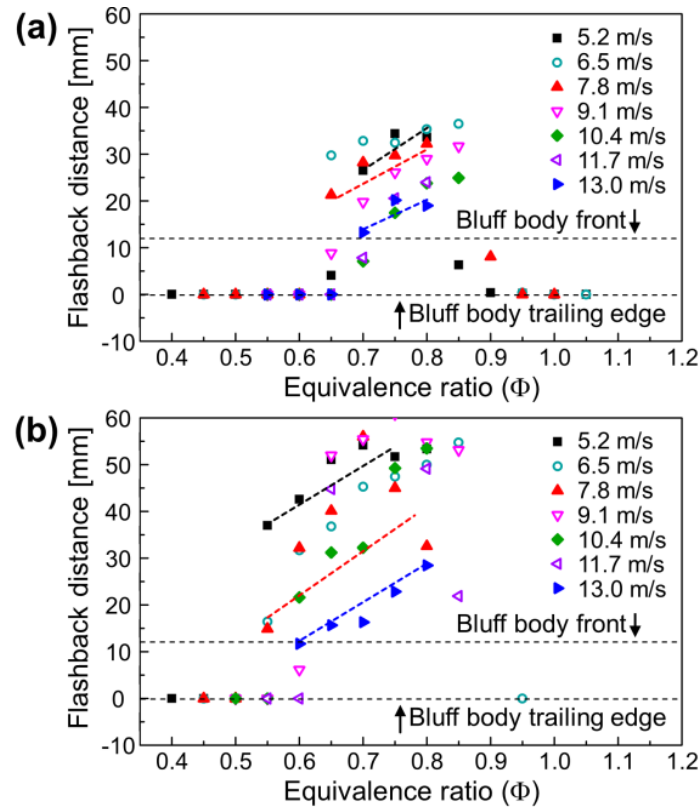


Fig. 4.8. The flashback distance for various U_{mean} and Φ ; (a) $L_{\text{coldzone}} = 1.0$ m; (b) $L_{\text{coldzone}} = 1.3$ m.

As shown in Figure 4.8, it was confirmed that the D_{FB} varied depending on the combustion conditions. An analytical method utilizing nondimensionalization was conducted to ascertain the main causes, since changes in the D_{FB} are generated by a complex interaction of ambient conditions. An increase in the p' increases the possibility of flashback, and it has a positive effect on the D_{FB} . On the other hand, the increase of the U_{mean} prevents an increase in the D_{FB} because the flame should propagate against the inflowing mixture when the flashback occurs. In order to nondimensionalize the relationship between pressure and velocity, it is necessary to transform the pressure parameter to the velocity parameter. Assuming linearized acoustics, u'_{rms} was calculated

from p'_{rms} through $u' \sim p'/\rho c$ [38], where p'_{rms} is acquired at $P'_{(5)}$. The relationship between u' and U_{mean} was represented as turbulence intensity (\mathbf{I}), which was defined as $\mathbf{I} = u'/U_{\text{mean}}$, as a dimensionless number. Therefore, the effect of Φ and the initial flow condition is implicit in the \mathbf{I} . After examining the D_{FB} trends corresponding to the calculated \mathbf{I} , the D_{FB} data, which were scattered in Figure 4.8(b), were gathered in a line. The same conclusion can be drawn from the data presented in Figure 4.8(a), but the slope of the data shown in Figure 4.8(a) is smaller than the slope of the data shown in Figure 4.8(b), and the two cases are distributed in the graphs. To resolve the differences that occurred due to the geometric features of the combustor, it was necessary to introduce a new parameter. As previously mentioned, the f_{CI} that varied depending on the combustor length is likely to hinder an increase in the D_{FB} . Although nondimensionalization was not achieved, an approach that takes into account \mathbf{I} and f_{CI} effectively works to collect data regardless of the combustor length, as shown in Figure 4.9. The results of the preceding analysis suggest that the D_{FB} greatly affected the magnitude of the CI as well as the f_{CI} when the flashback phenomenon occurs due to CI. Furthermore, strong flashback has to be considered in a combustor that has a low f_{CI} .

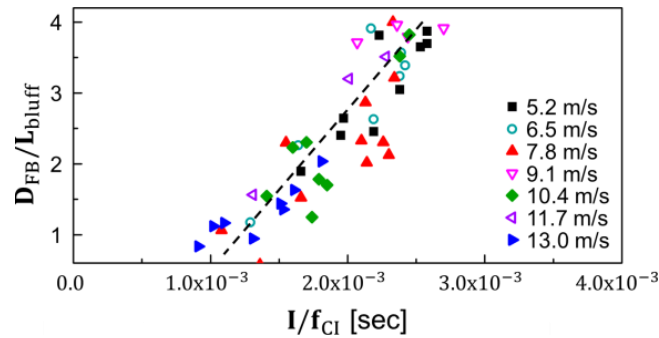


Fig. 4.9. Results of the relationship between D_{FB} and \mathbf{I}/f_{CI} for various flow and geometric conditions.

CHAPTER 5

EFFECT OF HYDROGEN/PERFORATED PLATE/REACTANT TEMPERATURE ON THE FLASHBACK IN BLUFF BODY FLAMES

5.1 Background and Objectives

In a Chapter 4, we had revealed the cause of the flashback phenomenon in a confined combustor with a bluff body and had established the decisive factors that influence the flashback distance. However, as the experiments were conducted only on the methane flame at room temperature, the results obtained from the previous work are limited in terms of versatility. Therefore, it is necessary to confirm the effective application of the decisive factors at various initial conditions.

Of late, the verification of the fuel flexibility is being continuously performed in the field of gas turbine research. In particular, the hydrogen/methane flame has been extensively studied because hydrogen has advantages such as ready accessibility, high lower heating value (LHV) per unit mass; carbon oxides such as CO and CO₂ are also not formed [32, 79-82]. Figura demonstrated that similar flame structures have similar flame heat release centers regardless of the operating conditions and heat release center of the flame has a single path related to the flame stability. Therefore, he suggested that the flame structure has a potential to predict the combustion instability under various experimental conditions [79]. Yoon investigated the combustion instability characteristics with a partially premixed H₂/CH₄/CO flame and demonstrated that the combustion instability mainly occurred in a H₂/CH₄ flame condition [81]. Although hydrogen has several advantages as a fuel, hydrogen fuel needs attention while handling, as a flashback is likely to occur easily due to a rapid reaction rate.

A perforated plate can modify the characteristics of the flow field or flame structure

with comparative ease. Based on the method of usage, the perforated plate increases the homogeneity of the flow field and prevents the generation of cavitation [83]. The relationship between the perforated plate and the flame has been consistently studied because the perforated plate is practically used to stabilize the flame in industrial and household burners [84-87]. The influence of the perforated plate on the flow field changes according to the hole arrangement, number of holes, hole size, blockage ratio (BR), thickness of the plate, etc. These geometric variations change the acoustic reflection coefficient of the perforated plate, affecting the flame structure and characteristics accordingly, when installed in a combustor.

Meanwhile, the temperature of the inlet mixture of the actual combustor is higher than the room temperature in most cases because the mixture undergoes a compression process. When the mixture temperature rises, the chemical reaction rate of the mixture increases and the acoustic characteristics in the combustor change. In addition, the increase in the unburned gas affects the flame dynamics. Until recently, several researches have been actively conducted on the characteristics of the flame owing to the temperature ratio of the reactant and the products. Erickson explained the reasons for the shift in the fluid dynamics to a coherent asymmetric behavior [88]. When the reactant temperature increases, the temperature ratio across the flame reduces both by the $1/T_u$ effect and the absolute reduction of $T_b - T_u$. The flame moves away from the wake region due to the increase in the flame speed; hence, the impact of combustion on the wake is reduced. Emerson demonstrates that the bluff body wake structure is closely related to the density ratio and the baroclinic vorticity [89]. The increase in the density ratio causes the transition of the dominant flow instability from a convective instability to an absolute instability but this transition does not occur abruptly and intermittency exists. Manoharan elucidates that the major mechanism for an absolute/convective instability transition is closely related to the vorticity fluctuations generated by the competition between the flow vorticity gradient and the flow density gradient [90]. In addition, the effect of a harmonically acoustic excitation was investigated under conditions, where the density ratio was varied [91].

Therefore, in this study, we confirm the applicability of the decisive factors affecting the flashback distance, derived from the previous work, under various conditions. The ratio of hydrogen in the fuel, the reactant temperature, and the blockage ratio of the perforated plate are set as the variables.

5.2 Experimental Methods

5.2.1. Experimental Apparatus

The overall schematic of the combustor is provided in Figure 2.1. The bluff body is of a v-gutter type and an equilateral triangle with a side length of 14 mm. The pressure fluctuation and flow temperature were measured using six dynamic pressure sensors and three K-type thermocouple, respectively.

As mentioned in the introduction, the experimental apparatus was additionally configured to consider various variables, as shown in Figure 5.1. An MFC for hydrogen was installed to regulate the mass flow rate of hydrogen, and a shut-off and check valve were installed in the downstream of the MFC for safety. A static mixer was installed in the upstream of the fuel injector for the uniform mixing of hydrogen and methane. Perforated plates with different blockage ratios were designed and placed between the fuel injector and bluff body, as indicated by the arrows in Figure 5.1. The perforated plate was installed at a position, where it is closest to the bluff body and not affected by the flashback flames. In addition, an electric air heater was placed between the air MFC and the upper orifice to control the temperature of the reactant. The heater operates on the principle that air is heated, while passing the layered structure of the ceramic plate heated by electricity. The temperature of the heater is controlled by a proportional–integral–derivative (PID) controller.

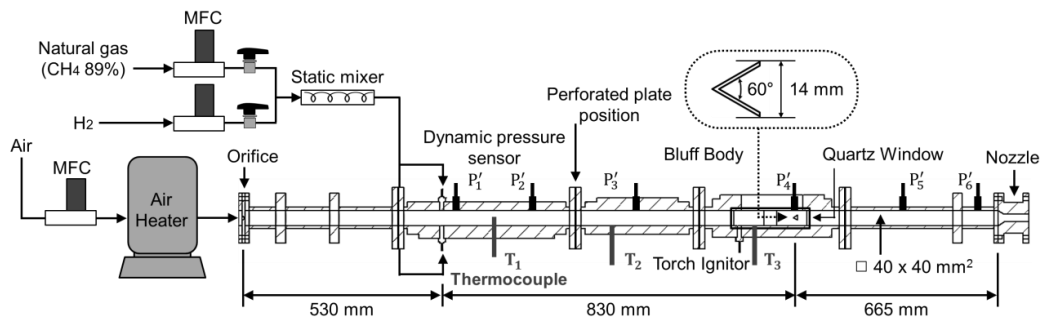


Fig. 5.1. Schematic of the combustor with an electric air heater, hydrogen feeding device, and the perforated plate position.

5.2.2. Experimental Conditions

The air mass flow rate was varied from 10–30 g/s, in steps of 2.5 g/s for all the experimental conditions. For the hydrogen/methane flame condition, the experiment was conducted by increasing the volume ratio of hydrogen from 12.5–75% in steps of 12.5%. At each volume ratio, the fuel mass flow rate was regulated based on the equivalence ratio.

The blockage ratio of the perforated plate, i.e., the ratio of the plate’s frontal area over the combustor cross-sectional area, varied from 0.2–0.7. A square hole shape was adopted for a large variation of the blockage ratio. Nine holes were arranged in the form of a 3 x 3 matrix on the perforated plate. The size of the holes was adjusted by changing the side length, while fixing the distance from the center point of the hole in the center, to the center point of each hole. Figure 5.2 depicts perforated plates with blockage ratios of 0.4, 0.6, and 0.8. The turbulence characteristic in a non-reacting flow with the perforated plate was measured using a hot wire anemometer.

In the case of the reactant temperature, the temperatures of air and the fuel mixture were varied from 373–623 K in steps of 50 K at the bluff body position. To avoid thermal fatigue of the thermocouple owing to the flame, the temperature was set based on thermocouple 1, as shown Figure 1, in the actual experiments. Therefore, the experiment was conducted by setting a value 10% higher than the desired temperature condition to

consider the effect of the temperature decrease due to heat transfer, when the reactant moves from the location of thermocouple 1 to the bluff body. The temperature of air from the heater outlet dropped sharply, when the mixture passed through the combustor due to heat transfer between the combustor and the surrounding atmosphere. As the amount of heat is proportional to the temperature difference, the flow temperature in the combustor was not stable, initially. Therefore, the experiment was conducted, when the heat transfer between the combustor and the surrounding atmosphere reached a quasi-steady state and the temperature drop accompanying the movement of the fluid was almost constant.

At the fixed conditions of the mass flow rate and cross-sectional area of combustor, the flow velocity increased with the temperature. The mass flow rate decreased depending on the flow temperature for minimizing the effect of the velocity because velocity is one of the decisive factors for the formation of the flashback condition. Here, the flow rate was determined based on the condition of the 15 g/s and 20 g/s at room temperature. In addition, the case of a fixed mass flow rate at 15 g/s was considered to compare the case of the fixed flow velocities. All the test conditions are summarized in Table 5.1.

The images of the OH radical chemiluminescence of the flame were obtained for observation and comparison of the flame structure with respect to the initial condition, using a high-speed camera (High Speed Star 8) with a UV lens ($f = 105$ mm, $f/2.8$) and an OH light interference (LIF) filter. The camera had a resolution of 1024×1024 pixels and the frame rate was set to 7000 fps.

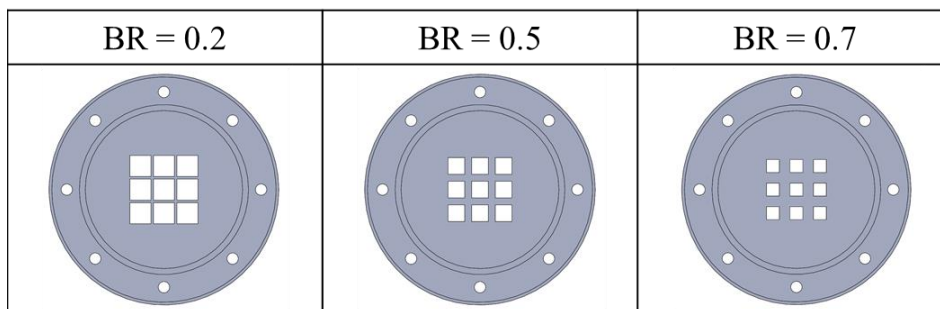


Fig. 5.2 Design of the perforated plate with various blockage ratios.

Table 5.1 Experimental conditions with each case.

	Condition		
	H ₂ /CH ₄ flame	Perforated plate	Reactant temperature
Hydrogen ratio	12.5% – 75% (at intervals of 12.5%)	0%	0%
Blockage Ratio	0	0.2 – 0.7 (at intervals of 0.1)	0
Temperature	≅ 290 K (Room Temperature)	≅ 290 K (Room Temperature)	373 K – 623 K (at intervals of 50 K)

5.3 Effect of Hydrogen/Methane Fuel on the Flashback

Figure 5.3 depicts the laminar flame speed of hydrogen/methane flame depending on the amount of hydrogen added to the fuel. The flame speed was calculated using the GRI 3.0 mechanism. For a higher proportion of hydrogen in the fuel, as expected, the flame speed increases. The values of the laminar flame speed are similar to the values of the pure methane condition, when the proportion of hydrogen is 25% or less; the rate of increase of the flame speed rises significantly with the hydrogen proportion. The increase in the laminar flame speed due to the addition of hydrogen has a duality with respect to the flame stabilization; although a fast flame speed makes it possible to maintain a stable flame under a high-speed flow condition, it also has a disadvantage in that the flame is vulnerable to flashback.

Figure 5.4 presents a graph of the relationship amongst the flashback distance, the measured pressure fluctuation, and the combustion instability frequency in the hydrogen/methane flame conditions. The definition of the flashback distance and the x-axis parameter was applied directly to the method used in the Chapter 4.6. It can be seen that the location, where the data concentrates, differs depending on the hydrogen mixing ratio. Data is evenly distributed when the proportion of hydrogen is 12.5 %. Data at hydrogen ratios of 25 % and 37.5 % are concentrated near flashback distances of 70 mm

and 90 mm, respectively. These trends indicate that the range of conditions, where the flame periodically moves close to the bluff body under a high pressure fluctuation condition, is wide and the flame is not easily extinguished. Because the flashback distance in the 37.5% hydrogen case is longer than 12.5 and 25 % cases, the flame speed can be considered as the parameter that influences the increase of the flashback distance. However, in the 50% and 62.5% hydrogen cases, the data is again evenly distributed because it is in the section, where the flashback distance is less. In addition, there is relatively more data at the point, where the flashback distance is zero. Although the flame speed is faster than the lower-hydrogen-proportion case, the flashback distance did not noticeably increase. Most data are distributed near the zero-flashback distance, when the hydrogen proportion is 75%. This tendency does not imply that the increase in the flame speed does not affect the increase in the flashback distance but that the flame completely leaves the bluff body under several conditions. The flashback flame moved upstream in the combustor beyond the visualization area and was not anchored in bluff body under conditions where the magnitude of the pressure fluctuation was lower than the general value at which combustion instability occurs. Therefore, the flashback distance cannot be measured. Although there are slight differences depending on the flow rate, the range of conditions for periodic combustion instability were the widest, when the proportion of hydrogen was 37.5% and 50%, and it significantly decreased at 62.5% and higher. In conclusion, a certain amount of hydrogen maintains the flame close to the bluff body, even under high pressure fluctuation conditions. However, because the flame easily proceeds upstream in the combustor, even with relatively small pressure perturbations, when the proportion of hydrogen in the fuel increases, the use of hydrogen as a fuel in the premixing conditions is to be considered carefully.

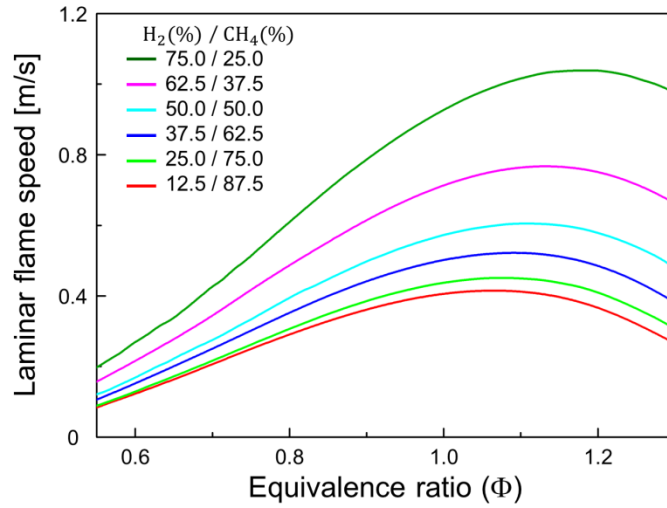


Fig. 5.3 S_L of the hydrogen/methane flame with respect to the amount of hydrogen added (calculated using the GRI 3.0 mechanism).

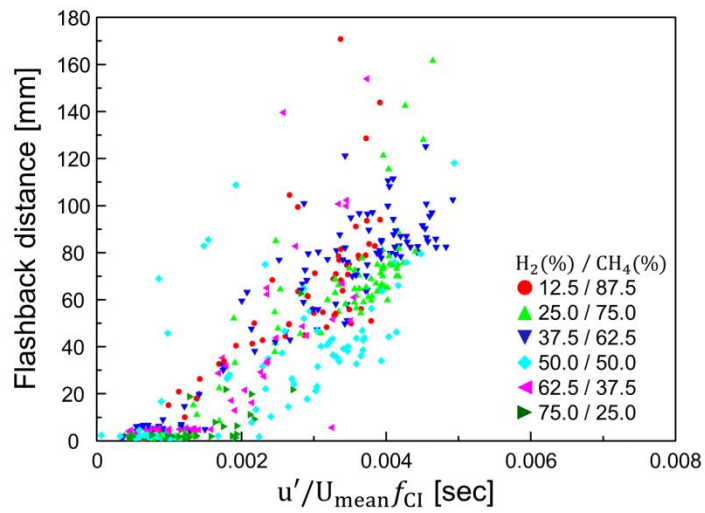


Fig. 5.4 Relationship amongst the D_{FB} , the measured pressure fluctuation, and the f_{C1} under hydrogen/methane flame conditions.

5.4 Effect of Perforated Plate on the Flashback

Figure 5.5 shows the turbulence intensity of the cold flow with respect to the blockage ratio of the perforated plate. Using a hot wire installed in the same position as the bluff body, the mean flow velocity and the velocity perturbation were measured for calculating the turbulence intensity of the cold flow. The black square symbol (blockage ratio = 0) presents the condition without the perforated plate. The magnitude of the turbulence intensity varies by almost twice, depending on the air mass flow rate condition. At air mass flow rates of 10 g/s and 12.5 g/s, the cold flow turbulence intensity has similar values regardless of the blockage ratio, when the perforated plate was installed in the combustor.

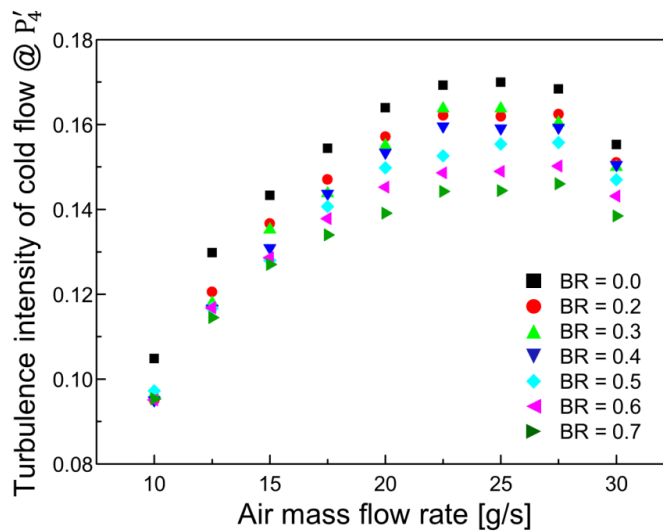


Fig. 5.5 Turbulence intensity of the non-reacting flow with respect to the blockage ratio of the perforated plate.

However, the difference in the turbulence intensity corresponding to the blockage ratio considerably increased with the increase in the mass flow rate. The turbulence intensity does not change linearly with the blockage ratio. When a perforated plate with a

blockage ratio of 0.2 was installed, the magnitude of the turbulence intensity relatively decreased, more than that in the case without the perforated plate, with similar values of the blockage ratio (0.3 and 0.4); the reduction rate increases again at a blockage ratio of 0.5. Meanwhile, the cold flow turbulence intensity has a maximum value without the perforated plate and decreases at the bluff body position, when a perforated plate with a lower blockage ratio is used. In general, a perforated plate with a high blockage ratio induces a high turbulence intensity [92]. However, in this study, the perforated plate plays a role in reducing the perturbation of the flow entering through the orifice.

Figure 5.6 presents the flashback distance data measured at various blockage ratios. The concentrated location of the data moves from right to left, as the blockage ratio increases. This tendency is more prominent, when the blockage ratio exceeds 50%. The flammability limit as per the blockage ratio hardly changes. Even though the same initial conditions including the equivalence ratio and inlet velocity were used, the magnitude of the pressure perturbation in the combustor is large, when a low blockage ratio perforated plate is used, increasing the flashback distance. This may be owing to the same reason because the cold flow turbulence intensity is differently displayed along the blockage ratio of the perforated plate under the same mass flow rate condition shown in Figure 5.5. Thermo-acoustic combustion instability occurs, when the pressure fluctuation generated by the heat release rate fluctuation affects the heat release rate fluctuation again through propagation and reflection inside the combustor, and they are in phase with each other. The mechanism of the thermo-acoustic combustion instability is called a Rayleigh criterion and can be expressed by the Equation 1.1.

Because the perforated plate was located between the bluff body and the orifice, the amplitude of the pressure fluctuation was attenuated by the perforated plate, when the fluctuation propagated and reflected in the combustor. As a result, the interaction between the reduced pressure fluctuation and the heat release rate fluctuation caused a reduction in the magnitude of the combustion instability and the flashback distance.

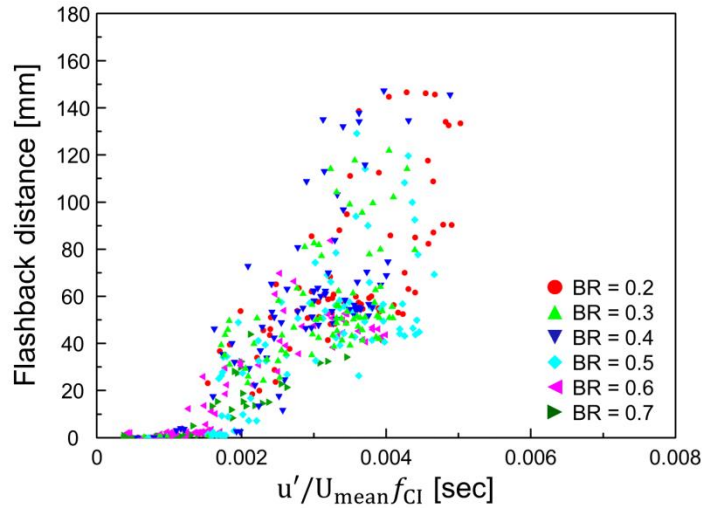
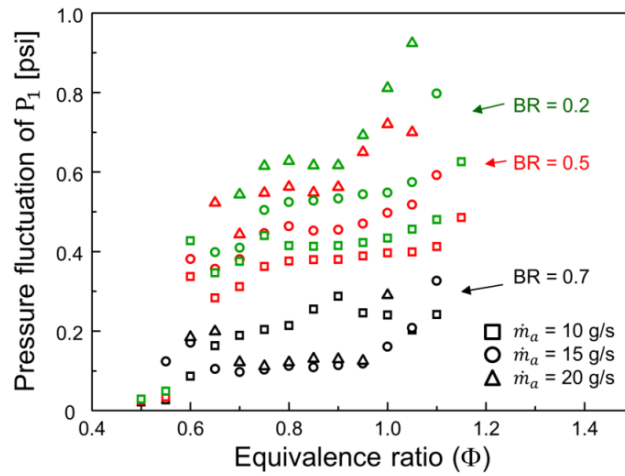


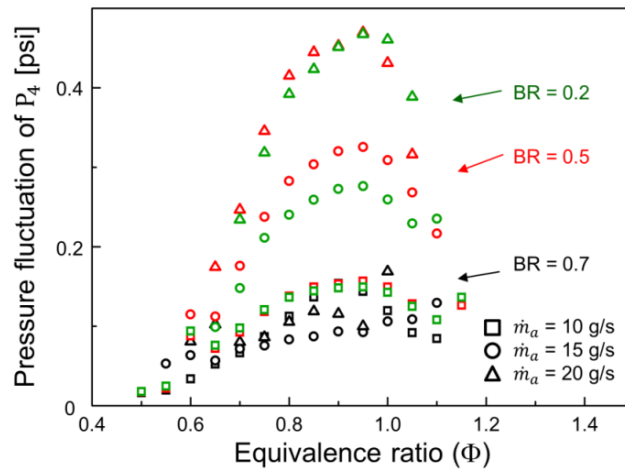
Fig. 5.6 Relationship amongst the D_{FB} , the measured pressure fluctuation, and the f_{CI} under various blockage ratio conditions.

The results of Figure 5.6 can be explained by the trends of the pressure perturbation as per the conditions. Figure 5.7 depicts the RMS value of the pressure perturbation occurring near the uppermost region of the combustor and the bluff body, depending on the blockage ratio of the perforated plate. The green, red, and black colors indicate cases of the perforated plates with blockage ratios of 0.2, 0.5, and 0.7, respectively. The magnitude of the pressure perturbation, by position, increases as the blockage ratio of the perforated plate decreases. In addition, the differences in the perturbation values between the 0.7 blockage ratio case and the other two cases are clear. In the previous work, it was revealed that the adverse pressure gradient generated inside the combustor caused the flashback phenomenon. Although the magnitude of the adverse pressure gradient cannot be defined by the difference in the pressure perturbation at two positions in the combustor, a significant perturbation difference between two positions is likely to increase the magnitude of the adverse pressure gradient. When combustion instability occurs, the reduction in the pressure fluctuation by the perforated plate effect causes a small-scale

adverse pressure gradient. Therefore, the flashback distance tends to be short with a high blockage ratio.



(a)



(b)

Fig. 5.7 Magnitude of the pressure perturbation with respect to the blockage ratio of the perforated plate; (a) near the uppermost region of the combustor and (b) near the bluff body.

5.5 Effect of the Reactant Temperature on the Flashback

Variations in the reactant temperature can cause changes in the flame velocity owing to modifications in the chemical reaction rate and changes in the acoustic characteristics owing to modifications in the temperature distribution in the combustor. These variations alter the characteristics of the combustion instability owing to its close connection with the flame stability.

Before analyzing the experimental results according to the variations in the reactant temperature, it is necessary to consider the flame behavior based on the temperature ratio between the reactant and the product. The bluff body flame exhibits a symmetric behavior near the bluff body and a sinuous behavior in the wake zone, when the reactant is at room temperature. When the reactant temperature increases and the temperature ratio decreases, the sinuous behavior moves upstream and appears near the bluff body. Therefore, the results should be carefully analyzed because differences in the flame behavior can lead to the different flashback characteristics. However, it is known that the behavior of flame according to the ratio has no significant difference, when the temperature ratio is 3.5 or more [88]. In the present work, the lowest temperature ratio is approximately 3.5, when raising the temperature of the reactant to 623 K; hence, there is no necessity to consider the change in the flame behavior.

Figure 5.8 depicts the laminar flame speed with respect to the equivalence ratio under various reactant temperature conditions. A GRI 3.0 mechanism was used for this calculation also, as with the hydrogen/methane fuel flame. The flame speed drastically increases with the reactant temperature and the increase rate is almost linear. The flame speed at the highest temperature condition, in particular, is faster than that of the mixed fuel with 75% hydrogen.

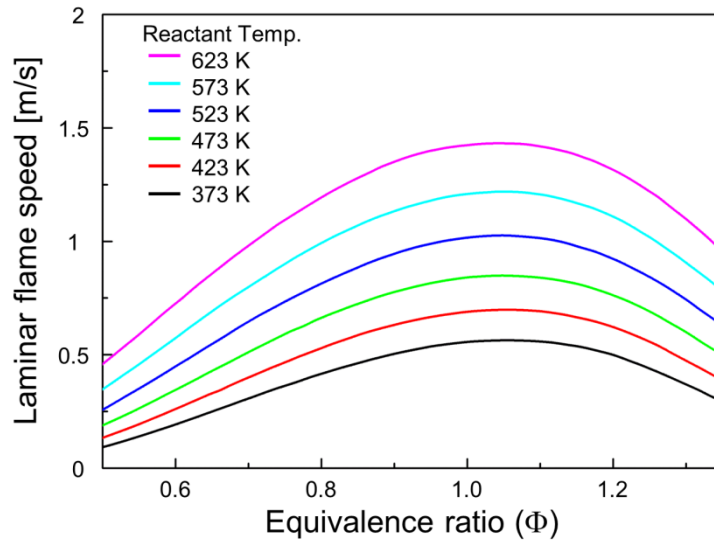


Fig. 5.8 S_L as per the equivalence ratio under various reactant temperature conditions (calculated using the GRI 3.0 mechanism).

Figure 5.9 presents the graph of the flashback distance with respect to the reactant temperature. The filled symbol indicates the conditions, where the reactant velocity was maintained constant and the hollow symbol indicates the case in which the temperature was increased with a fixed flow rate. The flashback distance is relatively short compared to the results in the Section 5.3 and 5.4. It is confirmed that the flame gradually stabilizes without generating a flashback, according to the increase in the reactant temperature. The high temperature of the reactant causes an increase in the flame stability [93, 94]. There were a few conditions in which that flame moved upstream to the leading edge of the bluff body above a temperature of 523 K. This result is similar to the condition, where the content of hydrogen was high in the hydrogen mixed fuel; however, there is a difference in terms of the flame stability. When a flashback occurs in a hydrogen/methane flame, the flame propagates to the fuel injection at a relatively low equivalence ratio and there is no condition that can be used to measure the flashback distance. However, as the flame itself

is stable, when the reactant temperature increases, the result shown in Figure 5.9 is obtained, although the range of the combustible equivalence ratio was similar to the low temperature condition. Therefore, it is not sufficient to judge the possibility of the occurrence of a flashback with the magnitude of the laminar flame velocity.

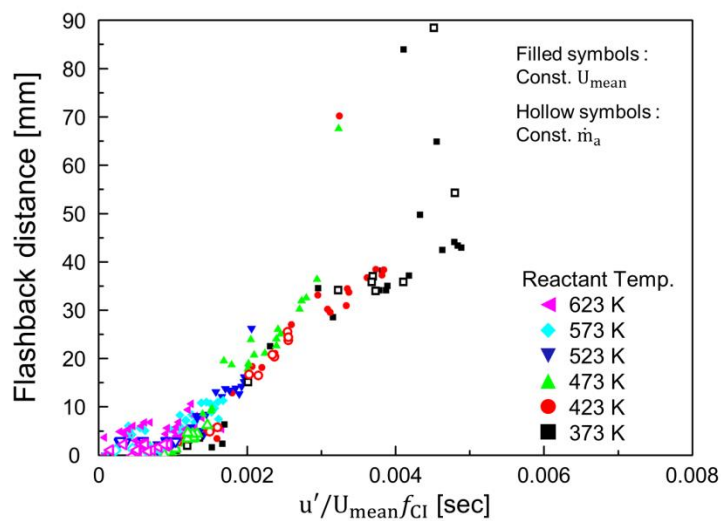


Fig. 5.9 Relationship amongst the D_{FB} , the measured pressure fluctuation, and the f_{CI} with respect to the reactant temperature (The filled symbol and hollow symbols indicate the constant velocity conditions and the constant flow rate conditions, respectively).

5.6 Relationship between the Experimental Conditions and Flashback Distance

The effect of the various parameters on the flashback distance was examined in Section 5.3, 5.4 and 5.5. In the previous work, the flashback distance data were effectively gathered using the Equation 5.1, comprising the pressure fluctuation, mean air velocity, and the frequency of the combustion instability as referred in Section 4.6.

$$\frac{u'}{U_{\text{mean}}f_{\text{CI}}} \quad (5.1)$$

where u' is calculated using the pressure fluctuation measured at P'_4 . When all the experimental results of the present work were exhibited on a graph using Equation 5.1, similar tendencies between the data shown in Figure 5.4, 5.6 and 5.9 were observed. However, this method was not sufficient to include the diversity of the various conditions because the data was rather distributed. Therefore, it was necessary to modify the introduction of the existing variables and to add new variables. The cause of the flashback phenomenon was comprehended by a simultaneous measurement of the flame structure and the pressure fluctuation and it was revealed that the adverse pressure gradient was the main cause for the flashback phenomenon, as mentioned in Section 5.4. Because the magnitude of the pressure fluctuation near the orifice was much larger than that near the bluff body, the magnitude of the adverse pressure gradient is more closely related to the pressure fluctuation near the orifice. Therefore, to reasonably represent the flow characteristics in the combustor, when combustion instability occurs, the pressure fluctuation data near the orifice was selected instead of the that near the bluff body.

The flame speed varies considerably in the combustion characteristics with the rise in the reactant temperature and the hydrogen/methane flame condition. The variation in the laminar flame speed was up to three times in the hydrogen/methane flame condition and four times in the reactant temperature rise condition, compared to a pure methane flame condition, as shown in Figure 5.3 and Figure 5.8. In addition, the change in the turbulence intensity due to the perforated plate can also influence the turbulent flame speed. In Chapter 4, it was confirmed that the freely propagating flame behavior was involved in the process of the flashback phenomenon. Figure 5.10 shows the flame structure, when flashback occurs under various conditions. These structural changes are similar regardless of the conditions.

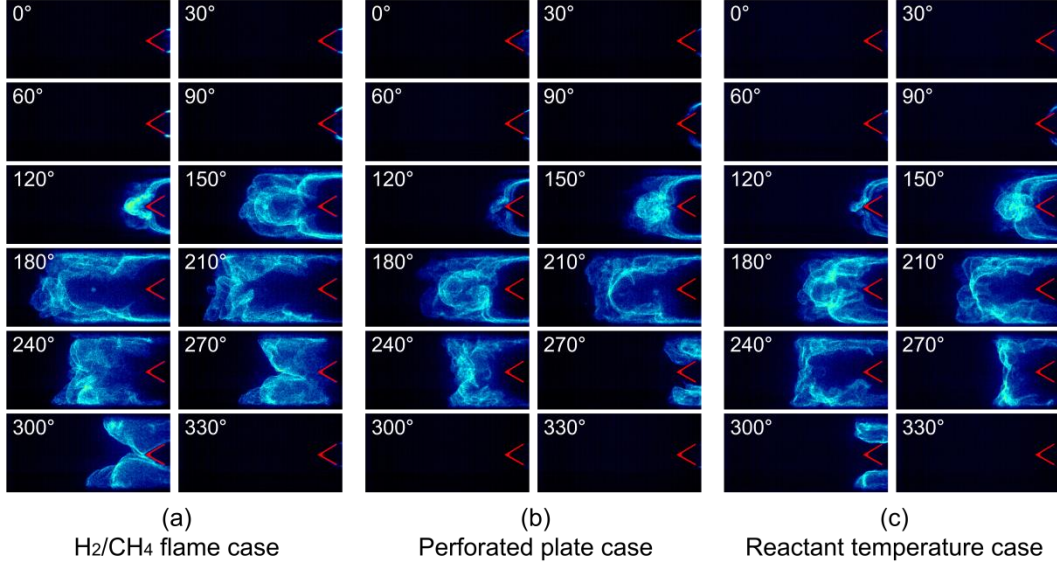


Fig. 5.10 Images of OH radical chemiluminescence in the vicinity of the bluff body during one period of (a) H₂/CH₄ flame case (H₂/CH₄ = 50%/50%, U_{mean} = 10.4 m/s, Φ = 0.80); (b) perforated plate case (BR = 0.5, U_{mean} = 10.4 m/s, Φ = 0.85); (c) reactant temperature case (T = 373 K, U_{mean} = 10.4 m/s, Φ = 0.90).

If a free propagation of the flame occurs for a period during the flashback phenomenon, the flame speed acts as a positive parameter, increasing the flashback distance. Therefore, the turbulent flame speed was included in the numerator of Equation 5.1. Although there are various methods for the calculation of the turbulent flame speed, it is a function of the laminar flame speed and the turbulence velocity fluctuation, and can be generally expressed as follows [95].

$$\frac{S_T}{S_L} = \left[1 + C \left(\frac{u'}{S_L} \right)^n \right]^{\frac{1}{n}} \quad (5.2)$$

where C and n are constants. Here, 0.45 and 1.0 are used as the value of C and n, respectively [96]. The values of the constants are slightly different depending on the

research method but the difference does not significantly affect the value of the turbulence flame velocity in the present work. The turbulence velocity fluctuation, u' , in Equation 5.2 was calculated through $u' \sim p'/\rho c$ [38]. The pressure fluctuation data near the bluff body, where the flame actually behaves was considered as p' because it is the process of determining the flame speed. Comprehensively, Equation 5.3 was formed using the pressure fluctuation, mean air velocity, frequency of the combustion instability and the turbulent flame velocity as the variables.

$$\frac{u'S_T}{U_{\text{mean}}f_{\text{CI}}L_{\text{Bluff}}} = \frac{I_{\text{flame}}}{St_{\text{flame}}} \quad (5.3)$$

where the L_{Bluff} is the hydraulic diameter of the bluff body. The turbulence intensity of the flame condition, I_{flame} , was defined to represent the relationship between the velocity fluctuation and the mean air velocity; the Strouhal number of the flame condition, St_{flame} , was defined to represent the relationship amongst the turbulence flame speed, combustion instability frequency, and bluff body diameter. Figure 5.11 depicts the relationship between the flashback distance and the results using Equation 5.3. The red, green, and blue symbols indicate the experimental results with the hydrogen/methane fuel, perforated plate, and the reactant temperature rise, respectively. In order to investigate the relationship with Chapter 4, the data of Figure 4.9 were presented as black symbol. Comparing Figure 5.3, 5.5, and 5.9 with Figure 5.11, it can be seen that the Equation 5.3 has a greater effect in gathering the flashback distance data than Equation 5.1. The method using Equation 5.3 is also consistent with the result of Chapter 4. Consequently, the characteristics of the flashback distance data obtained under various conditions were effectively represented, considering the upstream pressure fluctuation that represents the flow characteristics in the combustor and the turbulent flame speed that is determined by the laminar flame speed and the pressure fluctuation near flame.

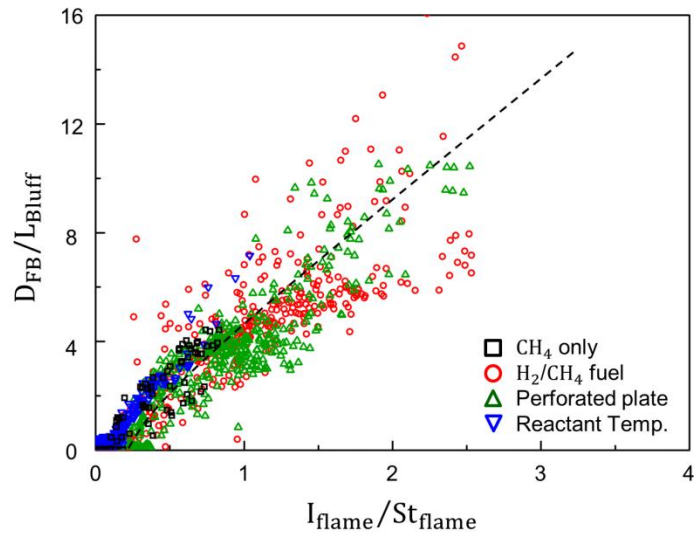


Fig. 5.11 Relationship between the D_{FB} and I_{flame}/St_{flame} for various initial conditions.

CHAPTER 6

CONCLUSION

In this study, the blowoff characteristics of a lean premixed flame in a duct combustor were investigated in the presence of external excitation. The blowoff equivalence ratio changed according to the geometry of the combustor and the flow properties. In addition, we once again confirmed that the recirculation zone inside the bluff body also plays an important role in flame stabilization. In the case of a flame without excitation, the recirculation zone collapsed near the blowoff and the flame was significantly smaller. However, this phenomenon was not directly connected to the blowoff and the flame recovered and became stable again. Shortly before the blowoff, the unburned gas strongly penetrated the recirculation zone, extinguishing the flame and disrupting the recirculation zone. Eventually, the penetrated unburned gas failed to ignite, and blowoff occurred. The relationship between the Damköhler number and the Reynolds number was examined using data from previous and present experiments. The results shed light on trends in the blowoff phenomenon and demonstrated that the flow velocity at the downstream tip of the bluff body and the laminar flame velocity under the condition of the blowoff equivalence ratio have a major impact on the blowoff.

In the presence of excitation, blowoff occurred via a similar process, except that a flame hole periodically appeared far from the blowoff. The blowoff equivalence ratio was increased by the intensity of the excitation, and it rapidly increased at specific excitation frequencies. POD analysis revealed that the frequencies with a high blowoff equivalence ratio corresponded to the peak frequencies of the shear-generated vortex of the bluff body. Because this vortex is associated with the harmonic frequency of the combustor, it was assumed that the resonance phenomenon was the cause of the increase in the blowoff equivalence ratio. The blowoff mechanism hypothesis was developed based on those results, and its verification was attempted using PIV and TMM. Consequently, it was found that blowoff occurs at a higher equivalence ratio when the maximum transverse

velocity downstream from the bluff body increases due to the resonance of the harmonic frequency and the excitation frequency.

The characteristics of the flashback phenomenon coupled with self-excited combustion instability were studied in turbulent premixed bluff body flames under various initial conditions. A flashback flame that did not arrive at the front of the bluff body was designated as a weak flame, and a flashback flame that propagated to the upstream region of the bluff body was designated as a strong flame. The features of the flame structure and the occurrence of strong flashback were examined primarily using high-speed OH-PLIF and PIV techniques.

In the present study, the values of pressure fluctuation amplitude and combustion instability frequency did not change significantly when combustion instability occurred. The combustion instability frequency varied depending on the length of the combustor. The calculated resonance frequency exists within the range of the combustion instability frequency, indicating that thermo-acoustic combustion instability occurs in the combustor. In the strong flashback condition, the distribution of the calculated Rayleigh index was greater in the positive section because the combustion instability driving was stronger (due to the small phase differences between pressure fluctuation and heat release fluctuation). This was confirmed that the characteristics of the flashback were related to combustion instability magnitude. When a weak flashback condition was shifted to a strong flashback condition by increasing equivalence ratio, the amplitude of pressure fluctuation was changed non-periodically. The intermittent increase of pressure fluctuation during these transition conditions provides more details about the characteristics of the strong flashback.

The circular structure of the flame in the front region of the bluff body is a characteristic of strong flashback. Reverse flow is caused by the inverse pressure gradient that occurs near the 90° phase of one period of combustion instability due to pressure fluctuation. The flame at the trailing edge of the bluff body was pushed by the reverse flow, and it moved forward to the upstream region of the bluff body. At that point, the flame on the side of the bluff body propagated rapidly under the influence of the

boundary layer flow and the decreased quenching distance. The flame that reached the front tip of the bluff body acted as an ignition source and generated the circular propagating flame. The velocity field was also generated along the direction of the flame propagation. It was confirmed that this circular propagating flame played an important role in increasing the flashback distance in the conditions of strong flashback. The flashback distance showed a tendency to increase in accordance with equivalence ratio and combustor length, and to decrease according to the inlet air velocity. In analyzing the data, turbulence intensity and combustion instability frequency were found to significantly influence the flashback distance. The combustion instability frequency was inversely proportional to the flashback distance when the all other conditions were the same because the time required for the flame to propagate to the upstream region of the bluff body decreased as the frequency increased.

Additionally, in order to confirm the applicability of research results of flashback under more practical conditions, experiment was conducted with the ratio of hydrogen to fuel, blockage ratio of perforated plate, and the reactant temperature as variables.

The flashback distance of the hydrogen/methane flame increased in comparison with the methane flame condition. The flashback distance gradually increased until the proportion of hydrogen reached 50% because the hydrogen/methane flame has a relatively higher flame speed than a pure methane flame. However, it appeared that the flashback distance became shorter, when the proportion of hydrogen became more than 50%. This is because the periodic combustion instability phenomenon disappeared, when the flame was completely backed up to the bluff body upstream, even with a relatively small pressure fluctuation. The turbulence intensity in the non-reacting flow exhibited a tendency to decrease as the blockage ratio of perforated plate increased. The flow stabilization characteristics of the perforated plate reduced the flashback distance, while reducing the pressure fluctuation in the combustor, when combustion instability occurred. The flashback distance sharply decreased in accordance with the pressure fluctuation magnitude, when the blockage ratio exceeded 50%. Although the flame speed increased with the reactant temperature, the flashback distance in the reactant temperature case

showed a different trend from the hydrogen/methane flame case. The increase in temperature stabilized the flame and the flashback distance gradually decreased. However, this result depends on whether combustion instability occurs separately from the flame speed and the gradient of the flashback distance data was similar to the other conditions.

The flashback distance data of the methane flame was collected using the relationship amongst the velocity fluctuation, mean velocity, and the combustion instability frequency. The results of the present work also show a linear trend, when the same empirical correlation is applied but this correlation was not adequate to include all the diversities, with a slightly scattered figure. In order to represent the combustor pressure characteristics primarily affecting the flashback phenomenon, the velocity fluctuation was calculated using the pressure fluctuation near the orifice instead of that near the bluff body. In addition, it was experimentally confirmed that the burning velocity plays a role in increasing the flashback distance, through a comprehensive analysis of the results of the previous and present works. The empirical correlation affecting the flashback distance was supplemented by modifying the velocity fluctuation parameter and adding the turbulent flame speed parameter. Consequently, the improved correlation was able to efficiently gather the flashback data obtained under various conditions and provided a comprehension of the main factors affecting the flashback distance.

APPENDIX A

VOLTAGE ADJUSTMENT

Excitation intensity varies depending on the frequency due to the speaker's characteristics if the input voltage to the speaker is the same. Voltage adjustment was required to maintain equal intensity depending on the excitation frequency. Figure A.1 shows the root-mean-square (RMS) value of the sound pressure obtained using a microphone. The sound pressure is directly proportional to the input voltage of the acoustic device. Moreover, sound pressure is also directly proportional to the frequency when the particle displacement is maintained as constant. Therefore, the voltage at a specific frequency can be described as follow:

$$V_{\text{freq}} = \frac{P_{\text{ref}}f_{\text{freq}}}{P_{\text{ref}}f_{\text{ref}}} V_{\text{ref}} \quad (\text{A.1})$$

where P_{ref} the is measured sound pressure at the reference frequency, P_{freq} is the measured sound pressure at the specific frequency using a microphone, f_{freq} is the specific frequency, f_{ref} is the reference frequency, and V_{ref} is the voltage at the reference frequency.

Figure A.2 shows the adjusted voltage using an acoustic device in a frequency range of 150 Hz to 400 Hz in increments of 10 Hz. These data were acquired by measuring the sound pressure with frequency and voltage variations. The reference voltage had a range of 2 volt to 12 volt in increments of 2 volt. The measurement was performed under a quasi-free-field condition.

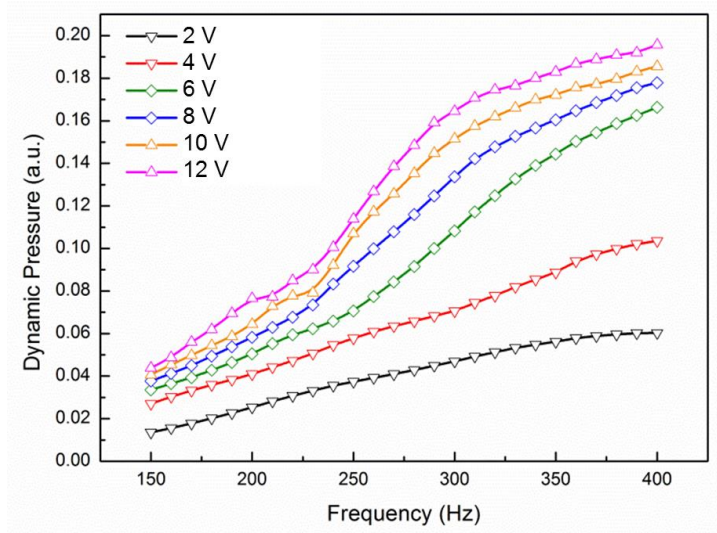


Fig. A.1 Measured sound pressure with excitation frequency variations.

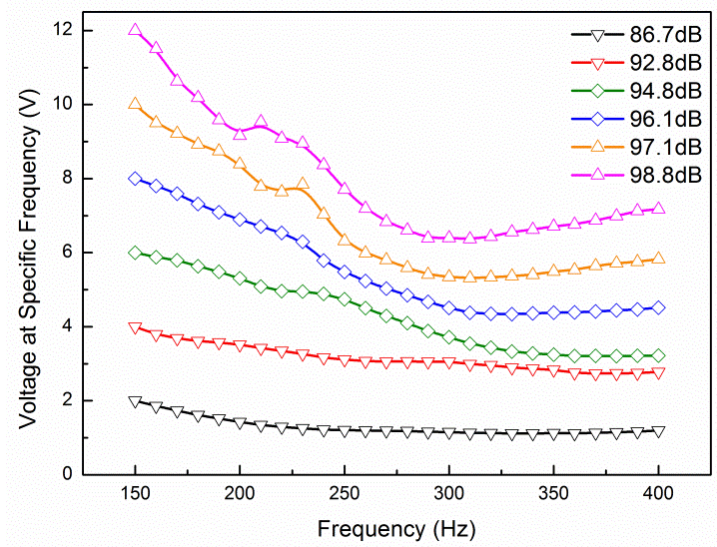


Fig. A.2 Adjusted voltage with excitation frequency variations.

APPENDIX B

SOUND PRESSURE LEVEL

Sound pressure level (SPL) is a logarithmic measure of the effective sound pressure of a sound relative to a reference value. It is measured in decibels (dB) above a standard reference level. The SPL value obtained using a microphone is described as follows:

$$\text{SPL} = 10 \log \left(\frac{P_{\text{rms}}^2}{P_0^2} \right) = 20 \log \left(\frac{P_{\text{rms}}}{P_0} \right) \quad (\text{B.1})$$

where P_{rms} is RMS value of the sound pressure, and $P_0 = 2.9 \times 10^{-9}$ psi. The excitation intensity indicates the SPL value obtained at a standard distance of 1 m. When SPL_1 is measured at a distance r_1 , the SPL_2 at a distance r_2 is described as follows:

$$\text{SPL}_2 = \text{SPL}_1 + 20 \log \left(\frac{r_1}{r_2} \right) \quad (\text{B.2})$$

where SPL_1 is the calculated value using Eq. B.1, r_1 is a measurement distance of sound pressure, and r_2 is the standard distance of 1 m. When the sound pressure was measured, the distance r_1 was 1.3 cm, taking the sensitivity of the microphone into consideration. The results of the calculation are shown in Table B.1.

Table B.1 Sound pressure and excitation intensity.

V_{ref} (V)	P_{rms} (a.u.)	SPL_1 (dB)	SPL_2 (dB)
2	0.0964	164.4	86.7
4	0.1943	170.5	92.8
6	0.2461	172.6	94.8
8	0.2863	173.9	96.1
10	0.3202	174.8	97.1
12	0.3896	176.5	98.8

REFERENCES

- [1] Y. Huang and V. Yang, "Dynamics and stability of lean-premixed swirl-stabilized combustion," *Progress in Energy and Combustion Science*, vol. 35, pp. 293-364, 2009.
- [2] S. J. Shanbhogue, S. Husain, and T. Lieuwen, "Lean blowoff of bluff body stabilized flames: Scaling and dynamics," *Progress in Energy and Combustion Science*, vol. 35, pp. 98-120, 2009.
- [3] P. Huerre and P. A. Monkewitz, "Local and global instabilities in spatially developing flow," *Annual review of fluid mechanics*, vol. 22, pp. 473-537, 1990.
- [4] J. Longwell, "Flame Stabilization by Bluff Bodies and Turbulent Flames in Ducts," in *Fourth Symposium (International) on Combustion*, 1953, pp. 90-97.
- [5] D. Spalding, "Theoretical aspects of flame stabilization: an approximate graphical method for the flame speed of mixed gases," *Aircraft Engineering and Aerospace Technology*, vol. 25, pp. 264-276, 1953.
- [6] F. Williams, "Flame stabilization of premixed turbulent gases," *Applied Mechanics Surveys*, pp. 1157-1170, 1966.
- [7] S. Yamaguchi, N. Ohiwa, and T. Hasegawa, "Structure and blow-off mechanism of rod-stabilized premixed flame," *Combustion and Flame*, vol. 62, pp. 31-41, 1985.
- [8] J. Pan and D. Ballal, "Chemistry and turbulence effects in bluff body stabilized flames," in *ASME Paper*, 1992, pp. 1992-771.
- [9] J.-T. Yang, G.-L. Tsai, and W.-B. Wang, "Near-wake characteristics of various v-shaped bluff bodies," *Journal of Propulsion and Power*, vol. 10, pp. 47-53, 1994.
- [10] S. Chaudhuri, S. Kostka, M. W. Renfro, and B. M. Cetegen, "Blowoff dynamics of bluff body stabilized turbulent premixed flames," *Combustion and Flame*, vol. 157, pp. 790-802, 2010.
- [11] S. G. Tuttle, S. Chaudhuri, S. Kostka Jr, K. M. Kopp-Vaughan, T. R. Jensen, B. M. Cetegen, et al., "Time-resolved blowoff transition measurements for two-dimensional bluff body-stabilized flames in vitiated flow," *Combustion and Flame*,

- vol. 159, pp. 291-305, 2012.
- [12] J. Dawson, R. Gordon, J. Kariuki, E. Mastorakos, A. Masri, and M. Juddoo, "Visualization of blow-off events in bluff-body stabilized turbulent premixed flames," *Proceedings of the Combustion Institute*, vol. 33, pp. 1559-1566, 2011.
 - [13] J. Kariuki, J. R. Dawson, and E. Mastorakos, "Measurements in turbulent premixed bluff body flames close to blow-off," *Combustion and flame*, vol. 159, pp. 2589-2607, 2012.
 - [14] S. Hemchandra, N. Peters, and T. Lieuwen, "Heat release response of acoustically forced turbulent premixed flames—role of kinematic restoration," *Proceedings of the Combustion Institute*, vol. 33, pp. 1609-1617, 2011.
 - [15] D.-H. Shin, D. V. Plaks, T. Lieuwen, U. M. Mondragon, C. T. Brown, and V. G. McDonnell, "Dynamics of a longitudinally forced, bluff body stabilized flame," *Journal of Propulsion and Power*, vol. 27, pp. 105-116, 2011.
 - [16] D.-H. Shin and T. Lieuwen, "Flame wrinkle destruction processes in harmonically forced, laminar premixed flames," *Combustion and Flame*, vol. 159, pp. 3312-3322, 2012.
 - [17] P. Palies, T. Schuller, D. Durox, L. Y. M. Gicquel, and S. Candel, "Acoustically perturbed turbulent premixed swirling flames," *Physics of Fluids*, vol. 23, 2011.
 - [18] J. P. Moeck, J.-F. Bourgooin, D. Durox, T. Schuller, and S. Candel, "Nonlinear interaction between a precessing vortex core and acoustic oscillations in a turbulent swirling flame," *Combustion and Flame*, vol. 159, pp. 2650-2668, 2012.
 - [19] A. Triantafyllidis, E. Mastorakos, and R. Eggels, "Large eddy simulations of forced ignition of a non-premixed bluff-body methane flame with conditional moment closure," *Combustion and Flame*, vol. 156, pp. 2328-2345, 2009.
 - [20] S. Ayache, J. Dawson, A. Triantafyllidis, R. Balachandran, and E. Mastorakos, "Experiments and Large-Eddy Simulations of acoustically forced bluff-body flows," *International Journal of Heat and Fluid Flow*, vol. 31, pp. 754-766, 2010.
 - [21] A. Chaparro, E. Landry, and B. M. Cetegen, "Transfer function characteristics of bluff-body stabilized, conical V-shaped premixed turbulent propane-air flames,"

- Combustion and flame, vol. 145, pp. 290-299, 2006.
- [22] S. Chaudhuri and B. M. Cetegen, "Response dynamics of bluff-body stabilized conical premixed turbulent flames with spatial mixture gradients," *Combustion and Flame*, vol. 156, pp. 706-720, 2009.
- [23] V. Acharya, B. Emerson, U. Mondragon, D.-H. Shin, C. Brown, V. McDonell, et al., "Velocity and flame wrinkling characteristics of a transversely forced, bluff-body stabilized flame, Part II: Flame response modeling and comparison with measurements," *Combustion Science and Technology*, vol. 185, pp. 1077-1097, 2013.
- [24] B. Emerson, U. Mondragon, V. Acharya, D.-H. Shin, C. Brown, V. McDonell, et al., "Velocity and flame wrinkling characteristics of a transversely forced, bluff-body stabilized flame, part I: experiments and data analysis," *Combustion Science and Technology*, vol. 185, pp. 1056-1076, 2013.
- [25] A. A. Chaparro and B. M. Cetegen, "Blowoff characteristics of bluff-body stabilized conical premixed flames under upstream velocity modulation," *Combustion and flame*, vol. 144, pp. 318-335, 2006.
- [26] S. Chaudhuri, S. Kostka, M. W. Renfro, and B. M. Cetegen, "Blowoff mechanism of harmonically forced bluff body stabilized turbulent premixed flames," *Combustion and Flame*, vol. 159, pp. 638-640, 2012.
- [27] S. Biswas, K. Kopp-Vaughn, M. W. Renfro, and B. M. Cetegen, "Phase resolved characterization of conical premixed flames near and far from blowoff," *Combustion and Flame*, vol. 160, pp. 2843-2855, 2013.
- [28] J. W. W. Rayleigh, *The Theory of Sound* vol. 2: Mc. Millan & Co London and New York, 1896.
- [29] T. C. Lieuwen, "Investigation of combustion instability mechanism in premixed gas turbines," Georgia Institute of Technology, 1999.
- [30] S. Candel, "Combustion dynamics and control progress and challenges," *Proceedings of the Combustion Institute*, vol. 29, pp. 1-28, 2002.
- [31] Y. Sommerer, D. Galley, T. Poinso, S. Ducruix, F. Lacas, and D. Veynante, "Large

- eddy simulation and experimental study of flashback and blow-off in a lean partially premixed swirled burner," *Journal of Turbulence*, vol. 5, 2004.
- [32] T. Lieuwen, V. McDonell, E. Petersen, and D. Santavicca, "Fuel Flexibility Influences on Premixed Combustor Blowout, Flashback, Autoignition, and Stability," *Journal of Engineering for Gas Turbines and Power*, vol. 130, p. 011506, 2008.
- [33] C. Eichler and T. Sattelmayer, "Premixed flame flashback in wall boundary layers studied by long-distance micro-PIV," *Experiments in Fluids*, vol. 52, pp. 347-360, 2011.
- [34] F. Dinkelacker, B. Manickam, and S. P. R. Muppala, "Modelling and simulation of lean premixed turbulent methane/hydrogen/air flames with an effective Lewis number approach," *Combustion and Flame*, vol. 158, pp. 1742-1749, 2011.
- [35] C. Heeger, R. L. Gordon, M. J. Tummers, T. Sattelmayer, and A. Dreizler, "Experimental analysis of flashback in lean premixed swirling flames: upstream flame propagation," *Experiments in Fluids*, vol. 49, pp. 853-863, 2010.
- [36] A. C. Benim, and Khawar Jamil Syed, *Flashback Mechanisms in Lean Premixed Gas Turbine Combustion*: Academic Press, 2014.
- [37] J. O. Keller, L. Vaneveld, D. Korschelt, G. L. Hubbard, A. F. Ghoniem, J. W. Daily, et al., "Mechanism of Instabilities in Turbulent Combustion Leading to Flashback," *AIAA JOURNAL*, vol. 20, pp. 254-262, 1982.
- [38] D. Thibaut and S. Candel, "Numerical Study of Unsteady Turbulent Premixed Combustion; Application to Flashback Simulation," *Combustion and flame*, vol. 113, pp. 53-65, 1998.
- [39] A. P. Dowling, "A kinematic model of a ducted flame," *Journal of Fluid Mechanics*, vol. 394, pp. 51-72, 1999.
- [40] C. Fureby, "A computational study of combustion instabilities due to vortex shedding," *Proceedings of the Combustion Institute*, vol. 28, pp. 783-791, 2000.
- [41] A. F. Ghoniem, S. Park, A. Wachsman, A. Annaswamy, D. Wee, and H. M. Altay, "Mechanism of combustion dynamics in a backward-facing step stabilized

- premixed flame," *Proceedings of the Combustion Institute*, vol. 30, pp. 1783-1790, 2005.
- [42] A. L. Birbaud, D. Durox, S. Ducruix, and S. Candel, "Dynamics of confined premixed flames submitted to upstream acoustic modulations," *Proceedings of the Combustion Institute*, vol. 31, pp. 1257-1265, 2007.
- [43] S. Hong, R. L. Speth, S. J. Shanbhogue, and A. F. Ghoniem, "Examining flow-flame interaction and the characteristic stretch rate in vortex-driven combustion dynamics using PIV and numerical simulation," *Combustion and Flame*, vol. 160, pp. 1381-1397, 2013.
- [44] S. Hong, S. J. Shanbhogue, K. S. Kedia, and A. F. Ghoniem, "Impact of the Flame-Holder Heat-Transfer Characteristics on the Onset of Combustion Instability," *Combustion Science and Technology*, vol. 185, pp. 1541-1567, 2013.
- [45] S. Hong, S. J. Shanbhogue, R. L. Speth, and A. F. Ghoniem, "On the phase between pressure and heat release fluctuations for propane/hydrogen flames and its role in mode transitions," *Combustion and Flame*, vol. 160, pp. 2827-2842, 2013.
- [46] A. Birch, D. Brown, M. Fairweather, and G. Hargrave, "An experimental study of a turbulent natural gas jet in a cross-flow," *Combustion science and technology*, vol. 66, pp. 217-232, 1989.
- [47] J. M. Seitzman, A. Ungut, P. H. Paul, and R. K. Hanson, "Imaging and characterization of OH structure in a turbulent nonpremixed flame," *Proceedings of the Combustion Institute*, pp. 637-644, 1990.
- [48] S. R. Turns, *An introduction to combustion: McGraw-hill New York*, 1996.
- [49] M. Stöhr, C. Arndt, and W. Meier, "Effects of Damköhler number on vortex-flame interaction in a gas turbine model combustor," *Proceedings of the Combustion Institute*, vol. 34, pp. 3107-3115, 2013.
- [50] M. Stöhr, I. Boxx, C. Carter, and W. Meier, "Dynamics of lean blowout of a swirl-stabilized flame in a gas turbine model combustor," *Proceedings of the Combustion Institute*, vol. 33, pp. 2953-2960, 2011.
- [51] I. Boxx, M. Stöhr, C. Carter, and W. Meier, "Temporally resolved planar

- measurements of transient phenomena in a partially pre-mixed swirl flame in a gas turbine model combustor," *Combustion and Flame*, vol. 157, pp. 1510-1525, 2010.
- [52] P. Petersson, R. Wellander, J. Olofsson, H. Carlsson, C. Carlsson, B. B. Watz, et al., "Simultaneous high-speed PIV and OH PLIF measurements and modal analysis for investigating flame-flow interaction in a low swirl flame," in *International Symposium Applied Laser Technical Fluid Mechanical*, 2012, pp. 09-12.
- [53] P. Xavier, A. Vandael, G. Godard, B. Renou, F. Grisch, G. Cabot, et al., "Analysis of the flame structure in a trapped vortex combustor using low and high-speed OH-PLIF," in *ASME Turbo Expo 2014: Turbine Technical Conference and Exposition*, 2014, pp. V04AT04A012-V04AT04A012.
- [54] J. R. Dawson, R. L. Gordon, J. Kariuki, E. Mastorakos, A. R. Masri, and M. Juddoo, "Visualization of blow-off events in bluff-body stabilized turbulent premixed flames," *Proceedings of the Combustion Institute*, vol. 33, pp. 1559-1566, 2011.
- [55] N. A. Worth and J. R. Dawson, "Cinematographic OH-PLIF measurements of two interacting turbulent premixed flames with and without acoustic forcing," *Combustion and Flame*, vol. 159, pp. 1109-1126, 2012.
- [56] S. Hammack, S. Kostka, A. Lynch, C. Carter, and T. Lee, "Simultaneous 10-kHz PLIF and chemiluminescence imaging of OH radicals in a microwave plasma-enhanced flame," *IEEE Transactions on Plasma Science*, vol. 41, pp. 3279-3286, 2013.
- [57] P. M. Allison, Y. Chen, M. Ihme, and J. F. Driscoll, "Coupling of flame geometry and combustion instabilities based on kilohertz formaldehyde PLIF measurements," *Proceedings of the Combustion Institute*, vol. 35, pp. 3255-3262, 2015.
- [58] S. Meares, V. N. Prasad, M. Juddoo, K. H. Luo, and A. R. Masri, "Simultaneous planar and volume cross-LIF imaging to identify out-of-plane motion," *Proceedings of the Combustion Institute*, vol. 35, pp. 3813-3820, 2015.
- [59] E. E. Zukoski, "Flame stabilization on bluff bodies at low and intermediate

- Reynolds numbers," Ph.D., California Institute of Technology, 1954.
- [60] A. Roshko, "On the development of turbulent wakes from vortex streets," National Advisory Committee for Aeronautics, Washington D.C. NACA Report 1191, 1954.
 - [61] S. M. Bush and E. J. Gutmark, "Reacting and nonreacting flowfields of a V-gutter stabilized flame," AIAA journal, vol. 45, pp. 662-672, 2007.
 - [62] B. Kiel, K. Garwick, J. R. Gord, J. Miller, A. Lynch, R. Hill, et al., "A detailed investigation of bluff body stabilized flames," in ASME Paper, 2007.
 - [63] R. Balachandran, B. Ayoola, C. Kaminski, A. Dowling, and E. Mastorakos, "Experimental investigation of the nonlinear response of turbulent premixed flames to imposed inlet velocity oscillations," Combustion and Flame, vol. 143, pp. 37-55, 2005.
 - [64] M. P. Waser and M. J. Crocker, "Introduction to the two-microphone cross-spectral method of determining sound intensity," Noise Control Engineering Journal, vol. 22, pp. 76-85, 1984.
 - [65] J. O'Connor and T. Lieuwen, "Recirculation zone dynamics of a transversely excited swirl flow and flame," Physics of Fluids (1994-present), vol. 24, p. 075107, 2012.
 - [66] I. Glassman, Combustion, 3rd ed. London: Academic press, 1997.
 - [67] S. Hong, S. J. Shanbhogue, and A. F. Ghoniem, "Impact of fuel composition on the recirculation zone structure and its role in lean premixed flame anchoring," Proceedings of the Combustion Institute, vol. 35, pp. 1493-1500, 2015.
 - [68] C. Armitage, R. Balachandran, E. Mastorakos, and R. Cant, "Investigation of the nonlinear response of turbulent premixed flames to imposed inlet velocity oscillations," Combustion and Flame, vol. 146, pp. 419-436, 2006.
 - [69] I. Weisbrot and I. Wygnanski, "On coherent structures in a highly excited mixing layer," Journal of Fluid Mechanics, vol. 195, pp. 137-159, 1988.
 - [70] P. G. Mehta and M. C. Soteriou, "Combustion heat release effects on the dynamics of bluff body stabilized premixed reacting flows," in ASME Paper, 2003.

- [71] S. Kostka, A. C. Lynch, B. C. Huelskamp, B. V. Kiel, J. R. Gord, and S. Roy, "Characterization of flame-shedding behavior behind a bluff-body using proper orthogonal decomposition," *Combustion and Flame*, vol. 159, pp. 2872-2882, 2012.
- [72] H. Chen, D. L. Reuss, D. L. Hugn, and V. Sick, "A practical guide for using proper orthogonal decomposition in engine research," *International Journal of Engine Research*, vol. 14, pp. 307-319, 2012.
- [73] M. C. Lee, J. Yoon, S. Joo, J. Kim, J. Hwang, and Y. Yoon, "Investigation into the cause of high multi-mode combustion instability of H₂/CO/CH₄ syngas in a partially premixed gas turbine model combustor," *Proceedings of the Combustion Institute*, vol. 35, pp. 3263-3271, 2015.
- [74] S. L. Plee and A. M. Mellor, "Review of Flashback Reported in Pre-vaporizing Premixing Combustors," *Combustion and flame*, vol. 32, pp. 193-203, 1978.
- [75] L. Vaneveld, K. Hom, and A. K. Oppenheim, "Secondary effects in combustion instabilities leading to flashback," *AIAA Journal*, vol. 22, pp. 81-82, 1984.
- [76] A. Gruber, J. H. Chen, D. Valiev, and C. K. Law, "Direct numerical simulation of premixed flame boundary layer flashback in turbulent channel flow," *Journal of Fluid Mechanics*, vol. 709, pp. 516-542, 2012.
- [77] D. Ebi and N. T. Clemens, "Experimental investigation of upstream flame propagation during boundary layer flashback of swirl flames," *Combustion and Flame*, vol. 168, pp. 39-52, 2016.
- [78] W. Meier, I. Boxx, M. Stöhr, and C. D. Carter, "Laser-based investigations in gas turbine model combustors," *Experiments in Fluids*, vol. 49, pp. 865-882, 2010.
- [79] L. Figura, J. G. Lee, B. D. Quay, and D. A. Santavicca, "The effects of fuel composition on flame structure and combustion dynamics in a lean premixed combustor," in *ASME Turbo Expo 2007: Power for Land, Sea, and Air, 2007*, pp. 181-187.
- [80] T. F. Wall, "Combustion processes for carbon capture," *Proceedings of the Combustion Institute*, vol. 31, pp. 31-47, 2007.
- [81] J. Yoon, M.-C. Lee, S. Joo, J. Kim, and Y. Yoon, "Instability mode and flame

- structure analysis of various fuel compositions in a model gas turbine combustor," *Journal of Mechanical Science and Technology*, vol. 29, pp. 899-907, 2015.
- [82] R. M. Jones and N. Z. Shilling, "IGCC gas turbine for refinery applications," *GE Energy* 2003.
- [83] S. Malavasi, G. Messa, U. Fratino, and A. Pagano, "On the pressure losses through perforated plates," *Flow Measurement and Instrumentation*, vol. 28, pp. 57-66, 2012.
- [84] N. Noiray, D. Durox, T. Schuller, and S. Candel, "Passive control of combustion instabilities involving premixed flames anchored on perforated plates," *Proceedings of the Combustion Institute*, vol. 31, pp. 1283-1290, 2007.
- [85] H. M. Altay, K. S. Kedia, R. L. Speth, and A. F. Ghoniem, "Two-dimensional simulations of steady perforated-plate stabilized premixed flames," *Combustion Theory and Modelling*, vol. 14, pp. 125-154, 2010.
- [86] K. S. Kedia and A. F. Ghoniem, "Mechanisms of stabilization and blowoff of a premixed flame downstream of a heat-conducting perforated plate," *Combustion and Flame*, vol. 159, pp. 1055-1069, 2012.
- [87] J. Edacheri Veetil, C. V. Rajith, and R. K. Velamati, "Numerical simulations of steady perforated-plate stabilized Syngas air pre-mixed flames," *International Journal of Hydrogen Energy*, vol. 41, pp. 13747-13757, 2016.
- [88] R. R. Erickson and M. C. Soteriou, "The influence of reactant temperature on the dynamics of bluff body stabilized premixed flames," *Combustion and Flame*, vol. 158, pp. 2441-2457, 2011.
- [89] B. Emerson, J. O'Connor, M. Juniper, and T. Lieuwen, "Density ratio effects on reacting bluff-body flow field characteristics," *Journal of Fluid Mechanics*, vol. 706, pp. 219-250, 2012.
- [90] K. Manoharan and S. Hemchandra, "Absolute, Convective Instability Transition in a Backward Facing Step Combustor: Fundamental Mechanism and Influence of Density Gradient," *Journal of Engineering for Gas Turbines and Power*, vol. 137, p. 2015.

- [91] B. Emerson and T. Lieuwen, "Dynamics of harmonically excited, reacting bluff body wakes near the global hydrodynamic stability boundary," *Journal of Fluid Mechanics*, vol. 779, pp. 716-750, 2015.
- [92] B. Roy Chowdhury, J. A. Wagner, and B. M. Cetegen, "Experimental study of the effect of turbulence on the structure and dynamics of a bluff-body stabilized lean premixed flame," *Proceedings of the Combustion Institute*, 2016.
- [93] A. K. Gupta, "Flame characteristics and challenges with high temperature air combustion," *Proceedings of the International Joint Power Generation Conference*, pp. 23-26, 2000.
- [94] S. Lamige, J. Min, C. Galizzi, F. André, F. Baillot, D. Escudié and K. Lyons, "On preheating and dilution effects in non-premixed jet flame stabilization," *Combustion and Flame*, vol. 160, pp. 1102-1111, 2013.
- [95] G. Fru, D. Thévenin, and G. Janiga, "Impact of Turbulence Intensity and Equivalence Ratio on the Burning Rate of Premixed Methane–Air Flames," *Energies*, vol. 4, pp. 878-893, 2011.
- [96] I. G. Shepherd and R. K. Cheng, "The burning rate of premixed flames in moderate and intense turbulence," *Combustion and flame*, vol. 127, pp. 2066-2075, 2001

초 록

보염기를 사용하는 덕트형 밀폐 연소기에서 예혼합 난류 화염의 동특성과 이에 관련된 연소 불안정 현상에 대한 연구를 실험적으로 수행하였다. 안정한 연소 조건에서 당량비가 감소할 경우 발생하는 희박 화염 날림의 자체적인 특성과 외부 교란이 있는 경우를 고려하여 음향 가진을 주었을 때 나타나는 특성을 비교 및 분석하였다. 또한 안정한 연소 조건에서 당량비가 증가할 경우 발생하는 자발적 연소 불안정 현상의 특징을 연구하고 연소 불안정이 야기시키는 화염의 역류에 대한 연구를 수행하였다.

희박 화염 날림은 보염기의 크기가 크거나 보염기 내부에 공간이 존재할수록 더 낮은 당량비에서 발생하는데 이는 재순환 영역의 크기에 연관이 있다. 동일한 보염기에서는 유입되는 혼합기의 속도가 증가할수록 더 높은 당량비에서 화염 날림 현상이 발생하였다. 화염의 구조적 변화는 OH 라디칼 자발광 계측을 이용하여 관측되었다. 외부 가진이 없는 조건에서는 화염 날림이 발생하기 직전에 보염기 후류에서 화염이 국소적으로 소멸되어 나타나는 화염 구멍이 발견되었고 재순환 영역이 붕괴되는 현상이 나타났다. 이로 인해서 새롭게 유입되는 반응물이 연소되지 못하고 화염이 꺼지는 현상이 발생하였다. 레이놀즈 수와 댐코올러 수의 관계를 통해서 보염기 후단에서의 유동 속도와 난류 화염 속도가 화염 날림에 중요한 영향을 미치는 변수임을 확인하였다. 외부 가진이 존재할 때 희박 화염 날림의 구조적 변화는 가진이 존재하지 않을 때와 유사하였다. 다만, 안정한 조건에서도 화염 구멍이 가진 주기와 일치해서 나타나는 모습을 보여주었다. 음향 가진의 세기가 증가할수록 화염 날림의 당량비는 증가하면서 화염의 안정성을 떨어뜨리는 결과가 나타났다. 그리고 특정 주파수에서 화염 날림 당량비가 급격히 증가하는 현상이 발생하였다. 연소

기 길이 변화, POD (적합직교분해법), Two-microphone 기법, phase-locked PIV (위상 고정 입자 영상 유속계) 기법 등을 통해서 원인을 파악하였다. 연소기의 조화 주파수와 외부 가진 주파수가 일치하게 되면 공진 현상이 발생하고, 공진 현상은 연소기 내부의 유속 섭동과 재순환 영역 전단층의 반응물 침투 속도를 증가시키게 된다. 결과적으로, 순간적으로 유입되는 반응물의 속도가 증가하여 화염을 유지하기 위해서 더 높은 연소 속도가 요구됨에 따라 화염 날림이 더 높은 당량비에서 발생하는 것으로 판단되었다. 또한 공진 현상을 일으키는 가진 주파수 조건에서는 재순환 영역의 크기도 위상에 따라 변화함을 확인하였고 화염 안정성을 저하시키는 원인으로 생각된다.

자발적 연소 불안정에 의한 역화 현상은 희박 예혼합 조건에서 특징적으로 나타나는 현상으로 안정한 화염 조건에서 당량비를 증가시켰을 때 발생한다. 이전까지는 역화가 발생할 때 화염이 보염기 후단 주변에서 앞뒤로 움직이는 현상에 대해서 연구가 이루어져 왔으나, 불안정의 규모가 커짐에 따라 화염이 보염기 상류로 전파되는 역화 현상이 관측되었으며 이에 대한 연구를 진행하였다. 연소기의 길이 변화에 따라서 발생하는 연소 불안정 주파수가 변화되었으며 이를 통해 열-음향학적 연소 불안정이 발생했음을 확인하였다. 레일리 지수를 약한 역화 조건과 강한 역화 조건에 적용해본 결과 강한 역화 조건에서 음향 섭동과 열 방출량 섭동의 위상 차이가 더 작음이 관찰되었고 연소 불안정 규모와 역화의 세기가 비례하는 것을 확인하였다. 역화 순간의 화염 구조 관측과 분석을 위하여 고속의 평면 레이저 유도 형광법과 압력 섭동 측정을 동시에 수행하였고 위상 고정 입자 영상 유속계 기법을 적용하였다. 강한 역화 현상이 발생할 때, 연소기 전단의 압력이 크게 섭동하며 순간적으로 역 압력 구배가 형성되었다. 역 압력 구배는 유동을 역류시키며, 역류된 유동은 보염기 후단에 붙어있던 화염을 상류로 밀게 된다. 역화되는 화염은 경계층 유동 효과와 줄어든 소염 거리의 영향으로 보염기 옆면을 타고 더욱 빠

르게 이동하였다. 이 화염은 보염기 상단에서 점화원으로 작용하며 모든 방향으로 전파되는 화염을 발생시키면서 역화 거리를 증가시키는 주요 원인으로 작용하는 것을 확인하였다. 화염의 역화 거리는 연소기의 길이가 길고 유속이 낮으며 당량비가 높을수록 증가하였다. 연소기 길이만을 변수로 두었을 때도 역화 거리에 변화가 존재하였으며 이는 길이에 따라 변화하는 연소 불안정 주파수의 영향인 것으로 생각되었다. 압력 섭동과 유속을 이용해 얻은 난류 강도와 불안정 주파수가 다양한 조건에서 얻어진 역화 거리의 데이터를 하나의 선에 모으기 위한 변수로 적절히 작용함에 따라 두 변수가 역화 거리에 지배적인 영향을 미치는 원인이라고 판단하였다.

추가적으로, 현실적인 조건하에서 연구 결과의 적용 가능성을 확인해 보기 위해 수소/메탄 혼합 연료, 다공성 판의 차폐율, 반응물 온도를 변수로 하여 실험을 진행하였다. 수소의 첨가는 화염 속도를 증가시키며 메탄 화염보다 역화 거리를 증가시키는 원인으로 작용하였다. 그러나 수소의 비율이 50%를 넘어가게 되면 역화가 연료 인젝터까지 진행되어 역화 거리를 측정할 수 없는 조건이 쉽게 발생하였다. 다공성 판의 차폐율이 증가하는 경우 비반응장 유동에서 유동의 난류 강도가 약화되었다. 이러한 특성은 연소 불안정이 발생했을 때 압력 섭동을 감소시키는 역할을 하였고 역화 거리도 함께 감소하였다. 반응물 온도의 증가는 수소의 첨가와 동일하게 화염 속도를 증가시켰다. 그러나 화염의 안정성도 증가하여 높은 온도에서는 역화가 거의 발생하지 않았다. 난류 강도와 불안정 주파수 만으로 모든 조건에서 얻은 데이터들을 모으는데 한계가 있었기 때문에 새로운 변수의 도입이 필요하였다. 연소 불안정의 압력 섭동을 대표하는 값으로 보염기 위치의 압력 섭동 대신에 오리피스 근처의 압력 섭동을 사용하였다. 또한 각 조건의 층류 화염 속도와 난류 강도를 대변하기 위해 난류 화염 속도의 영향을 함께 고려하였다. 결과적으로 속도 섭동, 난류 화염 속도, 유동 평균 속도, 연소 불안정 주파수 사이의 관계를 통해서 메

탄 화염의 결과를 포함한 다양한 실험의 결과들을 효과적으로 모으면서 역화에 영향을 미치는 변수들을 확인하였다.

중심어: 예혼합화염, 난류화염, 보염기 화염, 희박 화염 날림, 음향 가진, 댐코올러 수, 공진, 열-음향학적 연소 불안정, 역화, 난류 강도, 불안정 주파수, 화염 속도, OH, PIV, OH PLIF

학 번: 2010-20721